

RECONSTRUCTION OF  $B$  MESON DECAYS AND  
MEASUREMENT OF THE  $B$  QUARK AND  $B$  MESON  
PRODUCTION CROSS SECTIONS  
AT THE FERMILAB TEVATRON COLLIDER

Richard Edward Hughes

A DISSERTATION

in

PHYSICS

Presented to the Faculties of the University of Pennsylvania in Partial Fulfillment of  
the Requirements for the Degree of Doctor of Philosophy

1992

  
Supervisor of Dissertation

  
Graduate Group Chairperson

## **ACKNOWLEDGMENTS**

I would like to thank Larry Gladney and Nigel Lockyer for their help in this analysis. I would also like to thank the many members of the Penn group who helped make my stay in room 2W11 so enjoyable. And finally, I would like to thank my CDF collaborators and the members of the technical staff at Fermilab, for their many contributions in making the CDF experiment a success.

**ABSTRACT**

**RECONSTRUCTION OF  $B$  MESON DECAYS AND  
MEASUREMENT OF THE  $B$  QUARK AND  $B$  MESON  
PRODUCTION CROSS SECTIONS  
AT THE FERMILAB TEVATRON COLLIDER**

Richard Edward Hughes

Dissertation Supervisor: Larry D. Gladney

We report on the full reconstruction of  $B$  meson decays using data obtained at the Collider Detector at Fermilab in  $\bar{p}p$  collisions at  $\sqrt{s} = 1.8 \text{ TeV}$ . We have reconstructed  $B$  meson decays in the mode  $B_u^- \rightarrow J/\psi + K^-$  ( $J/\psi \rightarrow \mu^+ \mu^-$ ). This sample represents the first and only full reconstruction of  $B$  mesons in a hadron collider. We use this sample to extract the  $B$  meson and  $b$  quark production cross sections. We obtain  $\sigma = 6.1 \pm 1.9(\text{stat.}) \pm 2.4(\text{syst.}) \mu\text{b}$ , for  $b$  quarks with transverse momentum  $P_t > 10.5 \text{ GeV}/c$  and rapidity  $|y| < 1.0$ , and  $\sigma = 2.8 \pm 0.9(\text{stat.}) \pm 1.1(\text{syst.}) \mu\text{b}$ , for  $B_u^-$  mesons with transverse momentum  $P_t > 9.0 \text{ GeV}/c$  and rapidity  $|y| < 1.0$ . We compare the  $b$  quark result with an  $O(\alpha^3)$  QCD calculation.

## Contents

<b>1</b>	<b>Introduction</b>	<b>1</b>
<b>2</b>	<b>Theory</b>	<b>4</b>
2.1	The Standard Model . . . . .	4
2.2	$b$ quark Production . . . . .	7
2.3	$b$ quark Fragmentation . . . . .	12
2.4	$B_u^- \rightarrow J/\psi + K^-$ Decay . . . . .	17
<b>3</b>	<b>The Fermilab Tevatron</b>	<b>19</b>
<b>4</b>	<b>The CDF Detector</b>	<b>23</b>
4.1	Overview . . . . .	23
4.2	The Vertex Time Projection Chamber (VTPC) . . . . .	24
4.3	The Central Tracking Chamber (CTC) . . . . .	25
4.4	The Solenoidal Coil . . . . .	29
4.5	Central Calorimetry . . . . .	29
4.6	The Central Muon Detector (CMU) . . . . .	30

<b>5</b>	<b>Triggering</b>	<b>33</b>
5.1	Overview . . . . .	33
5.2	Level 1 . . . . .	34
5.2.1	Data sample used to Measure the Efficiency . . . . .	37
5.2.2	Trigger Efficiency of <i>Real</i> Muons . . . . .	37
5.2.3	Trigger Efficiency of Interacting Punchthrough . . . . .	38
5.2.4	Trigger Efficiency of Decays-in-Flight . . . . .	42
5.2.5	Method . . . . .	42
5.2.6	Parameterization of the Efficiency . . . . .	49
5.3	Level 2 . . . . .	55
5.3.1	The Efficiency of the CFT . . . . .	60
5.3.2	The Efficiency of the Level-2 System . . . . .	60
<b>6</b>	<b>Offline Reconstruction</b>	<b>63</b>
6.1	Z Vertex Reconstruction . . . . .	64
6.2	Track Reconstruction in the CTC . . . . .	66
6.2.1	Algorithm . . . . .	68
6.2.2	Wire Resolution and Efficiency . . . . .	70
6.2.3	Track Quality Cuts . . . . .	70
6.2.4	Track Reconstruction Efficiency . . . . .	70
6.3	Determining the Beam Position . . . . .	72

6.4	Track Reconstruction in the CMU . . . . .	75
6.4.1	Algorithm . . . . .	76
6.4.2	Wire Resolution and Efficiency . . . . .	77
6.4.3	CMU Track Reconstruction Efficiency . . . . .	81
6.5	Linking CMU tracks with CTC tracks . . . . .	81
6.5.1	Algorithm . . . . .	81
6.5.2	CMU-CTC Link Quality Cuts . . . . .	83
6.5.3	Link Efficiency . . . . .	85
6.6	Vertexing and Mass Constraint Algorithms . . . . .	87
6.6.1	Performance . . . . .	90
<b>7</b>	<b>Reconstruction of Particle Decays</b>	<b>93</b>
7.1	Data Sample . . . . .	93
7.2	Isolation of $\psi(2S) \rightarrow J/\psi \pi^+ \pi^-$ . . . . .	97
7.3	Isolation of $B_u^- \rightarrow J/\psi + K^-$ . . . . .	98
7.4	Determining the Origin of the Background for $B_u^- \rightarrow J/\psi + K^-$ . . .	103
7.5	Determining the Number of Observed $B_u^- \rightarrow J/\psi + K^-$ Events . . . .	109
7.5.1	Fit Procedure . . . . .	109
7.5.2	Fit Results . . . . .	112
<b>8</b>	<b>Measuring the Cross Sections</b>	<b>115</b>

8.1	Method . . . . .	115
8.1.1	Monte Carlo Generation . . . . .	115
8.1.2	Trigger Model . . . . .	123
8.1.3	Detector Model . . . . .	123
8.1.4	Comparison of Data with the Monte Carlo Model . . . . .	132
8.2	The $b$ quark Cross Section . . . . .	135
8.3	The $B$ Meson Cross Section . . . . .	142
<b>9</b>	<b>Conclusions</b>	<b>145</b>
9.1	Comparison of the measurement with theoretical prediction . . . . .	145
9.2	Future Prospects . . . . .	146
	<b>Bibliography</b>	<b>150</b>

## List of Figures

2.1	QCD description of $p\bar{p} \rightarrow b\bar{b} + X$ . $x_1 P_1$ and $x_2 P_2$ represent the momenta of the incoming partons. $k$ represents the momenta of the outgoing $b$ quark . . . . .	9
2.2	Lowest order Feynman diagrams contributing to $p\bar{p} \rightarrow b\bar{b}$ . . . . .	10
2.3	Higher order Feynman diagrams contributing to $p\bar{p} \rightarrow b\bar{b} + X$ . . . . .	11
2.4	The inclusive cross section for the production of a heavy quark with mass $4.75 \text{ GeV}/c^2$ and rapidity $ y  \leq 1.0$ , at the Tevatron. . . . .	13
2.5	The fragmentation of a $b$ quark into a $B_u^-$ meson. . . . .	14
2.6	Spectator diagram for the decay $B_u^- \rightarrow J/\psi + K^-$ . . . . .	17
3.1	The Fermilab Tevatron layout. . . . .	22
4.1	An event display showing an $r - z$ projection of the VTPC wire hits. . . . .	26



4.2	An event display showing an $r-\phi$ projection of the CTC wire hits, with reconstructed tracks overlayed. On the left is a close-up which shows the cell geometry in Superlayers 8,7,6,5, and 4 from the top through the bottom, respectively. . . . .	28
4.3	The muon chamber (CMU) geometry. . . . .	32
5.1	Relating an angle measurement in the CMU to the $P_T$ measurement in the CTC. . . . .	35
5.2	Level-1 trigger efficiency using the Cosmic ray sample. The error bars represent the binomial error associated with taking the ratio of two numbers. . . . .	39
5.3	Hadronic energy distribution for cosmic ray muon sample. The error bars are statistical. . . . .	40
5.4	Trigger efficiency of background events. The error bars are binomial.	41
5.5	Efficiency for muons from kaon decay, relative to primary muons. . .	43
5.6	Hadronic energy distribution for the candidate muon sample. The error bars are statistical. . . . .	45
5.7	Fitting the hadronic energy distribution. The error bars are statistical.	46
5.8	Shape of the hadronic energy distribution for background. . . . .	48

5.9	Fitting the HAD distribution for data with no trigger requirement.	
	The data is organized into the following bins of $P_T$ : (a) $P_T$ range (2.0 – 2.5), (b) $P_T$ range (2.5 – 3.0), (c) $P_T$ range (3.0 – 3.5), (d) $P_T$ range (3.5 – 4.0). . . . .	50
5.10	Fitting the HAD distribution for data with no trigger requirement.	
	The data is organized into the following bins of $P_T$ : (a) $P_T$ range (4.0 – 5.0), (b) $P_T$ range (5.0 – 6.0), (c) $P_T$ range (6.0 – 7.0), (d) $P_T$ range (7.0 – 8.0). . . . .	51
5.11	Fitting the HAD distribution for data which passed the Level-1 muon trigger.. The data is organized into the following bins of $P_T$ : (a) $P_T$ range (2.0 – 2.5), (b) $P_T$ range (2.5 – 3.0), (c) $P_T$ range (3.0 – 3.5), (d) $P_T$ range (3.5 – 4.0). . . . .	52
5.12	Fitting the HAD distribution for data which passed the Level-1 muon trigger.. The data is organized into the following bins of $P_T$ : (a) $P_T$ range (4.0 – 5.0), (b) $P_T$ range (5.0 – 6.0), (c) $P_T$ range (6.0 – 7.0), (d) $P_T$ range (7.0 – 8.0). . . . .	53
5.13	Level-1 muon trigger efficiency measurement as a function of muon CTC track $P_T$ . The error bars are binomial. . . . .	54

5.14	Effect of gaussian smearing on muon chamber angle, as a function of track $P_T$ . The two solid straight lines indicate the region in angle $\alpha$ accepted by the Level-1 trigger. . . . .	56
5.15	Fitting function test on Monte Carlo data sample. . . . .	57
5.16	Fit of the Level-1 muon trigger efficiency. The error bars are binomial. . . . .	58
5.17	Efficiency of the CFT as a function of muon CTC track $P_T$ . The error bars are binomial. . . . .	61
6.1	The measured CTC position resolution and wire efficiency. . . . .	71
6.2	CTC track reconstruction efficiency as a function of track $P_T$ . The error bars are binomial. . . . .	73
6.3	CTC track reconstruction efficiency as a function of track detector $\eta$ . The error bars are binomial. . . . .	74
6.4	CMU track reconstruction results in the $xy$ plane. In (a) we show the residual distribution and in (b) we show the distribution of the number of hits attached to the reconstructed track. . . . .	79
6.5	CMU track reconstruction results in the $zy$ plane. In (a) we show the residual distribution and in (b) we show the distribution of the number of hits attached to the reconstructed track. . . . .	80
6.6	The distributions for $M_{I_x}$ (top) and $M_{I_z}$ (bottom) obtained using the cosmic ray muon sample. The error bars are statistical. . . . .	86

6.7	Illustration of the effects of multiple scattering on the path of a charged track from the inner beam pipe out through the CTC. . . . .	88
6.8	$\mu^+\mu^-K^-$ mass distributions showing the effects of adding constraints. Figure (a) shows the $\mu^+\mu^-K^-$ mass distribution with no constraints added, (b) has a vertex constraint, (c) has a vertex and pointing, and (d) has a combined vertex, pointing, and mass constraint. . . . .	92
7.1	Invariant mass of the $\mu^+\mu^-$ data sample for the cuts described in the text. . . . .	95
7.2	Fit results in the $\mu^+\mu^-$ data sample. (a) $\mu^+\mu^-$ mass distribution in the region of the $J/\psi$ meson. (b) $\mu^+\mu^-$ mass distribution in the region of the $\psi(2S)$ meson. (c) $\mu^+\mu^-$ mass distribution in the region of the $\Upsilon(1S)$ and $\Upsilon(2S)$ mesons. . . . .	96
7.3	$J/\psi \pi^+\pi^-$ mass distribution in the region of the $\psi(2S)$ meson. . . .	99
7.4	The $P_T$ spectrum for candidate $K^-$ observed in the data compared with the Monte Carlo spectrum for $K^-$ in the decay $B_u^- \rightarrow J/\psi + K^-$ . The error bars are statistical. . . . .	101
7.5	The $P_T$ spectrum for candidate $B^-$ mesons observed in the data compared with the Monte Carlo spectrum for true $B^-$ mesons. The error bars are statistical. . . . .	102

7.6	$J/\psi + K^-$ mass distribution in the region of the $B^-$ meson, for the cuts described in the text. . . . .	104
7.7	$J/\psi + K^-$ mass distribution after lowering the muon $P_T$ cut from 3.0 to 2.0 GeV/c . . . . .	105
7.8	$J/\psi + K^-$ mass distribution after lowering the kaon $P_T$ cut from 2.0 to 1.0 GeV/c . . . . .	106
7.9	$\mu^+\mu^-$ mass distribution observed in the data. The central shaded region is used in the search for $B_u^- \rightarrow J/\psi + K^-$ . The shaded regions on the sides are used to estimate the effect of <i>fake</i> $J/\psi$ 's. . . . .	107
7.10	Background to the observed $J/\psi K^-$ mass distribution from <i>fake</i> $J/\psi$ 's.	108
7.11	Background to the observed $J/\psi K^-$ mass distribution from random tracks in the events. . . . .	110
7.12	Fitting the observed $B_u^- \rightarrow J/\psi + K^-$ sample. For all figures the histogram is the data, the curve is the fit. In Figure (a) the mass and width are floated, in (b) the mass and width are fixed, in (c) the mass is floated, the width is fixed, and in (d) the mass is fixed, the width is floated. . . . .	114
8.1	UA1 measurement of the $b$ quark cross section. . . . .	117
8.2	The calculated $b$ -quark rapidity spectrum. . . . .	118

8.3	The calculated cross section overlayed with the fit curve described in the text. For the fit curve, $n = 3.01$ . . . . .	120
8.4	The calculated cross section overlayed with the fit curves described in the text. The fit curve in (a) is described by the parameter $n = 3.42$ . The fit curve in (b) is described by the parameter $n = 2.63$ . . . . .	121
8.5	Reconstruction efficiency as a function of the fit parameter $n$ described in the text. The error bars are binomial. . . . .	122
8.6	The calculated error on the track parameters $Z_0$ , $\phi_0$ , and $c$ ; Monte Carlo vs data. . . . .	125
8.7	The calculated error on the track parameters $D_0$ and $\cot \theta$ ; Monte Carlo vs data. . . . .	126
8.8	Detector rapidity spectra for muons and kaons as predicted by the Monte Carlo model. The error bars are statistical. . . . .	127
8.9	Decay radius of kaons with $P_T \geq 2.0$ GeV/c , as predicted by the Monte Carlo model. The error bars are statistical. . . . .	129
8.10	Comparison of the fit quality of the CMU track reconstruction observed in the data with that seen in the Monte Carlo model. The top curve is the fit quality in the $xy$ plane and the bottom is the fit quality in the $zy$ plane. . . . .	130

8.11	Comparison of the normalized matching variables observed in the data with that seen in the Monte Carlo model. The top curve is the normalized $x$ -intercept match, $(I_X/\sigma_X)$ , and the bottom curve is the normalized $z$ -intercept match, $(I_Z/\sigma_Z)$ . . . . .	131
8.12	Mapping the cracks in the muon chambers, comparison of the Monte Carlo model <i>vs</i> data. . . . .	133
8.13	Comparison of the $K^- P_T$ spectrum observed in the data with the Monte Carlo prediction. The error bars are the statistical errors of both the data and the background added in quadrature. . . . .	136
8.14	Comparison of the $B^-$ meson $P_T$ spectrum observed in the data with the Monte Carlo prediction. The error bars are the statistical errors of both the data and the background added in quadrature. . . . .	137
8.15	Comparison of the $B^-$ meson rapidity spectrum observed in the data with the Monte Carlo prediction. The error bars are the statistical errors of both the data and the background added in quadrature. . .	138
8.16	Illustration of $P_T^{min}$ . . . . .	140
8.17	The rapidity distribution of $b$ quarks which contribute to our final sample of observed $B_u^- \rightarrow J/\psi + K^-$ events. The error bars are statistical.	141
9.1	The $b$ quark production cross section using all current CDF measurements. Also shown is the theoretical calculation of Nason <i>etal</i> . . . .	147

## List of Tables

2.1	Experimental Branching Ratios for $B$ Meson Decay . . . . .	18
6.1	Results of a test of constrained fits on a Monte Carlo sample of $B_u^- \rightarrow J/\psi + K^-$ (with $J/\psi \rightarrow \mu^+\mu^-$ ) . . . . .	91
7.1	Results of fitting the $\mu^+\mu^-$ sample, showing for each resonance the fitted mass, width, and number of events ( $N^{rec}$ observed. The last column shows the deviation in % of the mass we observe from the world average. . . . .	94
7.2	Results of fitting the observed $B_u^- \rightarrow J/\psi + K^-$ sample. . . . .	113
8.1	Reconstruction Efficiencies and systematic errors. . . . .	132
8.2	Widths observed in the data compared with Monte Carlo. . . . .	134
8.3	Parameters used in the $b$ quark production cross section calculation. . . . .	143
8.4	Systematic uncertainties in the cross section calculation. . . . .	143
9.1	Measurements of the $b$ quark cross section at CDF, compared to the theoretical calculation. . . . .	146



## Chapter 1

### Introduction

This thesis describes the full reconstruction of  $B$  mesons at the Fermilab Tevatron by the CDF collaboration [1].  $B$  mesons have been studied extensively in a number of experiments, and consequently, much is known about their properties. The  $B$  lifetime is known to be large [2], neutral  $B$  mesons are found to undergo mixing [3], and a large number of  $B$  decay branching ratios have been tabulated [4][5].

What can a study of the  $B$  meson production cross section at  $\sqrt{s} = 1.8 \text{ TeV}/c^2$  tell us? The production of  $B$  mesons at hadron colliders is understood to be the result of the underlying production and subsequent hadronization (or fragmentation) of  $b$  quarks. The  $b$  quark production cross section at this energy has been calculated [6][7][8] and the uncertainty in this calculation is dependent on a number of parameters. These include the value of the  $b$  quark mass and the strength of  $\Lambda_{QCD}$ . In addition, the production of  $b$  quarks at this energy is dominated by the process of gluon fusion, and so is sensitive to the gluon distribution in the proton. Therefore,

a precise measurement of  $B$  meson production can help reduce the uncertainties in these parameters.

This thesis describes the first measurement of the  $b$  quark and  $B$  meson production cross sections at  $\sqrt{s} = 1.8 \text{ TeV}/c^2$ . This measurement is accomplished directly, through the observation of the exclusive decay  $B_u^- \rightarrow J/\psi + K^-$ , in which the  $J/\psi$  is identified via its decay into muons,  $J/\psi \rightarrow \mu^+ \mu^-$ . The substantial decay branching ratio of the  $J/\psi$  into  $\mu^+ \mu^-$  is crucial to the measurement, since the dimuons provide a natural and easily implemented trigger.

The reconstruction of  $B$  mesons begins with the identification of dimuons that are consistent with the decay of a  $J/\psi$ . The other decay products of the  $B$  meson are identified only as charged particles, as the CDF detector has no particle identification capability (excepting muons and electrons). Since the number of charged tracks in these events is of the order of 20, requirements must be placed on the charged tracks to increase the probability that the correct track is chosen. In the case of the decay  $B_u^- \rightarrow J/\psi + K^-$ , the  $K^-$  is required to have large transverse momentum. Once all the decay products have been identified, the invariant mass of the system is calculated, and compared to the expectation from Monte Carlo calculations.

The reconstructed  $B_u^- \rightarrow J/\psi + K^-$  sample is based on an integrated luminosity of  $2.6 \text{ pb}^{-1}$  taken during the 1988-89 colliding beam run at the Fermilab Tevatron. Using this sample, we have extracted the  $b$ -quark and  $B_u^-$  meson production cross

sections.

.

## Chapter 2

### Theory

#### 2.1 The Standard Model

The Standard Model [9] of particle physics is described by the gauge group  $SU(3) \times SU(2) \times U(1)$ . This model describes nature in terms of fundamental spin- $\frac{1}{2}$  particles called fermions. The forces that govern the interactions of the fermions are mediated by spin-1 vector gauge bosons. The gauge bosons are the photon, the massless particle that carries the electromagnetic force; the gluon, the massless particle that carries the strong force; and the very heavy particles  $W^\pm$  and  $Z^0$ , which carry the charged and neutral weak forces.

The fermions are grouped in three generations of quarks and leptons:

$$\begin{array}{ccc} \begin{pmatrix} u \\ d \end{pmatrix} & \begin{pmatrix} c \\ s \end{pmatrix} & \begin{pmatrix} t \\ b \end{pmatrix} & \text{quarks} \\ \\ \begin{pmatrix} \nu_e \\ e \end{pmatrix} & \begin{pmatrix} \nu_\mu \\ \mu \end{pmatrix} & \begin{pmatrix} \nu_\tau \\ \tau \end{pmatrix} & \text{leptons} \end{array}$$

where only the  $t$  quark has yet to be observed.

The electromagnetic interaction is well described by quantum electrodynamics (QED) [10], in which the interaction is carried by the massless photon. The weak interactions were first observed in the case of nuclear  $\beta$  decay, and are now understood to be mediated by the massive bosons  $Z^0$  and  $W^\pm$ . Glashow, Weinberg and Salam [11] unified these two interactions into a single electroweak interaction which is described by the gauge groups  $SU(2) \times U(1)$ .

The strong interaction is carried by gluons, and only affects quarks. The strong interactions involve a concept called color, which plays a role similar to that of charge in electromagnetism. In contrast to both the electroweak and electromagnetic interactions, both the quarks and the gluons carry the color charge. This non-Abelian nature of the strong interactions explains the conflicting properties of quarks. Quarks are only observed in combination with other quarks in hadrons (mesons or baryons), yet when these hadrons are probed at high energies, the quarks appear to behave as free particles (a property known as asymptotic freedom). The gauge theory that describes strong interactions is called quantum chromodynamics [13] (QCD) and it involves the symmetry group  $SU(3)$ .

The Lagrangian that governs the QCD interaction is given by [15]:

$$\mathcal{L} = -\frac{1}{4}F_a^{\mu\nu}F_{a\mu\nu} + \bar{\psi}_j(i\gamma_\mu D_{jk}^\mu - M_{jk})\psi_k$$

where the index  $a = 1, \dots, 8$  refers to the eight gluon fields, the indices  $j, k = 1, 2, 3$

refer to the three possible colors each quark can have.  $F_a^{\mu\nu}$  is the gluon field tensor, given by:

$$F_a^{\mu\nu} = \partial^\mu G_a^\nu - \partial^\nu G_a^\mu - gf_{abc}G_b^\mu G_c^\nu$$

where the  $G_a^\nu$  are the 8 gluon fields,  $g$  is the strong coupling constant, and  $f_{abc}$  are the structure constants of  $SU(3)$ .  $D_{jk}^\mu$  is the covariant derivative that acts on the quark fields  $\psi_k$ , and is given by:

$$D_{jk}^\mu = \delta_{jk}\partial^\mu + ig(T_a)_{jk}G_a^\mu$$

where the  $T_a$  are the  $SU(3)$  generators. Finally,  $M_{jk}$  can be written as  $M\delta_{jk}$ , where  $M$  is a  $6 \times 6$  matrix in flavor space, and  $\delta_{jk}$  is the Kronecker delta in the color indices. From this Lagrangian, one can derive the Feynman rules governing the interactions of quarks and gluons. The above Lagrangian contains a quark-gluon vertex, as well as vertices involving three and four gluons. By writing down all allowed Feynman graphs corresponding to the production of a heavy quark pair, one can then proceed to a calculation of the production cross section.

It should be noted that all existing data concerning elementary particles is consistent with the Standard Model. However, the major drawback to this model is that it has 21 free parameters that must be measured and put into the model by hand. As a result most particle physicists do not believe that the Standard Model is the final answer, and much of the current effort in this field is devoted to either searches for physics lying outside the model, or stringent tests of the model in hope of finding a

discrepancy. The  $b$  quark mass is one of the free parameters in the Standard Model, and is also one of the major uncertainties in the calculation of  $b$  quark production at  $\sqrt{s} = 1.8 \text{ TeV}/c^2$ . It follows that a precise measurement of  $b$  quark production may help reduce the uncertainty on the value of the  $b$  quark mass.

## 2.2 $b$ quark Production

Within the scheme of perturbative QCD [14], one can calculate the cross section for  $p\bar{p} \rightarrow b\bar{b} + X$ . One finds that  $b$  quark production is dominated by gluon-gluon interactions, and the typical momentum of the produced  $b$  quark is of the same order as the  $b$  quark mass (i.e.  $\sim 5 \text{ GeV}/c$ ). The cross section viewed as a function of the transverse momentum of the  $b$  quark peaks around the  $b$  quark mass, and falls sharply above this. Since the CDF detector is sensitive to processes which have transverse momenta above  $\sim 7 \text{ GeV}/c$ , the bulk of the cross section cannot be observed.

A schematic description of the process  $p\bar{p} \rightarrow b\bar{b} + X$  is shown in Figure 2.1. The incoming proton (anti-proton) is made up of the quark combination  $uud$  ( $\bar{u}\bar{u}\bar{d}$ ). A proper treatment shows that in addition to these *valence* quarks, there surrounds the proton and anti-proton a cloud of virtual gluons and quark-antiquark pairs  $u\bar{u}$ ,  $d\bar{d}$ ,  $s\bar{s}$ , etc. When probed at high enough momentum transfer (or  $q^2$ ), the quarks and gluons are considered as free partons. The probability of finding a particular parton is given

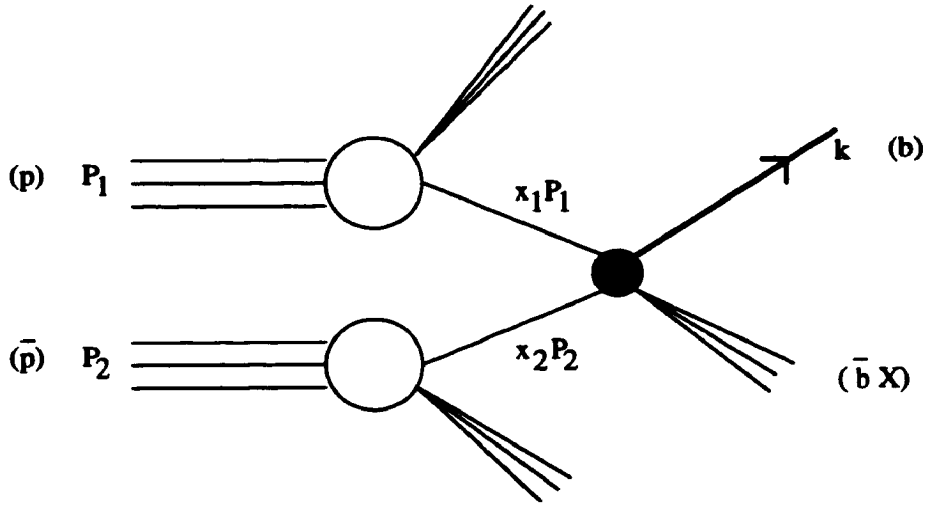


Figure 2.1: QCD description of  $p\bar{p} \rightarrow b\bar{b} + X$ .  $x_1 P_1$  and  $x_2 P_2$  represent the momenta of the incoming partons.  $k$  represents the momenta of the outgoing  $b$  quark.

by distributions that depend on the  $q^2$  of the probe [16].

To calculate the cross section for  $p\bar{p} \rightarrow b\bar{b} + X$ , one first calculates the partonic cross section, i.e. the cross section for parton  $i$  from the proton to interact with parton  $j$  from the anti-proton to form the product  $b\bar{b} + X$ . This cross section will depend, among other things, on the momenta of partons  $i$  and  $j$ . One then sums over the partons in the proton and anti-proton, and integrates over the allowed momenta for the two partons, to get the full cross section. The partonic cross sections can be calculated as a perturbative series in the QCD coupling constant  $\alpha_s(q^2)$  ( $= g/4\pi$ ). The Feynman diagrams which contribute to the lowest order ( $\alpha_s^2$ ) partonic cross section are shown in Figure 2.2. Some of the higher order ( $\alpha_s^3$ ) diagrams are shown in Figure 2.3.



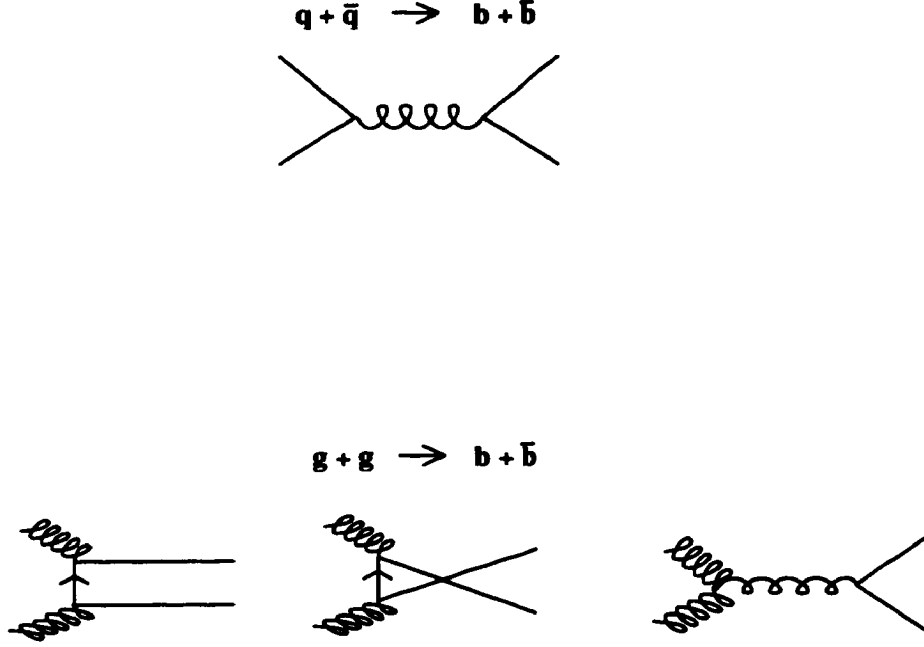


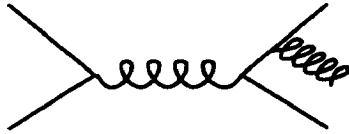
Figure 2.2: Lowest order Feynman diagrams contributing to  $p\bar{p} \rightarrow b\bar{b}$ .

The invariant cross section is given by [17]

$$E \frac{d^3\sigma}{d^3k} = \sum_{i,j} \int dx_1 dx_2 \left( E \frac{d^3\hat{\sigma}_{ij}(x_1 P_1, x_2 P_2, p, m, \mu)}{d^3k} \right) F_i^A(x_1, \mu) F_j^B(x_2, \mu)$$

where the sum is over the light partons ( $i, j = u, \bar{u}, d, \bar{d}, s, \bar{s}, c, \bar{c}, g$ ), the integrals are over the longitudinal momentum fractions of the partons,  $\hat{\sigma}$  is the partonic cross section,  $P_1$  ( $P_2$ ) is the momentum of the incoming proton (anti-proton),  $F_i^A(x_1, \mu)$  is the probability for finding parton  $i$  in the proton with momentum fraction  $x_1$  and  $\mu$  represents the scale (or  $q^2$ ) of the interaction. In general, one could distinguish between the scale in  $\hat{\sigma}$  (called the renormalization scale) and the scale in  $F_i^A$  (called the factorization scale), but for simplicity they are taken to be equal.  $\mu$  is typically taken to be of the order of the mass scale of the process under consideration. In the

$$q + \bar{q} \rightarrow b + \bar{b} + g$$



$$g + g \rightarrow b + \bar{b} + g$$

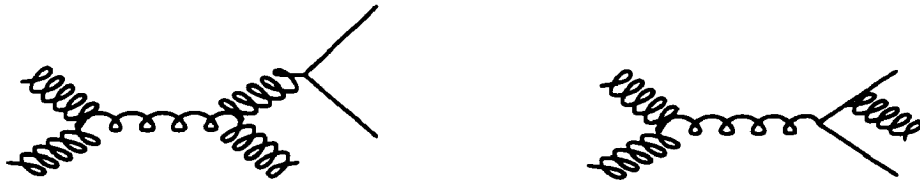


Figure 2.3: Higher order Feynman diagrams contributing to  $p\bar{p} \rightarrow b\bar{b} + X$  .

differential calculation, there are two relevant scales: the mass  $m$  of the heavy quark and its transverse momentum  $P_T$ . To reduce the sensitivity to the scale,  $\mu$  is chosen to be  $\sqrt{P_T^2 + m^2}$ . The results of the full  $O(\alpha_S^3)$  calculation by Nason, Dawson, and Ellis [6] are shown in Figure 2.4.

### 2.3 $b$ quark Fragmentation

Quark fragmentation describes the process in which one quark combines with an anti-quark (or quark/anti-quark pair) to form a meson (or baryon) which can then be observed in the laboratory. This process is believed to be necessary since nature seems to demand color neutral objects and quarks carry net color charge. For example, a  $b$  quark carrying the color index *red*, can combine with a  $\bar{u}$  quark carrying the color index *anti - red* to form a color-neutral  $B_u^-$  meson. This process is illustrated in Figure 2.5.

$b$  quark fragmentation actually implies two quite distinct processes. The first determines how much of the parent  $b$  quark energy is carried off by the resulting  $B$  meson. The second describes the probability that a given  $b$  quark will pair with a  $\bar{u}$ ,  $\bar{d}$ ,  $\bar{s}$ , or  $\bar{c}$  quark.

The experimental observation is that the  $B$  meson carries away most of the energy of the parent  $b$  quark. Since this process is highly non-perturbative, it has so far only been described by phenomenological models. One model due to Peterson et al.

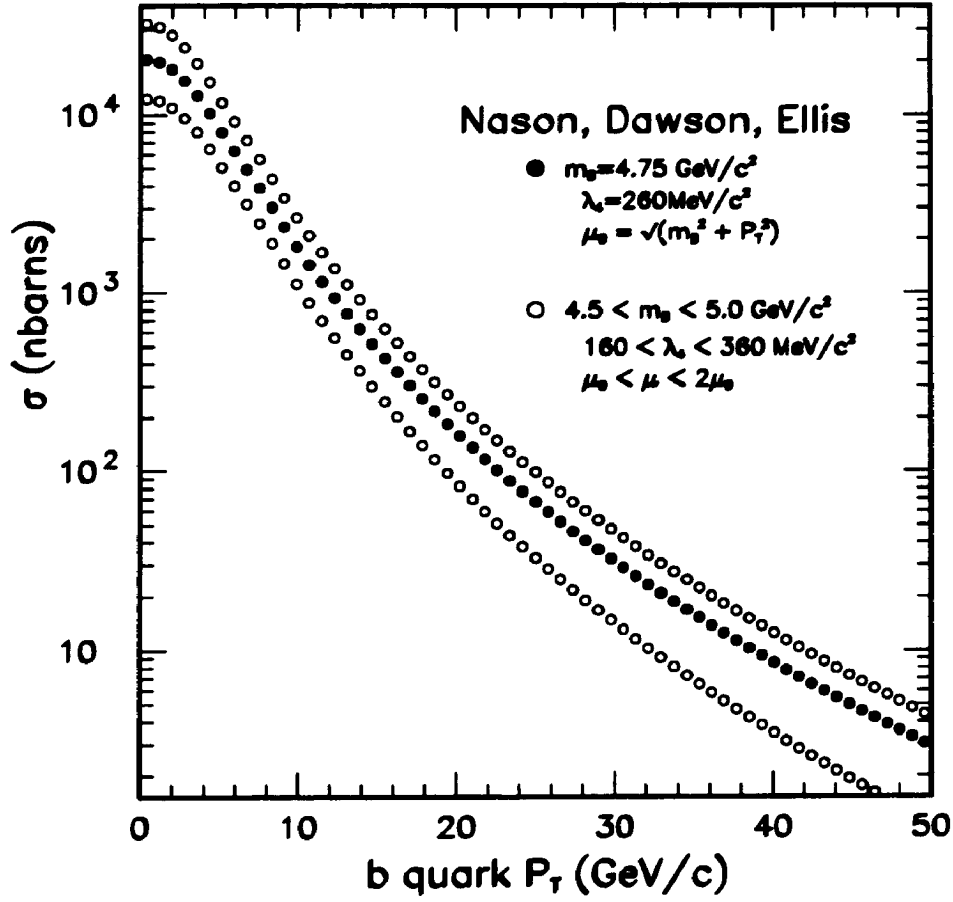


Figure 2.4: The inclusive cross section for the production of a heavy quark with mass  $4.75 \text{ GeV}/c^2$  and rapidity  $|y| \leq 1.0$ , at the Tevatron.

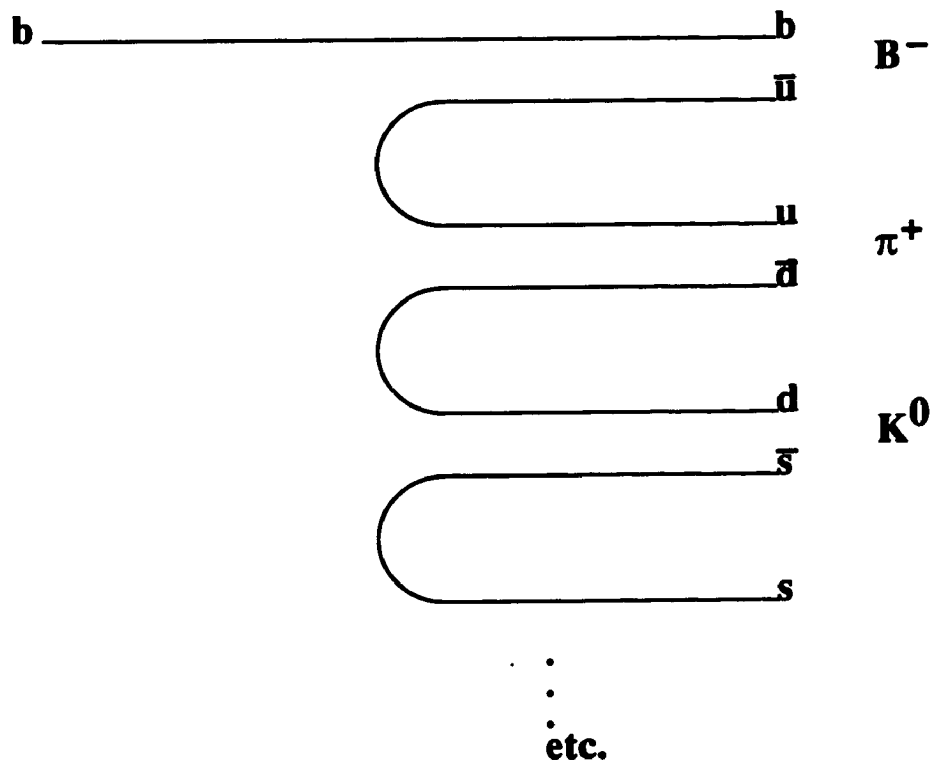


Figure 2.5: The fragmentation of a  $b$  quark into a  $B_u^-$  meson.

[18] describes fragmentation of heavy quarks (the  $b$  and  $t$  quarks, and possibly the  $c$  quark) in terms of the quantum mechanical transition probability for the process

$$Q \rightarrow Q\bar{q} + q$$

where  $Q$  represents the heavy quark, and  $Q\bar{q}$  represents the primary meson. The quark  $q$  is itself fragmented, and the process continues until energy conservation cuts it off. (A resulting problem with these models is that in general a light quark is left over at the end of this process.) One first defines the variable  $z$ , which corresponds roughly to the fraction of energy the meson takes from the quark:

$$z = \frac{(E_m + p_m^{\parallel})}{(E_q + p_q)}.$$

Here,  $E_q$  and  $p_q$  are the energy and momentum of the fragmenting quark.  $E_m$  and  $p_m^{\parallel}$  are the energy of the meson and the momentum of the meson parallel to the quark direction. Then, using simple kinematic arguments, one can show that the form of the probability distribution for fragmentation is:

$$f(z) \propto \frac{1}{z \left[ 1 - \frac{1}{z} - \frac{\epsilon_Q}{(1-z)} \right]^2}.$$

$\epsilon_Q$  is a parameter that must be measured experimentally for the heavy quark  $Q$ . It is expected to be of the form:

$$\epsilon_Q \propto \frac{M_q^2}{M_Q^2}$$

the ratio of the masses of the light and heavy quarks which form the primary meson in the fragmentation process.

The Peterson model seems to adequately describe the current data on heavy quark fragmentation, and the result for  $\epsilon_b$  from a review of many experiments is [19]:

$$\epsilon_b = 0.006 \pm 0.002.$$

The next question that must be answered concerns the flavor of the light quark  $q$  in the fragmentation process  $Q \rightarrow Q\bar{q} + q$ . A number of models [20] assume that the probability to produce a  $q\bar{q}$  pair in the fragmentation process, is proportional to  $e^{-m^2}$  where  $m$  is the mass of the quark. This yields:

$$u\bar{u} : d\bar{d} : s\bar{s} : c\bar{c} = 1 : 1 : 0.33 : 10^{-11}$$

For example, one can define a parameter called the strangeness suppression factor,  $\lambda_s$ , as the ratio of the probability to produce an  $s\bar{s}$  pair relative to a  $u\bar{u}$  or  $d\bar{d}$  quark pair. The above model predicts  $\lambda_s = 0.33$ , which is in agreement with  $\lambda_s = 0.33 \pm 0.02$  observed by a number of experiments [21]. A slightly larger value of  $\lambda_s = 0.40 \pm 0.05$  has been reported by the CDF collaboration [22]. Using this value, we obtain the probability for a  $b$  quark to fragment into the various possible mesons or baryons as:

$$B_u : B_b : B_s : B_{baryon} = 0.375 : 0.375 : 0.15 : 0.10$$

where an assumption of a 10% probability for a  $b$  quark to fragment into a  $B$  baryon is also indicated.

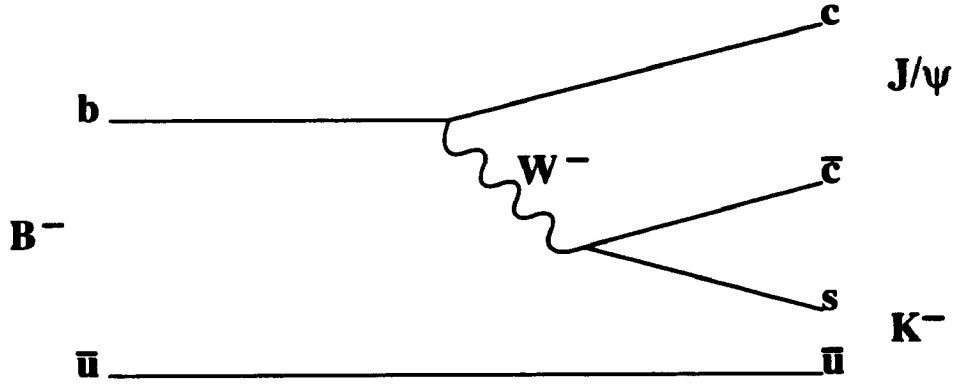


Figure 2.6: Spectator diagram for the decay  $B_u^- \rightarrow J/\psi + K^-$ .

#### 2.4 $B_u^- \rightarrow J/\psi + K^-$ Decay

A successful description [23] of the decay  $B_u^- \rightarrow J/\psi + K^-$  has been obtained with the Spectator Model. In this model, the  $b$  quark in the  $B_u^-$  meson decays weakly and independently of the  $\bar{u}$  quark, with a lifetime of approximately 1.3 psec. The spectator graph for this decay is shown in Figure 2.6. In this figure, the  $b$  quark decays into a  $c$  quark by emitting a virtual  $W^-$  boson, with a strength modified by the  $CKM$  [24] parameter  $V_{bc}$ . The  $W^-$  can then decay into the following:

$$W^- \rightarrow (e\bar{\nu}_e) \text{ or } (\mu\bar{\nu}_\mu) \text{ or } (\tau\bar{\nu}_\tau) \text{ or } (\bar{c}s) \text{ or } (\bar{u}d)$$

with the two decays into quark pairs each having a weight of 3 due to the three color possibilities. Of course, the relevant decay for this analysis is  $W^- \rightarrow \bar{c}s$ .

Finally, one has to also factor in the probability for the  $c\bar{c}$  pair to form a  $J/\psi$  bound state. An additional theoretical consideration is the idea of color suppression. Since the two mesons formed in the spectator decay must each carry the color of their



Table 2.1: Experimental Branching Ratios for  $B$  Meson Decay

Mode	CLEO measurement (%)	ARGUS measurement (%)
$B \rightarrow J/\psi + X$	$1.09 \pm 0.16 \pm 0.21$	$1.07 \pm 0.16 \pm 0.22$
$B \rightarrow \psi' + X$	—	$0.46 \pm 0.17 \pm 0.11$
$B_u^- \rightarrow J/\psi + K^-$	$0.09 \pm 0.06 \pm 0.02$	$0.07 \pm 0.04$

parent quarks, the  $\bar{c}$  and  $s$  quarks from the virtual  $W$  can have only 1 of the possible 3 color combinations in order to match the color of the  $b$  and  $\bar{u}$  quarks. This results in a suppression of this decay. This effect does seem to play a role in  $B_u^- \rightarrow J/\psi + K^-$  decays [25].

The  $B$  meson decays relevant to this analysis have been measured at CLEO [4] and ARGUS [5]. These two experiments run on the  $\Upsilon(4S)$  resonance, and utilize the fact that the  $\Upsilon(4S)$  decays primarily to  $B\bar{B}$  pairs. The decay branching ratios are summarized in Table 2.1.

## Chapter 3

### The Fermilab Tevatron

The Collider Detector at Fermilab (CDF) is a general purpose detector situated at the B0 interaction region in the Fermilab Tevatron. The Fermilab Tevatron[27, 28, 29] is the highest energy accelerator in the world, employing counter-rotating beams of protons and anti-protons which collide with a center-of-mass energy of 1.8 TeV.

The layout of the Tevatron is shown in figure 3.1. The process of colliding protons with anti-protons begins with the extraction of protons from a bottle of hydrogen gas. The protons are then ionized to form  $H^-$ . The  $H^-$  ions are first accelerated in a Cockcroft-Walton to 750 keV, then in a linear accelerator (the Linac) of length 150 m, where they reach an energy of 200 MeV. The  $H^-$  ions then are focused on a thin carbon foil which strips off the 2 electrons. The bare protons are then transferred to a circular accelerator of circumference 475 m called the Booster, which increases the proton energy to 8 GeV. At this stage the protons are grouped in approximately 7 bunches, with each bunch containing approximately  $2 \times 10^{10}$  protons. The Booster

feeds the proton bunches to the Main Ring (circumference 6300 m) which accelerates them to 150 GeV. At this stage all of the bunches are combined into one containing approximately  $7 \times 10^{10}$  protons. Finally, the bunch is transferred to the Tevatron, where it reaches its maximum energy of 900 GeV. The Tevatron lies right below the Main Ring, and has the same circumference. In the 1988-89 run, the Tevatron was operated in 6 bunch mode, so this process was repeated 6 times.

The cycle for anti-protons ( $\bar{p}$  's) is different, mainly due to the difficulty of producing them. Protons are first taken through the above cycle of Linac, Booster, and Main Ring. In this case, however, the Main Ring accelerates the protons to only 120 GeV. The protons are focused onto a copper target, and the resulting by-products contain anti-protons. Anti-protons with energy near 8 GeV are collected and sent to the Debuncher where the momentum spread of the  $\bar{p}$  sample is reduced. The anti-protons are collected or "stacked" in the Accumulator, and when the "stack" contains approximately  $27 \times 10^{10}$   $\bar{p}$  's, 6 bunches of approximately  $4.5 \times 10^{10}$   $\bar{p}$  's each are transferred to the Main Ring, and then to the Tevatron, just like the protons. The same magnets are used for the  $\bar{p}$  's, and they move in a direction opposite that of the protons. By the time the bunches reach the Tevatron, there are approximately  $3 \times 10^{10}$   $\bar{p}$  's per bunch.

The accelerator parameter that has the most impact on the physics possible (besides the center-of-mass energy) at the Tevatron is the Luminosity,  $\mathcal{L}$ . It is defined

by the following relation:

$$N = \mathcal{L}\sigma$$

where  $N$  is the observed rate of a given process (in  $\text{sec}^{-1}$ ) and  $\sigma$  is the production cross section for that process (in  $\text{cm}^2$ ). At the Tevatron, the luminosity is determined by:

$$L = \frac{N_p N_{\bar{p}} B f_0}{4\pi\sigma_b^2}$$

where  $N_p$  and  $N_{\bar{p}}$  are the number of protons and antiprotons per bunch,  $B$  is the number of bunches,  $f_0$  ( $=50$  kHz) is the revolution frequency, and  $\sigma_b$  is the cross sectional area of the bunches. For  $B = 6$  bunch operation, the crossing time (or the time between collisions) is  $\sim 3.33\mu\text{sec}$ . During the 1988-89 run, the average luminosity was  $1.6 \times 10^{30} \text{ cm}^{-2}\text{sec}^{-1}$ . A slightly more natural unit used instead of  $\text{cm}^2$  is the barn, with  $1 \text{ barn} = 10^{-24} \text{ cm}^2$ . Expressed in these units, the average luminosity during the 1988-89 run was  $1.6\mu\text{b}^{-1}\text{sec}^{-1}$ .

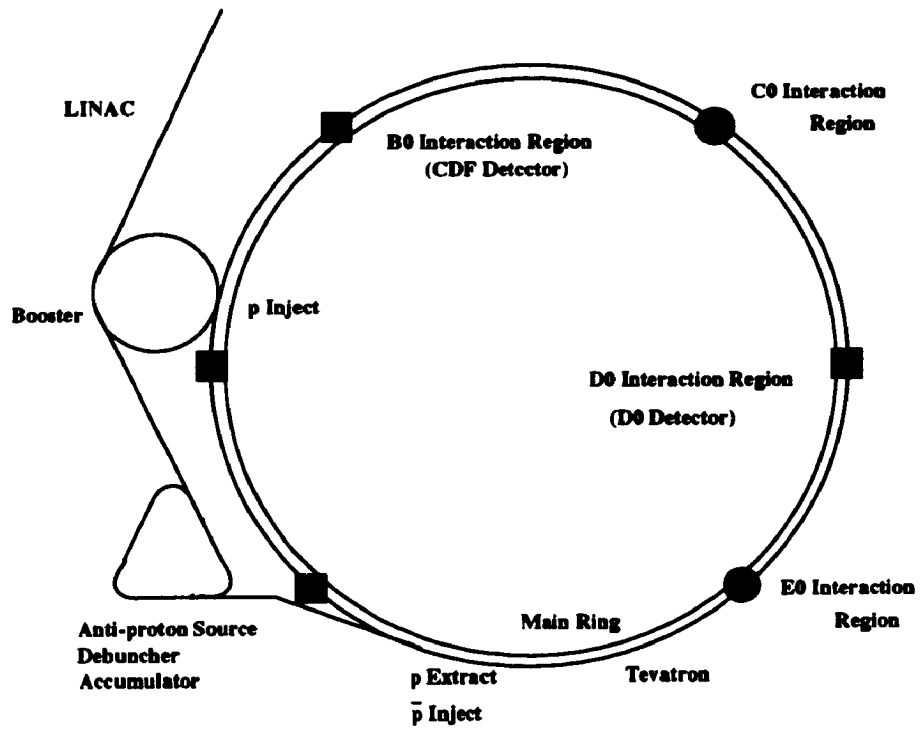


Figure 3.1: The Fermilab Tevatron layout.

## Chapter 4

### The CDF Detector

#### 4.1 Overview

A good description of the CDF detector is in reference [30]. The detector consists of a central region that emphasizes good charged particle tracking, fine-grained electromagnetic and hadronic calorimetry, and muon particle identification. The forward regions contain electromagnetic and hadronic calorimeters, and toroidal muon spectrometers. This analysis emphasizes the central parts of the detector, and detailed information on those aspects will follow.

Before describing the detector components relevant for this analysis, a few words should be said concerning the CDF coordinate system. The center of the coordinate system  $x = 0, y = 0, z = 0$  is located at the nominal  $p\bar{p}$  collision point. The positive  $z$  axis points along the direction of the protons. The positive  $x$  axis lies in the plane of the  $p\bar{p}$  ring and points out of the ring. The positive  $y$  axis is perpendicular to the plane of the  $p\bar{p}$  ring and points upwards.  $\phi$  is the azimuthal angle about the  $z$  axis

and  $\phi = 0$  is along the positive  $x$  axis.  $\theta$  is the polar angle, with  $\theta = 0$  along the positive  $z$  axis. A variable that is often used instead of  $\theta$  is the pseudorapidity  $\eta$ , which is defined as:

$$\eta = -\ln \tan \frac{\theta}{2}.$$

The pseudorapidity can also be related to the momentum of a particle:

$$\eta = \frac{1}{2} \ln \frac{P_{tot} + P_Z}{P_{tot} - P_Z}$$

where  $P_Z$  is the  $z$  component of the particle momentum, and  $P_{tot}$  is given by:

$$P_{tot} = \sqrt{P_X^2 + P_Y^2 + P_Z^2}.$$

In this form one can see how the pseudorapidity  $\eta$  is related to the rapidity  $y$  of a particle:

$$y = \frac{1}{2} \ln \frac{E_{tot} + P_Z}{E_{tot} - P_Z}$$

where  $E_{tot}$  is given by:

$$E_{tot} = \sqrt{M^2 + P_X^2 + P_Y^2 + P_Z^2}$$

and  $M$  is the mass of the particle.

## 4.2 The Vertex Time Projection Chamber (VTPC)

The VTPC [31] is the first detector system particles traverse on their way out from the  $p\bar{p}$  collision point. The VTPC is positioned immediately outside the beam pipe, which

is a 5.08 cm diameter Be tube with a wall thickness of 500  $\mu\text{m}$ . The active region of the VTPC extends from an inner radius of 7 cm out to a radius of 21 cm. It consists of 8 separate chambers which are mounted end-to-end along the beam direction. Each of these chambers is divided by a central high voltage grid into two 15.25 cm long drift regions. A chamber is further subdivided into 8 octants, with 24 sense wires per octant. Thus there are a total of 3072 sense wires for this system. As charged particles pass through the chamber they ionize the argon-ethane gas mixture (50% : 50%) and the resulting ionization electrons drift along the  $z$  direction, where they are collected on sense wires. As the drift speed in argon-ethane is  $\sim 46 \mu\text{m nsec}^{-1}$ , the maximum drift time is  $\sim 3.3 \mu\text{sec}$ , which is well matched to the  $\sim 3.33 \mu\text{sec}$   $p\bar{p}$  crossing time.

The VTPC is used to determine the position of the  $z$  vertex of the event. The  $z$  vertex distribution for events at CDF can be approximated by a Gaussian, with a mean of zero and width of 30 cm. This implies all vertices should be located well inside the 2.8 m long VTPC. The VTPC is sensitive to charged tracks within  $-3.5 \leq \eta \leq 3.5$ . An event display showing an  $r - z$  projection of the VTPC wire hits is shown in Figure 4.1.

### 4.3 The Central Tracking Chamber (CTC)

The CTC[32] is a cylindrical drift chamber designed for precise momentum measurements in the region  $-1.2 \leq \eta \leq 1.2$ . It is located outside of the VTPC and its active



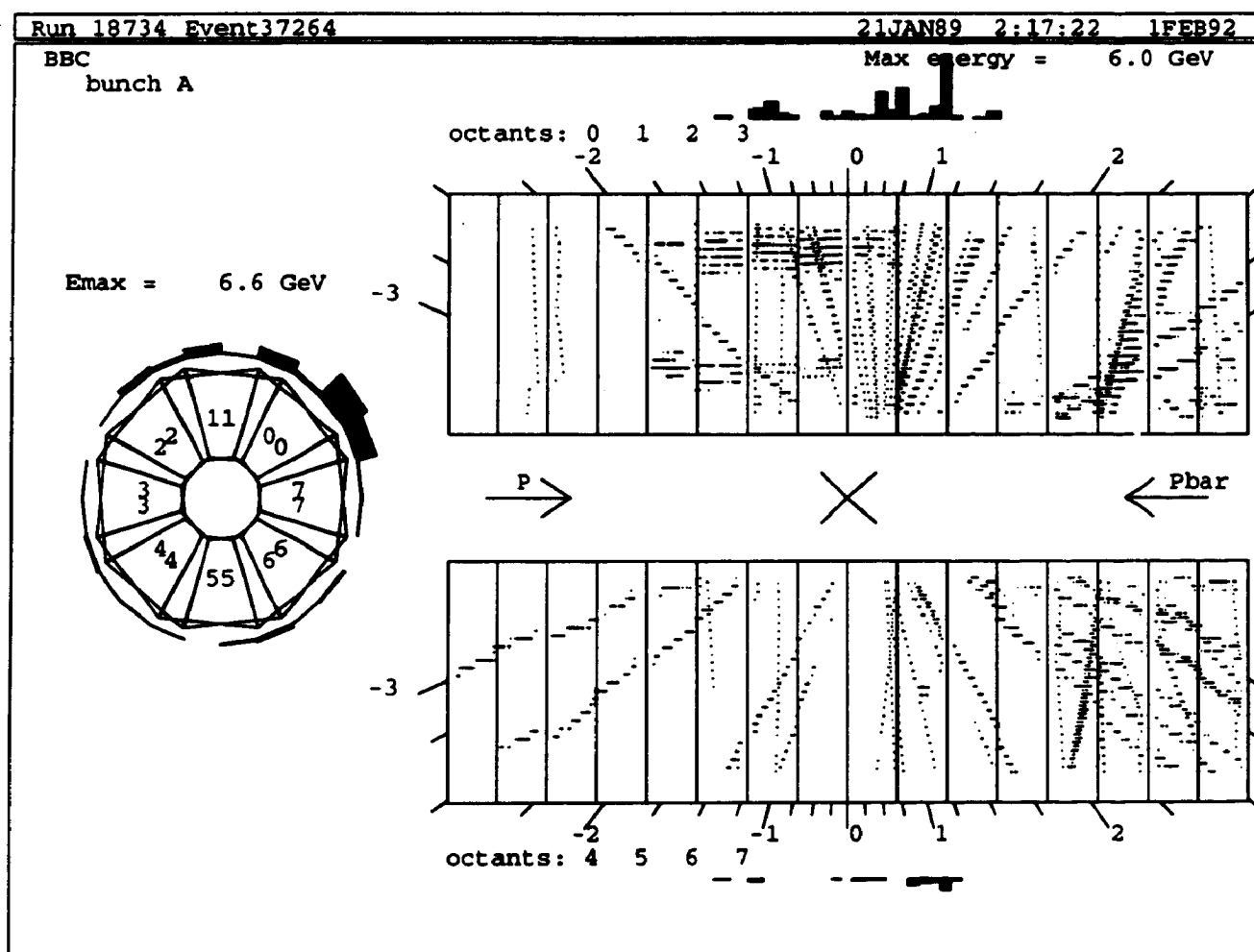


Figure 4.1: An event display showing an  $r - z$  projection of the VTPC wire hits.

region extends from a radius of 30 cm out to a radius of 130 cm. The chamber is composed of 84 layers of sense wires, which are grouped into 9 superlayers. The sense wires are strung along the  $z$  axis, and each wire measures the time of a hit relative to a global start time. 5 of the superlayers (called the axial layers) have 12 wires each, each of which is parallel to the beam line. These layers are sensitive to transverse  $r\phi$  information only. The remaining 4 superlayers (called the stereo layers) are each located between two axial superlayers. The wires in these superlayers are strung so that they make an angle of  $\pm 3^\circ$  relative to the beam line. These layers provide  $rz$  information.

Within each superlayer, the wires are grouped into cells, such that the maximum drift time in the argon-ethane-alcohol (49.6% : 49.6% : 0.8%) mixture is less than 800 nsec. An event display showing hits in the CTC along with reconstructed tracks is shown in Figure 4.2. The cell geometry for superlayers 4 through 8 is detailed in the left insert in this figure. The tilt of the sense wires is to compensate for the Lorentz angle, so that the drift direction of the electrons is purely azimuthal. The design resolution on each wire is  $\sim 200\mu m$ , and the double track resolution is less than 5 mm or 100 nsec. The total number of sense wires in the chamber is 6156, with each wire attached to a multi-hit TDC.

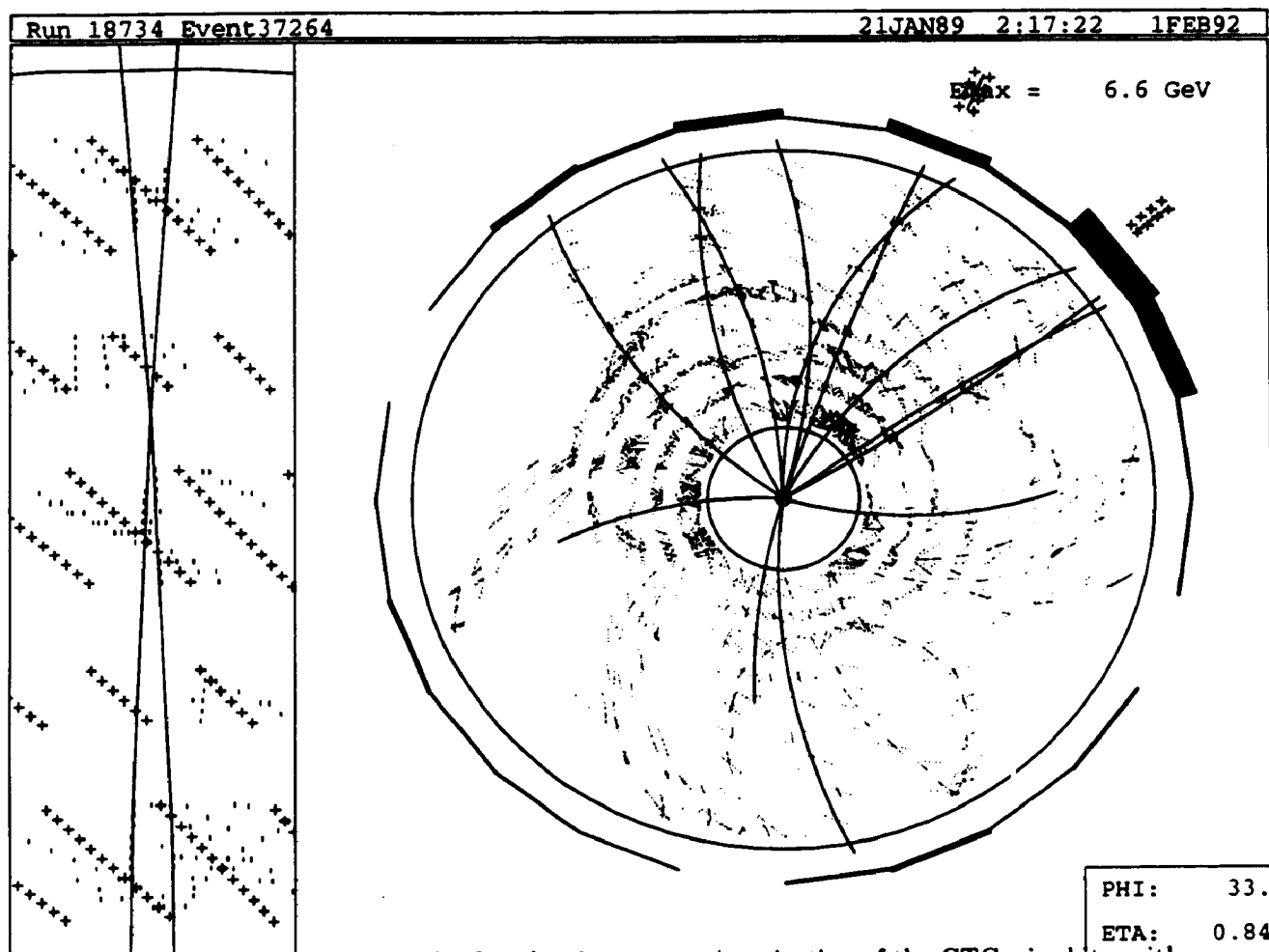


Figure 4.2: An event display showing an  $r - \phi$  projection of the CTC wire hits, with reconstructed tracks overlayed. On the left is a close-up which shows the cell geometry in Superlayers 8,7,6,5, and 4 from the top through the bottom, respectively.

#### 4.4 The Solenoidal Coil

The determination of momentum inside the CTC is made possible by a magnetic field generated by a superconducting solenoidal coil. This coil is located outside the CTC at a radius of 1.5 m, and has a length of 5 m. The coil is made of aluminum-stabilized NbTi/Cu superconductor, and the current during the 1988-89 run was 4650 A. It produces an axial magnetic field of 1.4116 T [33] which points along the  $-z$  direction. The field was mapped with a Hall probe (with a current value of 5000 A, however), and it is estimated that the percentage error in the axial value of the field is  $\sqrt{(0.05)^2 + \frac{(0.21)^2}{N}}$ , where  $N$  is the number of events in the sample under consideration. The dominant contribution to this error comes from the fact that the field was mapped at 5000A but was run at 4650A.

#### 4.5 Central Calorimetry

The calorimetry does not play a major role in this analysis. However, muons must traverse the calorimetry on their way to the muon chambers, and will undergo multiple coulomb scattering along the way. This will effect the offline identification of muons, and so a brief description of the calorimeter parameters is warranted.

The Central Electromagnetic Calorimeter (CEM) [34] lies outside the solenoidal coil. The CEM is composed of 48 wedges, grouped into 2 cylinders of 24 wedges each. The cylinders are placed end-to-end along the  $z$  axis and centered on the nominal

collision point  $z = 0$ . Each wedge is composed of 10 projective towers pointing back to the nominal collision point. This leads to a segmentation in  $\phi$  and  $\eta$  of  $\Delta\eta \times \Delta\phi = 0.09 \times 15^\circ$ . The CEM covers the pseudorapidity region of  $-1.1 \leq \eta \leq 1.1$  and extends from a radius of 160 to 200 cm. It is composed of 31 layers of lead absorber (0.32 cm thick) interspersed with polystyrene scintillator (0.50 cm thick), a total of 18 radiation lengths deep. The resolution in energy is  $\sigma(E)/E = 0.13/\sqrt{E}$ . Wire proportional chambers located 6 radiation lengths deep provide position resolution of  $\sigma_x = 2$  mm,  $\sigma_y = 5$  mm.

The Central Hadronic Calorimeter (CHA) [35] lies outside the CEM. The CHA is arranged in the same wedge-tower scheme as the CEM, and is also segmented such that  $\Delta\eta \times \Delta\phi = 0.09 \times 15^\circ$ . It covers the pseudorapidity region of  $-0.9 \leq \eta \leq 0.9$  and extends from a radius of 200 to 340 cm. It is composed of 32 layers of iron absorber (2.50 cm thick) interspersed with acrylic scintillator (1.00 cm thick), a total of 5 interaction lengths deep. The resolution in energy is  $\sigma(E)/E = 0.70/\sqrt{E}$ .

#### 4.6 The Central Muon Detector (CMU)

The central muon detector [36] consists of 48 chambers, each of which sits behind the hadron part of a central calorimeter wedge. Each chamber covers approximately 12.6 degrees in  $\phi$ , with a gap of 1.2 degrees on both sides of the wedge. The innermost layer of the detector lies at a radius of 347 cm from the nominal beam position. Each

chamber is divided in  $\phi$  into 3 modules. Each module is divided into 16 cells arranged in 4 layers. Each cell has one sense wire situated at the middle of the cell, and the cell is operated in limited streamer mode. Within each layer, alternate cells are connected together; in addition, four sense wires from each layer together form a tower. Thus, each module is comprised of two towers, and each wedge has six towers. Within each tower, two alternate sense wires lie along a radial line from the beam. The other two wires are offset from this line by 2 mm in the azimuthal direction. This allows for resolution of the  $\phi$  ambiguity (of a hit relative to a sense wire) by determining which two wires were hit first. A single hit TDC is used for measurements in the azimuthal direction, while dual ADCs measure position along the sense wire via charge division. The muon geometry is detailed in Figure 4.3.

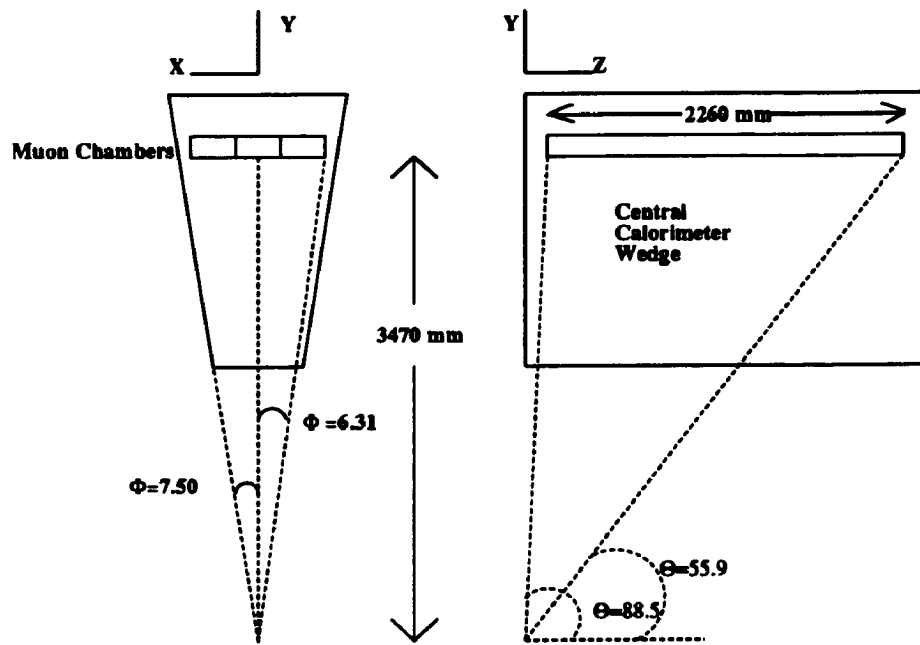


Figure 4.3: The muon chamber (CMU) geometry.

## Chapter 5

### Triggering

#### 5.1 Overview

With an average luminosity of  $1.6 \mu\text{b}^{-1} \text{ sec}^{-1}$  and with an inelastic cross section of  $\sim 44 \text{ mb}$ , the rate for observable events during the 1988-89 run was approximately 70 kHz. Since information for a given event could only be written to tape at a rate of a few Hz, a large fraction of events had to be rejected. At CDF, this is accomplished through a multi-level trigger system [37][38]. This system incorporated a variety of triggers, each sensitive to a different range of possible physics. The analysis of this thesis is based on a trigger sensitive to events with two muons present. This trigger was labeled `Dimuon_Central_3`. Although the total amount of data collected during the 1988-89 collider run was  $4.7 \text{ pb}^{-1}$ , the `Dimuon_Central_3` trigger was in place only during the latter half of the run, during which  $2.6 \text{ pb}^{-1}$  of data was collected.

The first level (Level 1) decision [39] is based in our case on the presence of a single muon candidate (or Level-1 muon stub) in the CMU, and the time for the



decision was less than the  $3.3\mu\text{sec}$  between  $p\bar{p}$  collisions. The rate of events passed by the Level-1 trigger was a few kHz ( $\sim 500\text{Hz}$  for the Level-1 muon trigger alone). Events passing Level 1 were then sent to Level 2, which was designed to reduce the event rate to 1-100 Hz. The rate out of the Level-2 trigger for this analysis was 0.07 Hz, low enough that further reduction in the Level-3 system was unnecessary.

## 5.2 Level 1

The arrangement of the wires in a muon cell naturally lends itself to a trigger [39]. Note that the measurement of the azimuthal positions of the hits in a cell determines the angle  $\alpha$  that a charged track makes with a radial line. In the absence of multiple scattering, this angle  $\alpha$  can be easily related to the transverse momentum of the charged track. This is illustrated in Figure 5.1.

The relationship of the angle of deflection  $\beta$  and transverse momentum  $P_T$  is given by:

$$\sin \frac{\beta}{2} = \frac{eLB}{2P_T}$$

where  $e$  is the charge of the track,  $L = 1.44$  m is the radius of the solenoidal magnetic field, and  $B = 1.4116$  T is the value of the magnetic field. The relationship of the angle  $\beta$  to the angle  $\alpha$  is given by:

$$D \sin \alpha = L \sin \frac{\beta}{2}$$

where  $D = 3.470$  m is the radius out to the muon chambers. In the small angle

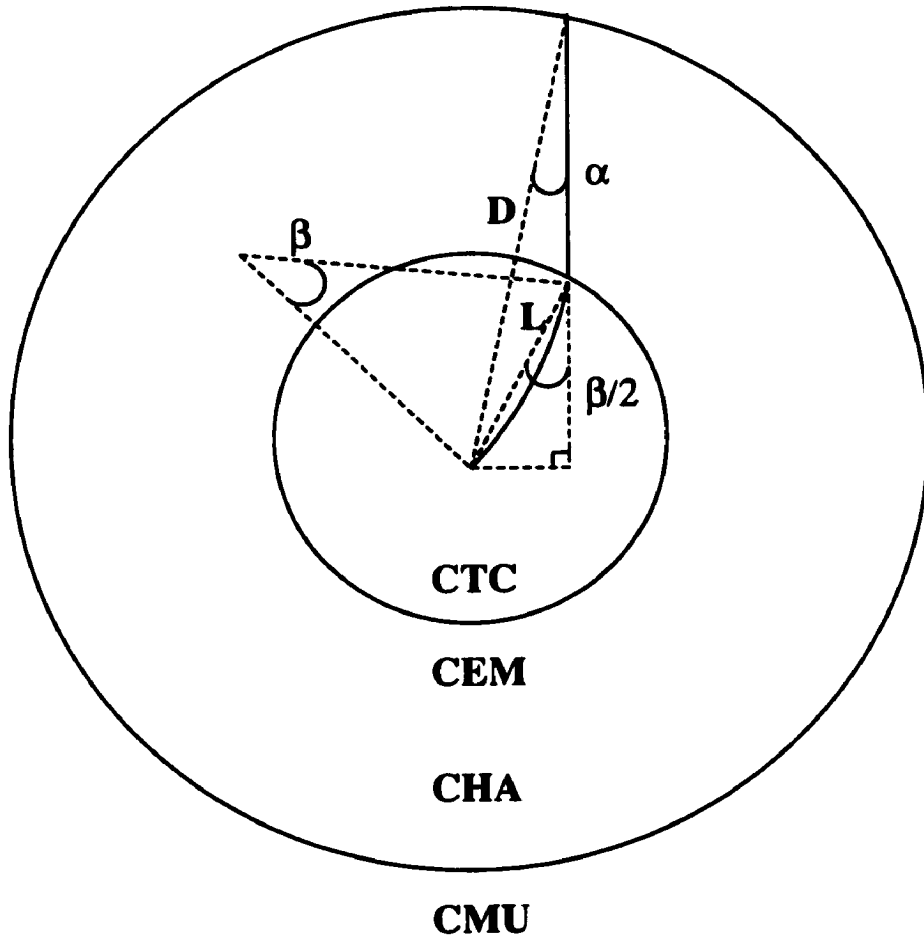


Figure 5.1: Relating an angle measurement in the CMU to the  $P_T$  measurement in the CTC.

approximation for  $\alpha$ , we find:

$$\alpha \approx \frac{eL^2B}{2DP_t}.$$

In the presence of multiple scattering,  $\alpha$  instead is approximated by a Gaussian distribution whose mean is given by the above equation and whose width is given by:

$$\sigma_\alpha = \frac{13.6MeV}{\beta cp} \sqrt{x/X_0}(1.0 + 0.2 \ln x/X_0)$$

where  $\beta c$  is the velocity, and  $p$  is the momentum of the charged track.  $x/X_0$  is the thickness of the calorimeter in radiation lengths.

In the muon chambers,  $\alpha$  is measured by taking the difference in drift times,  $\Delta t$ , in alternate layers:

$$\alpha = v\Delta t/H$$

where  $H = 55$  mm is the radial difference between two sense wires and  $v = 50 \mu\text{m}/\text{nsec}$  is the drift velocity of ionization electrons in the argon/ethane gas in the chambers. Note that each tower provides two independent measures of  $\alpha$ , given by the differences  $\Delta t = t_4 - t_2$  and  $\Delta t = t_3 - t_1$ , where the time subscripts refer to the layer that the drift time is measured in. The Level-1 trigger decision is based on whether the minimum of the two time differences is less than a value preset in the muon Level-1 trigger card. For the Dimuon\_Central\_3 trigger,  $\Delta t = 70$  nsec. Using the above equations, this corresponds to a cut on transverse momentum of  $2.0 \text{ GeV}/c$ . In the presence of multiple scattering, the  $P_T$  cut is only 50% efficient at  $2.0 \text{ GeV}/c$ .

### 5.2.1 Data sample used to Measure the Efficiency

We required triggers at Levels 1, 2, and 3 that were independent of the Central Muon system. This guarantees that we have a sample that is not biased for Central Muon trigger studies. We selected any event which had at least one reconstructed muon.

This selection procedure actually gives us a sample of *candidate* muons. These *candidate* muons (more will be said on this process of offline reconstruction of muons later) are charged tracks in the CTC which have been associated with charged tracks in the CMU. These candidates could in fact be real muons, but in general could also be due to non-interacting or interacting punch-through, or decays in flight of kaons and pions. Non-interacting punch-through describes a charged kaon or pion which traverses the CEM and CHA calorimetry without interacting. For the purposes of studying the trigger, non-interacting punch-through is indistinguishable from a real muon, and should not cause bias. Interacting punch-through, such as might happen with a high-energy jet that leaks out the end of the hadron calorimeter, will bias a trigger study, since the track which enters the CMU chambers cannot be simply related to a CTC track (and more importantly the  $P_T$  of a CTC track).

### 5.2.2 Trigger Efficiency of *Real* Muons

To get an idea of the Level-1 trigger efficiency for high  $P_T$  muons, one can look at a cosmic ray muon sample[40]. This result is shown in Figure 5.2. Note the lack of

statistics below  $5.0 \text{ GeV}/c \ P_T$  . The efficiency for muons with  $P_T \geq 6.0 \text{ GeV}/c$  is  $(93.0 \pm 1.0)\%$ .

The cosmic ray muon sample is nearly background free, so we can use this sample to help us define what a *real* muon sample looks like in the detector. We plan to use this sample to study the muon trigger, so we have to choose variables which do not bias our study. In Figure 5.3 we show the hadronic energy distribution (HAD) for the cosmic ray muon sample. This distribution shows a peak in the HAD region of  $0.6$  to  $3.1 \text{ GeV}/c^2$  , which is consistent with that expected for a minimum ionizing particle (MIP). We will use this HAD variable to distinguish between real muons and background (for the purposes of efficiency studies only, not to form our final data sample).

### 5.2.3 Trigger Efficiency of Interacting Punchthrough

We define our sample of interacting punchthrough as those candidate muons with large hadronic energy (HAD) in the calorimeter tower the muon traversed. In Figure 5.4 we show the trigger efficiency for muons with  $HAD \geq 5.0 \text{ GeV}/c^2$  . The efficiency for muons with  $P_T \geq 6.0 \text{ GeV}/c$  is  $(55.0 \pm 3.0)\%$ . This efficiency is much lower than that seen in the cosmic ray sample.

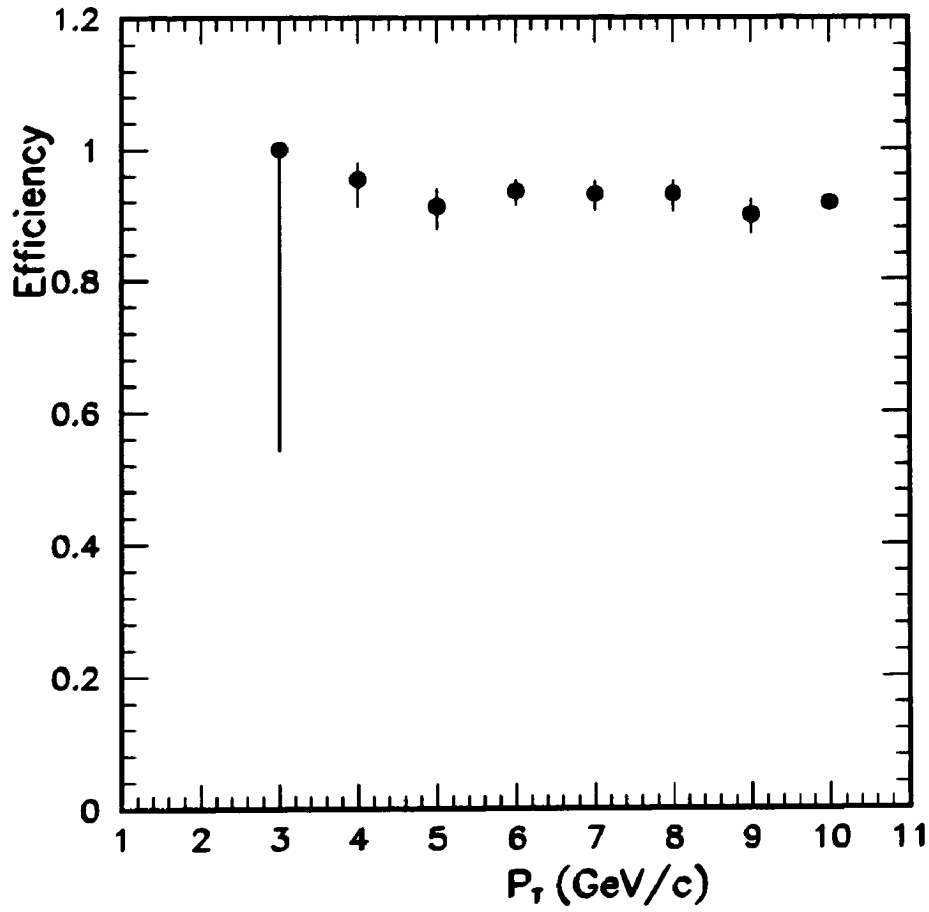


Figure 5.2: Level-1 trigger efficiency using the Cosmic ray sample. The error bars represent the binomial error associated with taking the ratio of two numbers.

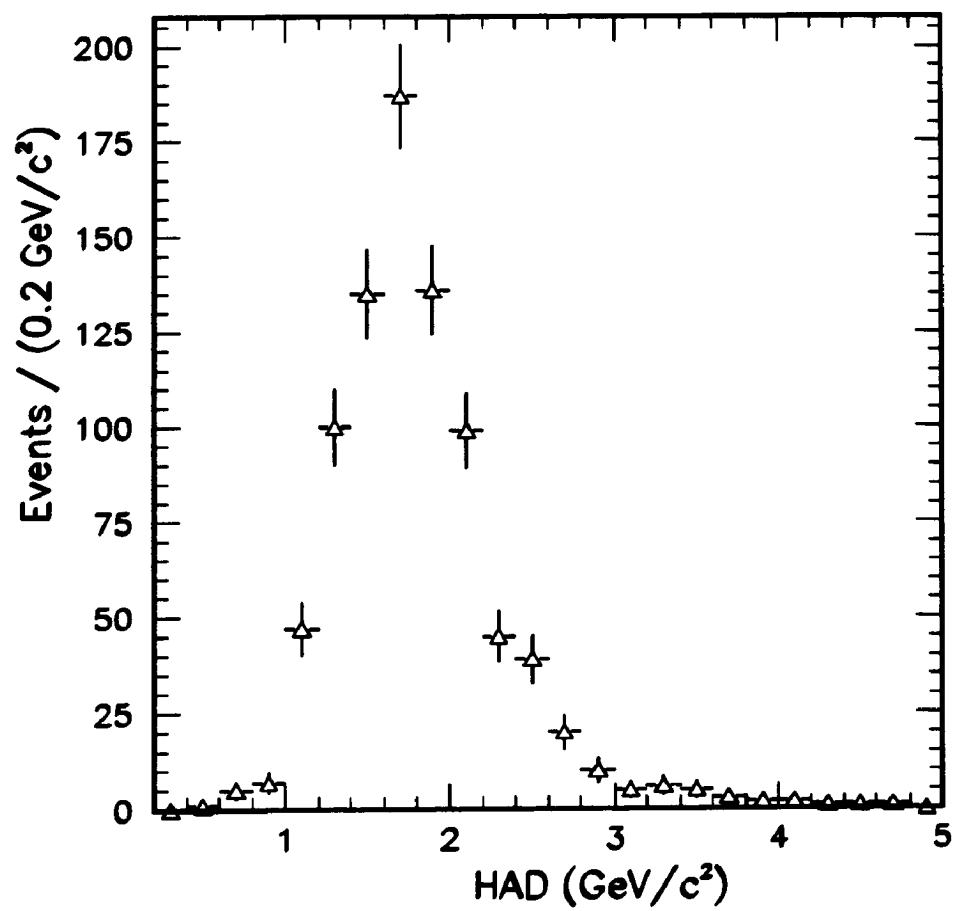


Figure 5.3: Hadronic energy distribution for cosmic ray muon sample. The error bars are statistical.

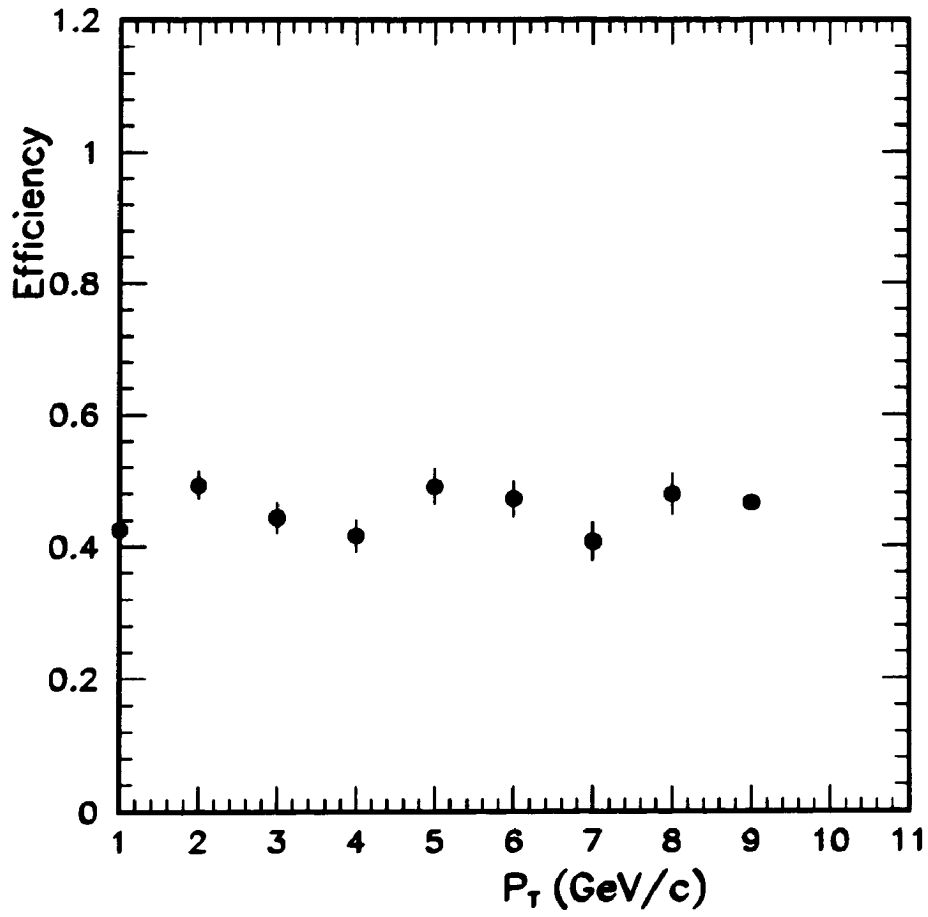


Figure 5.4: Trigger efficiency of background events. The error bars are binomial.



### 5.2.4 Trigger Efficiency of Decays-in-Flight

To test the efficiency of muons from decays in flight of pions and kaons, we used a Monte Carlo model. This model examined the effect on the trigger efficiency for kaons which decayed within the outer radius of the CTC. The model incorporated the kinematics of the kaon decay, and the effects of multiple scattering in the muon chambers, but no effects of track reconstruction are included. In Figure 5.5 we show the efficiency for muons from kaon decay relative to the efficiency of primary muons. The  $P_T$  axis in this figure refers to the kaon  $P_T$ . We see that the efficiency of decay muons is much lower than that of primary muons. The lower efficiency is due to decays in which the angle between the kaon and the decay muon is very large. A similar study of pion decays shows almost no difference in relative efficiency; since the mass difference ( $\pi^\pm - \mu^\pm$ ) is much smaller than ( $K^\pm - \mu^\pm$ ), the muon will tend to follow the parent pion direction. This implies that if muons from kaon decays form a large part of our signal sample, we will underestimate the efficiency of true muons.

### 5.2.5 Method

We divide our sample of candidate muons into two groups: minimum ionizing particles or MIPs (real muons and non-interacting punch-through) and background (interacting punch through). As mentioned previously, we distinguish between the two sources by looking at the energy deposition in the hadronic tower the muon traverses on its

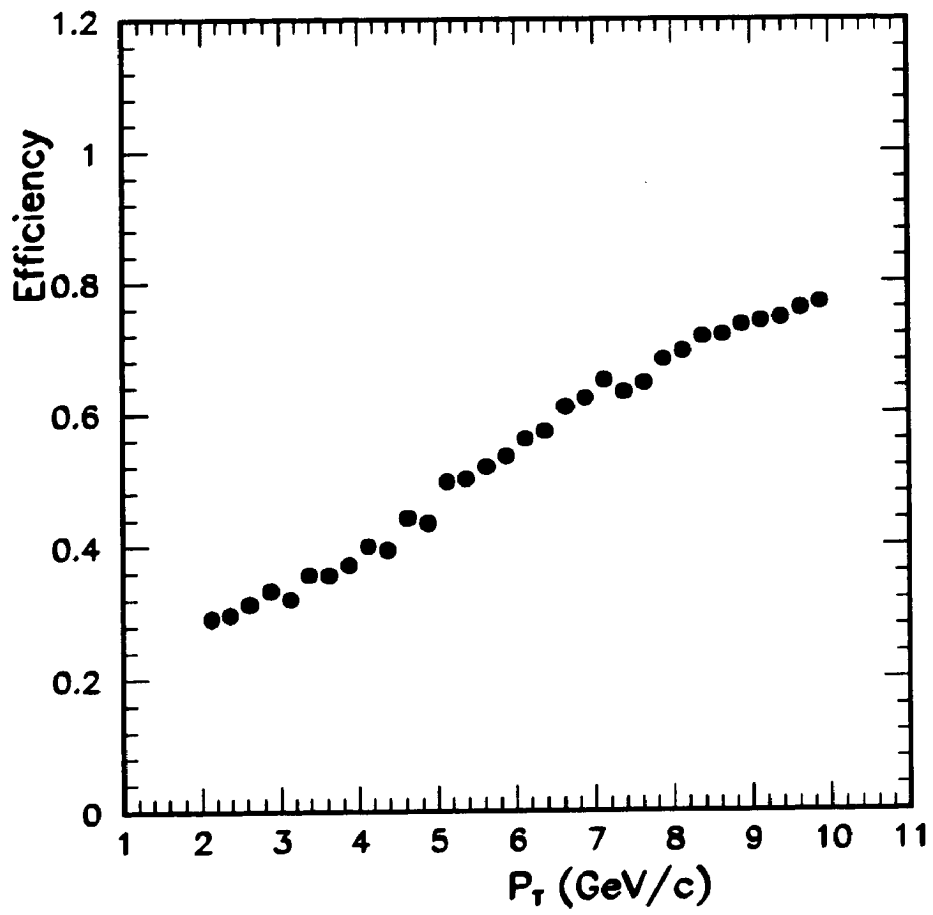


Figure 5.5: Efficiency for muons from kaon decay, relative to primary muons.

way to the muon chambers. This distribution for the full sample of candidate muons is shown in Figure 5.6. The minimum ionizing signal shows clearly, while in addition there is an approximately flat background.

We now need to determine the number of MIPs in our sample. To do this we need to know the functional form of both the MIPs and the background. The functional form for the energy loss due to radiation is given by a Vavilov distribution [41] [42]. This is the general form which in the case of thin absorbers reduces to the Landau distribution. The results of using this form on the cosmic ray muon sample is shown in Figure 5.7. We will define our signal region as the interval in hadronic energy  $0.6 - 3.1 \text{ GeV}/c^2$ .

To determine the form for the background we first assume that the background is due to cases in which there is no real relationship between the CTC track and the CMU track. We can then examine the HAD distribution for candidate muons which exhibit a large mismatch between the CTC track and the CMU track. Since the trigger is dependent on the  $xy$  matching, we examine matching in the  $zy$  plane. To characterize the background we demand a mismatch in the  $zy$  plane which is 5 times larger than the expected error on the mismatch. This cut will be described in more detail in Chapter 6. The HAD distribution with this cut is shown in Figure 5.8, where we have divided the background sample into the  $P_T$  intervals  $(3 - 5)\text{GeV}/c$ ,  $(5 - 7)\text{GeV}/c$ ,  $(7 - 9)\text{GeV}/c$  and  $(9 - 11)\text{GeV}/c$ . We will approximate the background

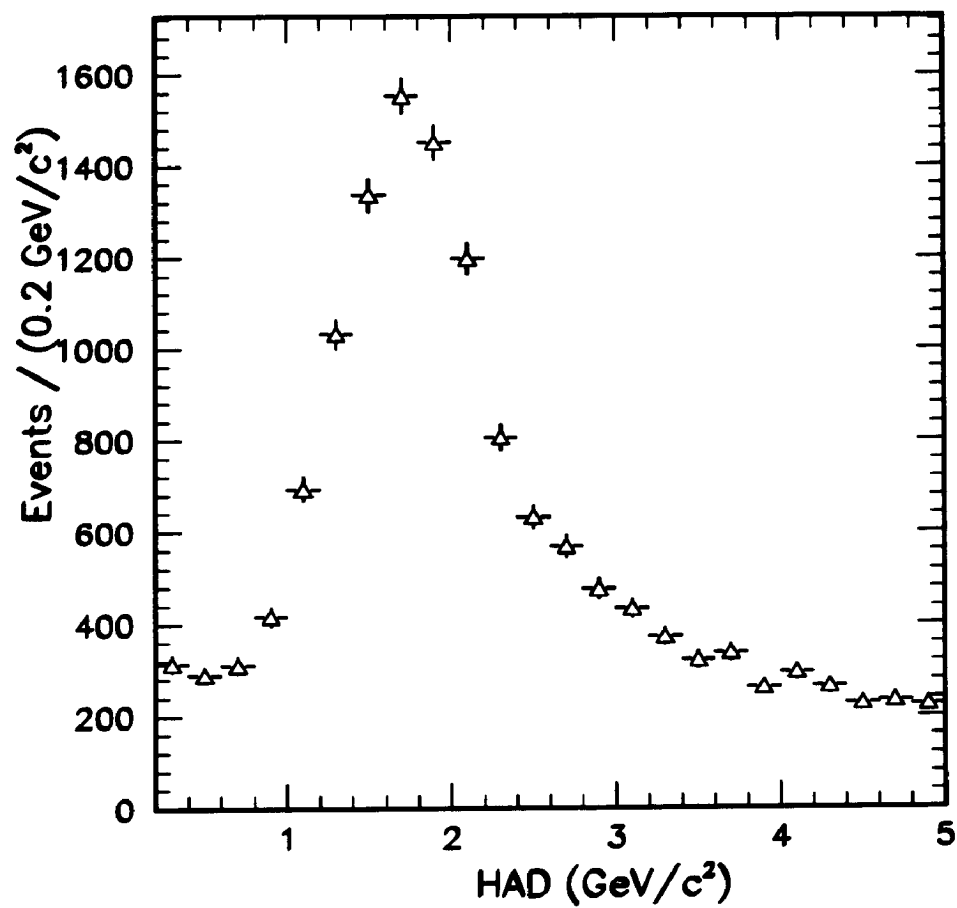


Figure 5.6: Hadronic energy distribution for the candidate muon sample. The error bars are statistical.

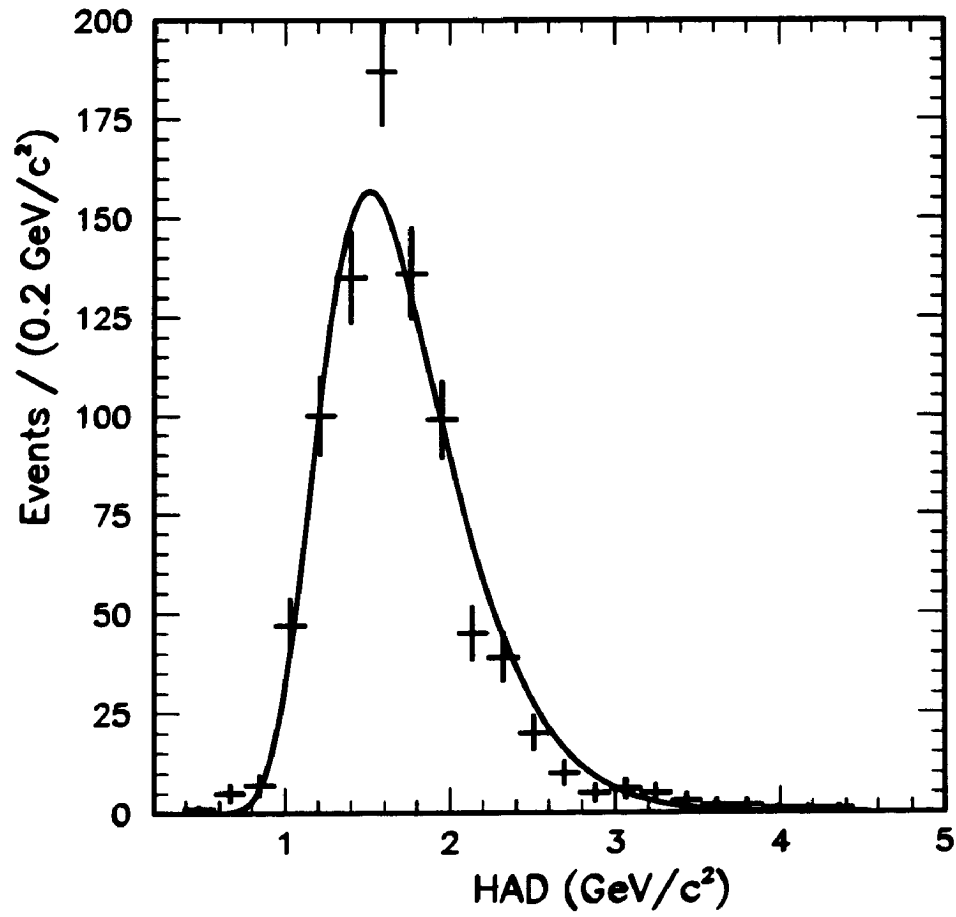


Figure 5.7: Fitting the hadronic energy distribution. The error bars are statistical.

distribution with a straight line.

Given the above fitting procedure, our methodology for determining the level-1 trigger efficiency as a function of  $P_T$  is as follows:

- We divide the sample of events lying in the signal region into bins in  $P_T$ .
- For each  $P_T$  bin, we fit the HAD distribution and determine the number of MIPs,  $N_{s1}$ , in the signal region.
- Then we require that the muon candidate fired the Level-1 trigger, refit the HAD distribution and determine the number of MIPs  $N_{s2}$  in the signal region.
- The efficiency at the given  $P_T$  bin is then:

$$\epsilon = \frac{N_{s2}}{N_{s1}}$$

Since we determine the efficiency by taking the ratio of the results of the two fits, we should be fairly insensitive to the assumed shape of the background. In Figures 5.9 and 5.10 we show the fits for the  $P_T$  bins (2.0 – 2.5) GeV/c , (2.5 – 3.0) GeV/c , (3.0 – 3.5) GeV/c , (3.5 – 4.0) GeV/c , (4.0 – 5.0) GeV/c , (5.0 – 6.0) GeV/c , (6.0 – 7.0) GeV/c , and (7.0 – 8.0) GeV/c , respectively. In Figures 5.11 and 5.12 we show the fits in the same bins, for the data passing the trigger. Finally, in Figure 5.13 we show the efficiency as a function of  $P_T$ . For each value  $\epsilon$ , the error is determined by taking in quadrature the error on the numbers  $N_{s1}$  and  $N_{s2}$  which are taken from

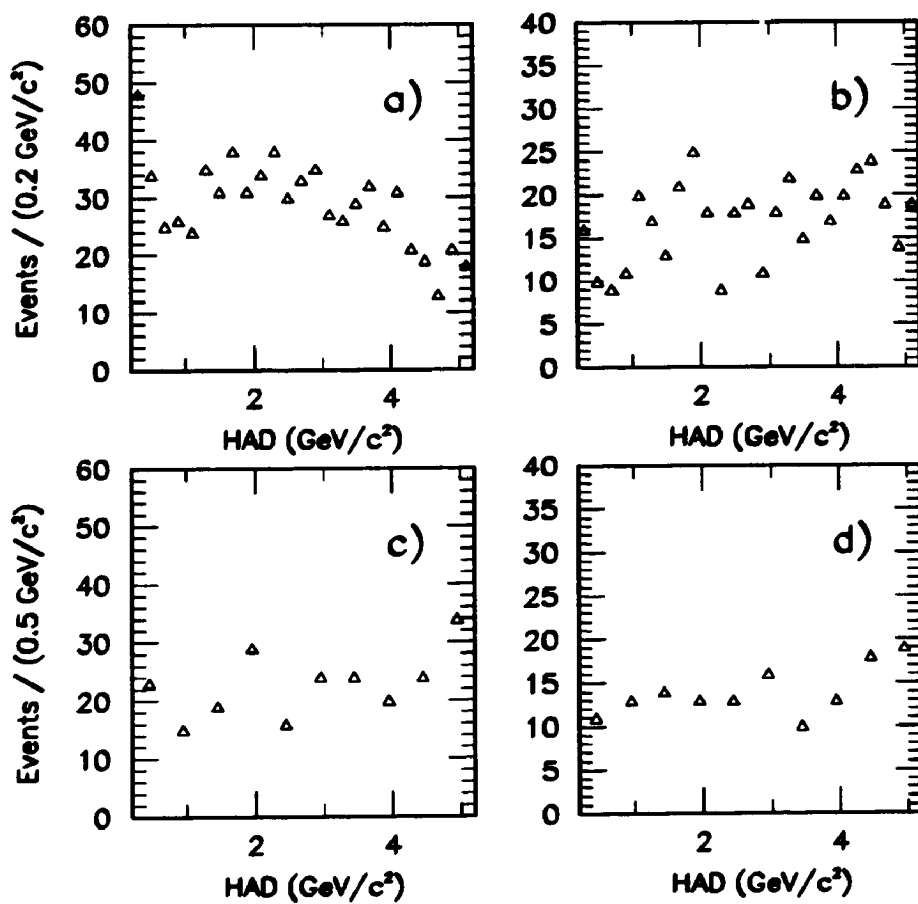


Figure 5.8: Shape of the hadronic energy distribution for background.

the fits. The error determined in this way is in general larger than the binomial error associated with taking the ratio of two numbers, and so is seen as conservative. The error is also constrained to lie in the physical region (i.e. the efficiency should always lie between 0.0 and 1.0) using a method detailed in the Particle Data Book[2].

### 5.2.6 Parameterization of the Efficiency

In order to parameterize the Level-1 efficiency we use a form motivated by the multiple scattering. Remember that the Level-1 trigger cuts on the angle that a track in the muon chambers makes with a radial line. Previously, we saw that in the presence of multiple scattering, the angle a track makes in the muon chambers is described by a Gaussian with mean:

$$\alpha_0 = \frac{0.140}{P_T(\text{GeV}/c)}$$

and sigma:

$$\sigma_\alpha = \frac{0.085}{P_T(\text{GeV}/c)}.$$

The nominal  $P_T$  cutoff for the Level 1 trigger was  $2.0 \text{ GeV}/c$ , which corresponds to a cut on the angle of:

$$\alpha_c = \frac{0.140}{2.0(\text{GeV}/c)} = 0.070 \text{ radians}.$$

Since the trigger actually cuts on angle, the Gaussian smearing implies that the trigger is not fully efficient until a much higher  $P_T$ . This is illustrated in Figure 5.14, where we show the Gaussian-distributed angles for several  $P_T$  's. The two straight lines in



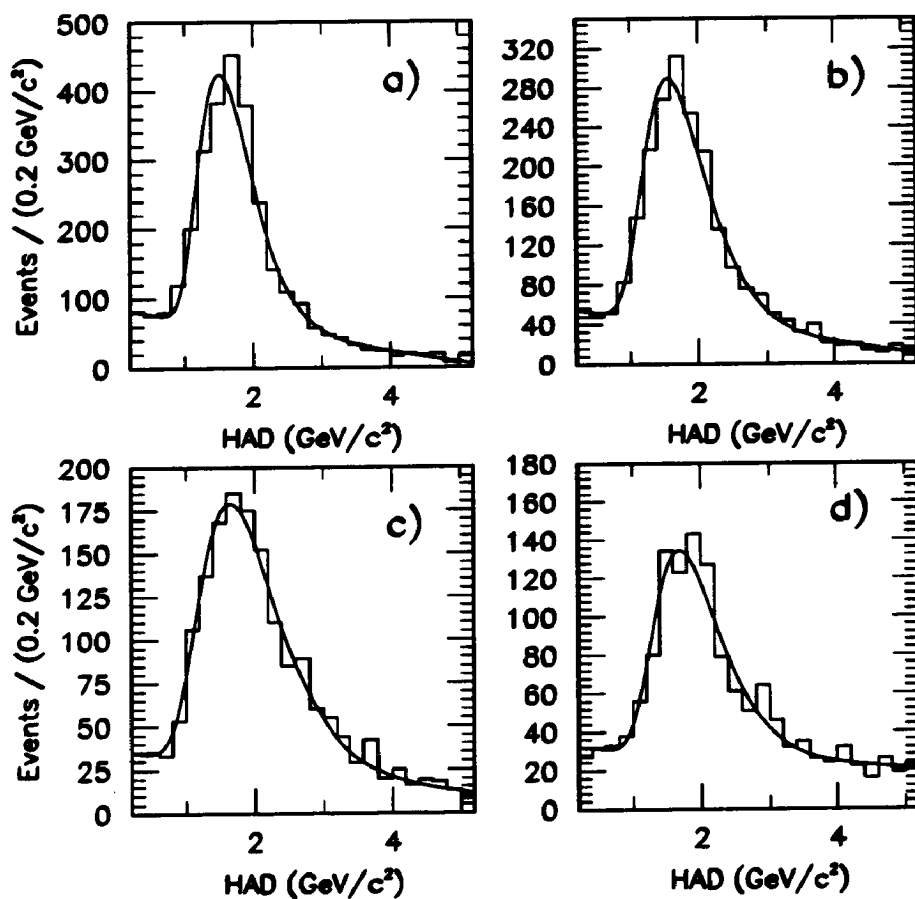


Figure 5.9: Fitting the HAD distribution for data with no trigger requirement. The data is organized into the following bins of  $P_T$  : (a)  $P_T$  range (2.0 – 2.5), (b)  $P_T$  range (2.5 – 3.0), (c)  $P_T$  range (3.0 – 3.5), (d)  $P_T$  range (3.5 – 4.0).

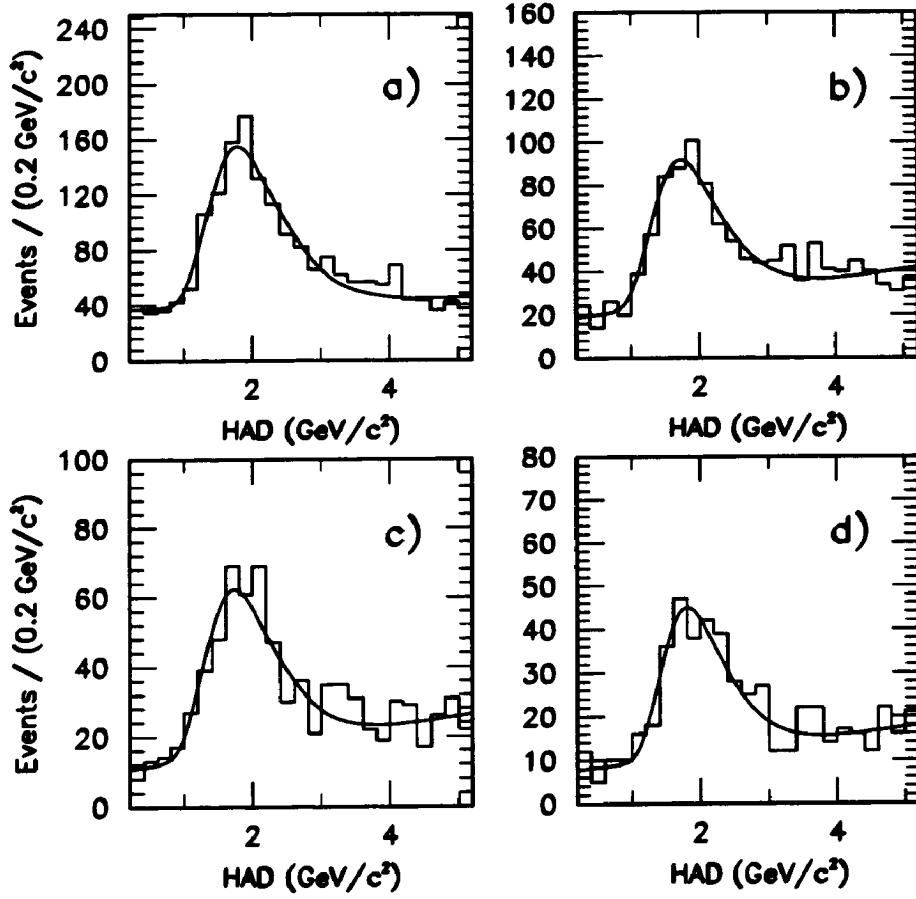


Figure 5.10: Fitting the HAD distribution for data with no trigger requirement. The data is organized into the following bins of  $P_T$  : (a)  $P_T$  range (4.0 – 5.0), (b)  $P_T$  range (5.0 – 6.0), (c)  $P_T$  range (6.0 – 7.0), (d)  $P_T$  range (7.0 – 8.0).

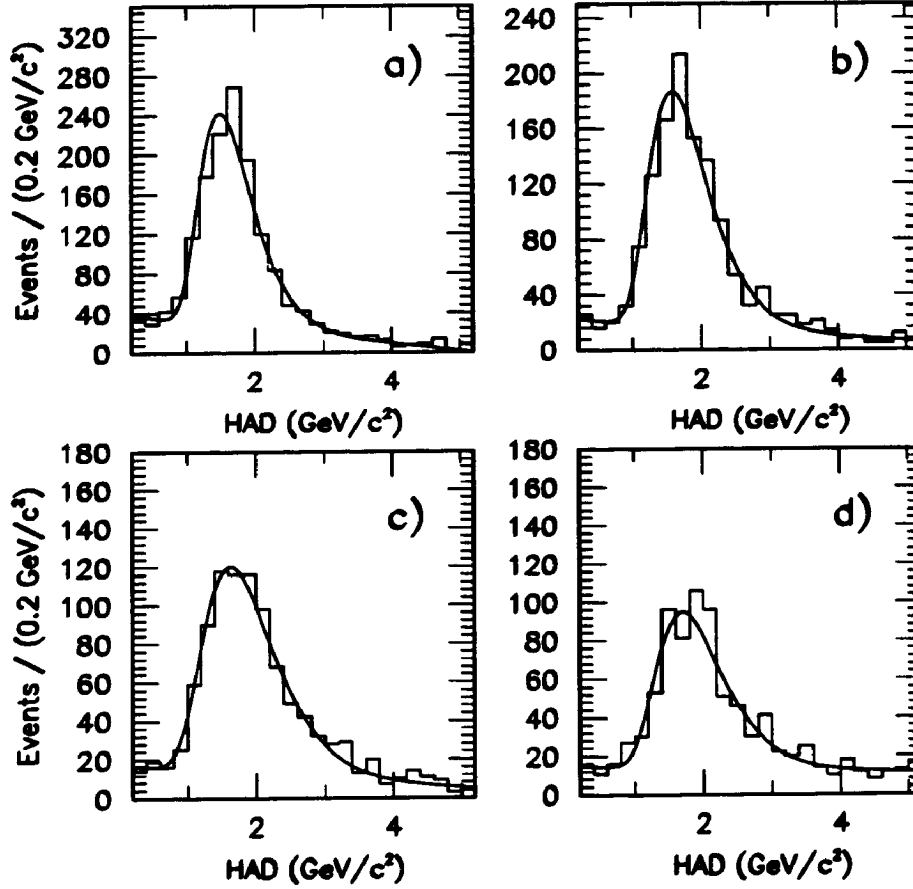


Figure 5.11: Fitting the HAD distribution for data which passed the Level-1 muon trigger.. The data is organized into the following bins of  $P_T$  : (a)  $P_T$  range (2.0 – 2.5), (b)  $P_T$  range (2.5 – 3.0), (c)  $P_T$  range (3.0 – 3.5), (d)  $P_T$  range (3.5 – 4.0).

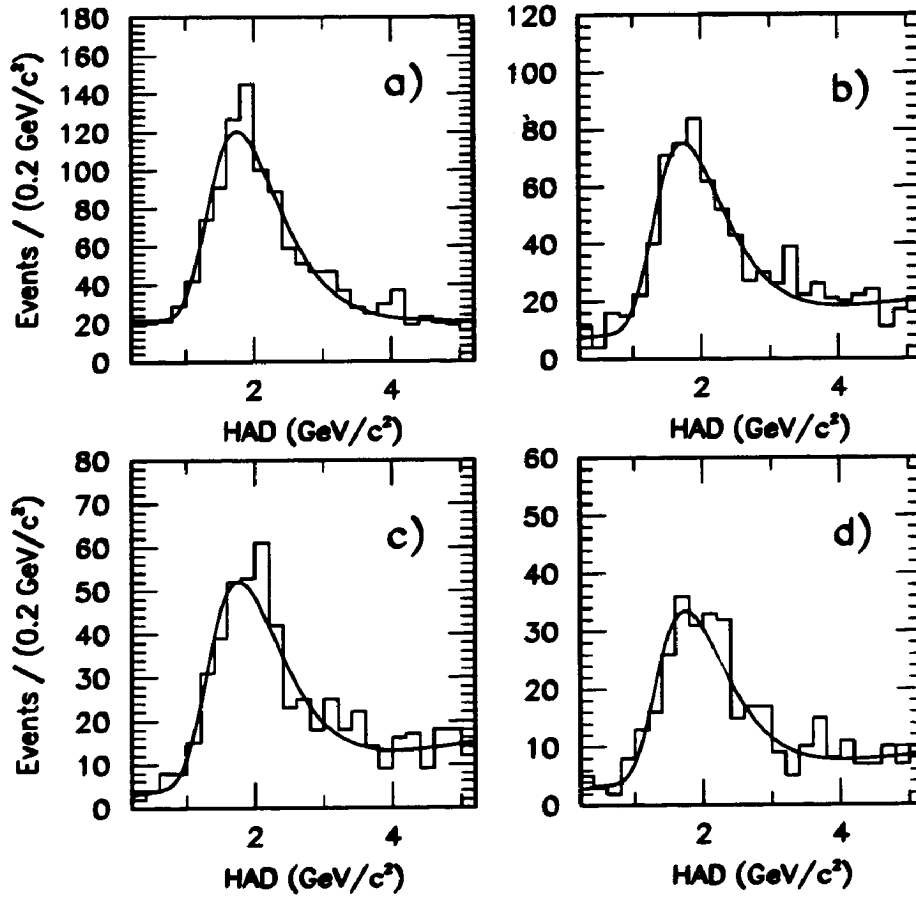


Figure 5.12: Fitting the HAD distribution for data which passed the Level-1 muon trigger.. The data is organized into the following bins of  $P_T$  : (a)  $P_T$  range (4.0 – 5.0), (b)  $P_T$  range (5.0 – 6.0), (c)  $P_T$  range (6.0 – 7.0), (d)  $P_T$  range (7.0 – 8.0).

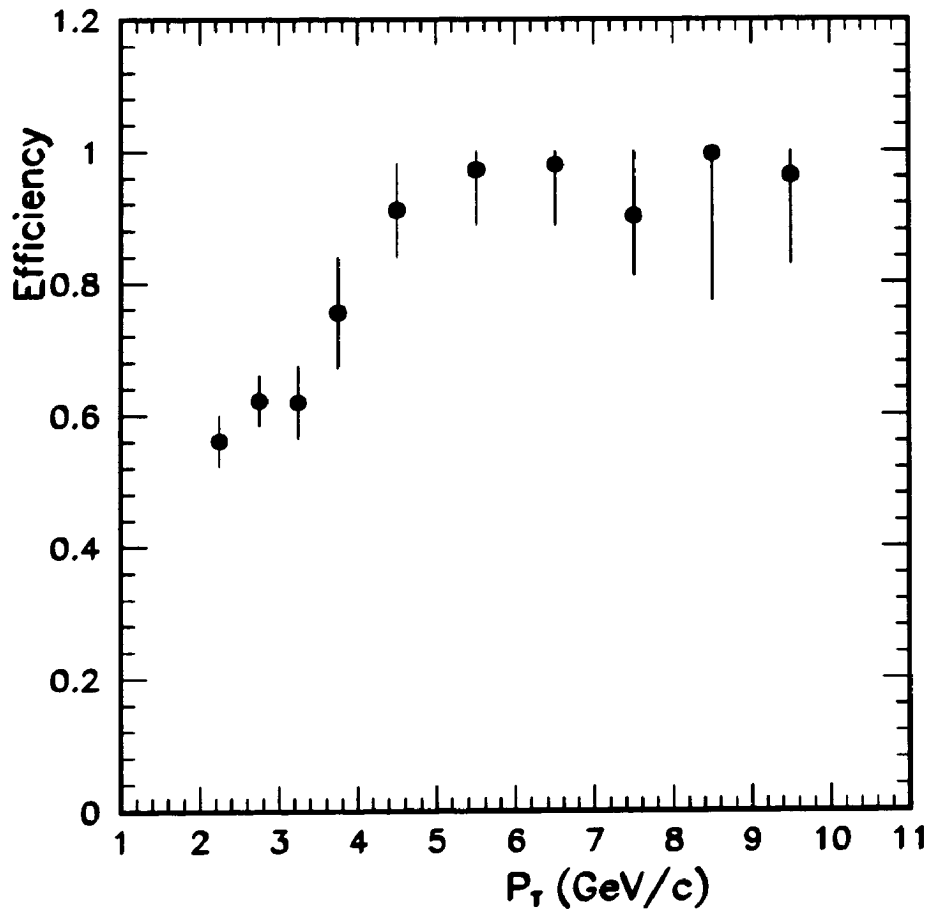


Figure 5.13: Level-1 muon trigger efficiency measurement as a function of muon CTC track  $P_T$ . The error bars are binomial.

this plot correspond to the two angles ( $\pm\alpha_c$ ) that are cut on at Level 1. This figure shows that at the nominal  $P_T$  cutoff of 2.0 GeV/c the trigger is only 50% efficient. The efficiency at a given  $P_T$  can be described as the percentage of the area of the corresponding Gaussian that falls below the cut angle. The efficiency can be written:

$$\epsilon = \frac{A}{\sqrt{2\pi}} \int_{-\alpha_c}^{\alpha_c} \exp \left[ -\frac{(\alpha - \alpha_0)^2}{\sigma_\alpha^2} \right] d\alpha = f(A, \alpha_c, P_T)$$

The  $P_T$  dependence comes in the terms  $\alpha_0$  and  $\sigma_\alpha$ . We allow the overall normalization  $A$  (the efficiency of the trigger at high  $P_T$ ) and the cut angle  $\alpha_c$  to float. To test the fitting function, we fit data from a Monte Carlo simulation of the trigger efficiency. The results are shown in Figure 5.15, and it is clear that the fitting function is very good. We then fit the data in Figure 5.13, and we get the following values:

$$A = 0.918 \pm 0.024$$

$$\alpha_c = 0.070 \pm 0.004.$$

The value for  $\alpha_c$  corresponds to a  $P_T$  cutoff of  $(2.0 \pm 0.1)$  GeV/c, which agrees well with the expectation of 2.0 GeV/c. The results of the fit are shown in Figure 5.16.

### 5.3 Level 2

The Level-2 muon trigger uses information from both the Level-1 CMU system and the Central Fast Tracker[43] (CFT). The CFT is the hardware track finder for the

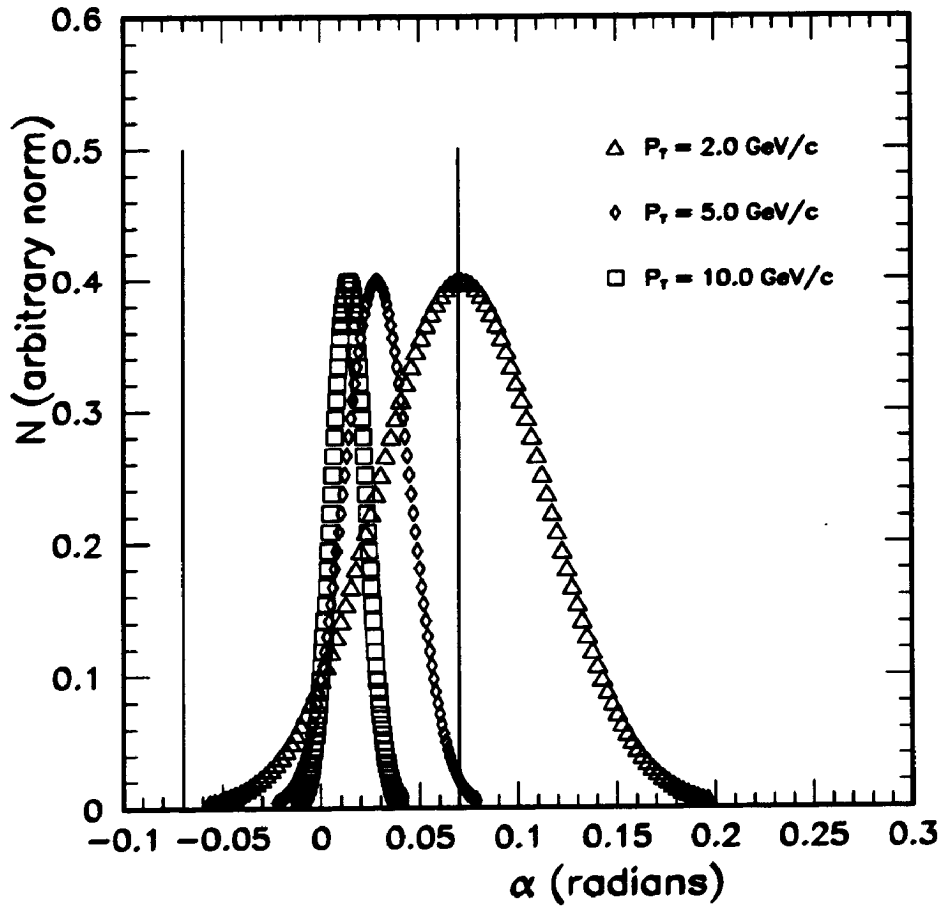


Figure 5.14: Effect of gaussian smearing on muon chamber angle, as a function of track  $P_T$ . The two solid straight lines indicate the region in angle  $\alpha$  accepted by the Level-1 trigger.

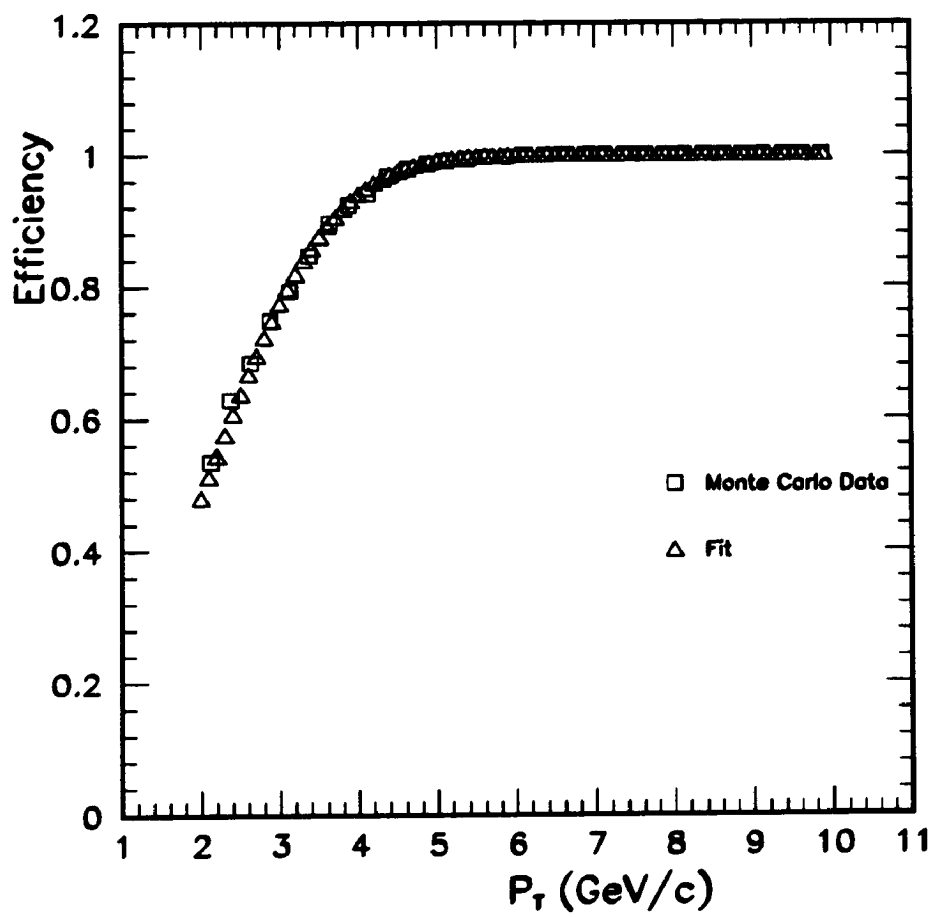


Figure 5.15: Fitting function test on Monte Carlo data sample.



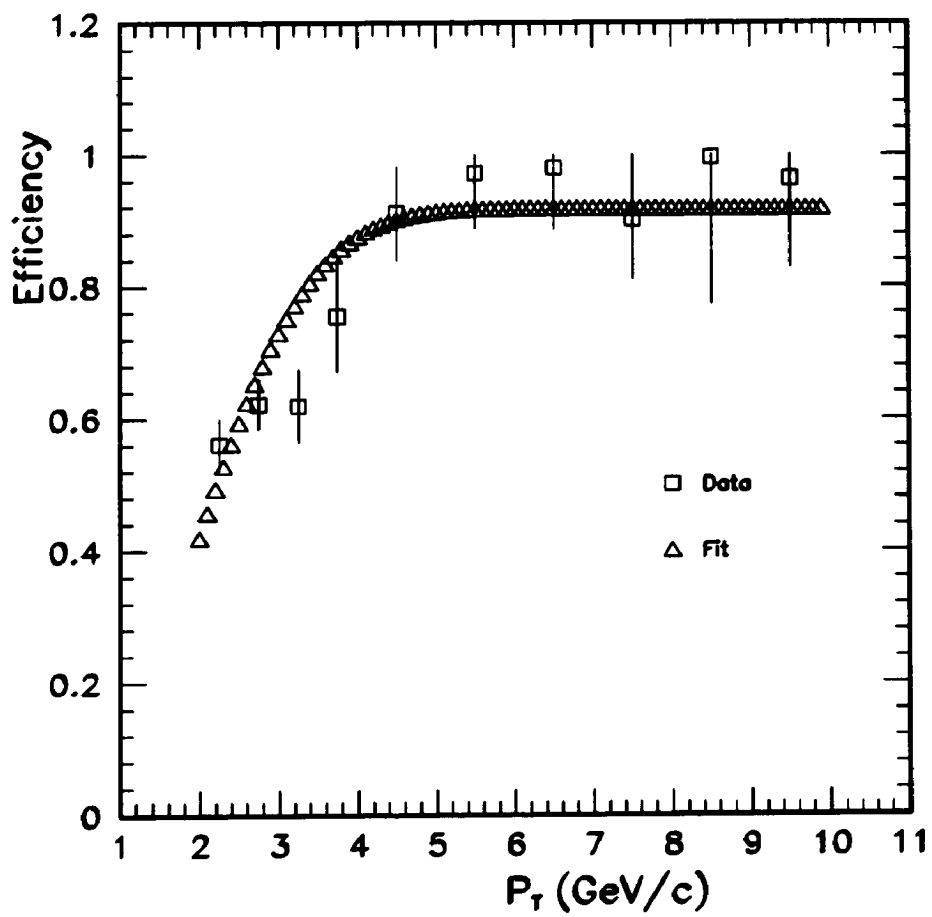


Figure 5.16: Fit of the Level-1 muon trigger efficiency. The error bars are binomial.

CTC. When the CFT has finished processing, it sends its list of found tracks to the Muon Matchbox. The Muon Matchbox uses lookup tables to associate CFT tracks with Level-1 muon stubs. The lookup tables incorporate both curvature and multiple scattering information. Level-1 muons which match CFT tracks are labeled golden muons, and a bit is set in an  $\eta$  and  $\phi$  map. This map is a  $2 \times 24$  array, corresponding to the 2 sides in  $\eta$  and the 24 wedges in  $\phi$ . At this step, the map of golden muons is processed by the Cluster Finder. The Cluster Finder merges golden muons which are nearest neighbors in either  $\eta$  or  $\phi$  into muon clusters. Diagonal neighbors are excluded in this merging process. The Dimuon\_Central\_3 trigger required two muon clusters.

The requirements of the Level-2 Dimuon\_Central\_3 trigger are:

- 2 Level-1 muon triggers (stubs)
- The  $P_T$  of each muon must be  $\geq 3.0$  GeV/c . This requirement is met by associating a CFT track with each muon stub.
- The two muon candidates cannot be nearest neighbors in either  $\eta$  or  $\phi$ .

Our study of the Level-2 trigger is separated into two pieces. We first test the efficiency for the CFT system to tag candidate muons which have fired the Level-1 trigger. This test will give us an idea of the CFT track finding efficiency as a function of track  $P_T$  . The second test we perform examines the overall efficiency of the Level-2 system. We

look at the efficiency of the CFT to find two muons (each of which have fired the Level-1 trigger) and the subsequent probability for the the Level-2 flag to be set. The data sample we use for these tests is a subset of that used in the Level-1 study. In addition to demanding a non-muon trigger as above, we also demand a trigger that is not based on the CFT system.

### 5.3.1 The Efficiency of the CFT

We look at candidate muons that fired the Level-1 CMU trigger (in this case Central\_Muon\_3). We then ask if the CFT found a track pointing at the wedge of the muon. We associate CFT tracks with CMU wedges using the lookup tables the muon matchbox hardware used. As mentioned previously, these lookup tables incorporate both the sign of the CFT track and multiple scattering in extrapolating the CFT track to the muon chambers. The result of this study is shown in Figure 5.17. The  $P_T$  cutoff below 2.0 GeV/c is due to a cut applied during offline reconstruction. The efficiency for  $P_T \geq 3.0$  GeV/c is  $(99.5^{+0.3}_{-0.6})\%$ , and the 90% efficiency point is approximately at 2.9 GeV/c .

### 5.3.2 The Efficiency of the Level-2 System

We required two candidate muons, each of which corresponded to a level 1 trigger. We require the  $P_T$  of both muons to be greater than 3.0 GeV/c. If the two muons also satisfy the geometry requirement of the Dimuon\_Central\_3 trigger (i.e. are not

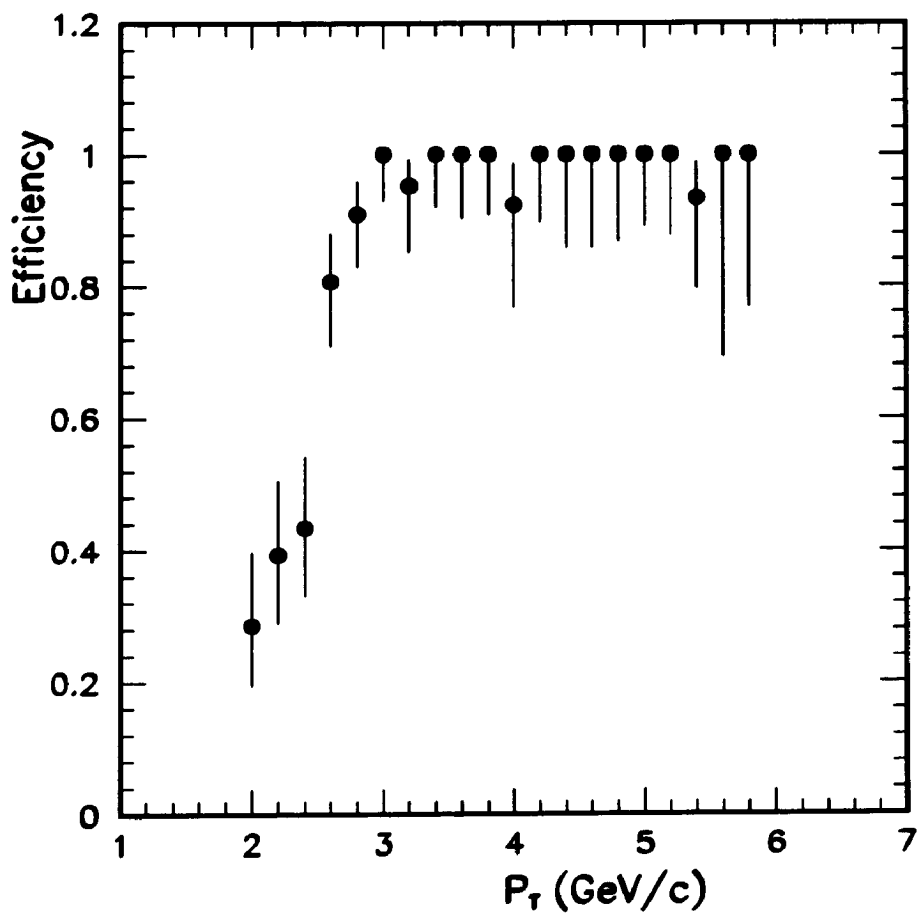


Figure 5.17: Efficiency of the CFT as a function of muon CTC track  $P_T$ . The error bars are binomial.

nearest neighbors in either  $\eta$  or  $\phi$ ), we then check if a CFT track points to each wedge corresponding to the two muons. Another straightforward test is to see if the event passed the Level-2 Dimuon\_Central\_3 trigger. The efficiency that results is the true Level-2 trigger efficiency, given the presence of 2 Level-1 muon stubs. In a sample of 5147 events with two muons (from the above trigger set), we found 133 that satisfied the full requirements of the Level-2 trigger. In 131 of these events, both muons were found by the CFT, and all (131) of these events passed the Level-2 Dimuon\_Central\_3 trigger. This corresponds to an efficiency of  $(98.5^{+1.0}_{-2.0})\%$ .

## Chapter 6

### Offline Reconstruction

The aim of the CDF offline reconstruction package is to locate physics objects that are present in a given event. These objects are typically muon candidates, electron candidates, clusters of energy in the calorimetry (JETs), or simply charged tracks reconstructed in the CTC. We say *candidates* because the given object has properties which are only consistent with the physics process in question.

Typical objects for this analysis are:

- **Muons:** These objects are *defined* as charged tracks reconstructed in the CTC which point to a charged track reconstructed in the CMU. This extrapolation must take into account the return of the magnetic field in the calorimetry (which serves as the flux return for the solenoidal field), and the effects of multiple scattering in the calorimetry.
- **Charged Tracks:** These objects are simply reconstructed CTC tracks which are not necessarily associated with any activity in either the CMU or the calorime-

try. In general, we have no way of knowing whether a given track is an  $e^\pm$ ,  $\mu^\pm$ ,  $K^\pm$ ,  $\pi^\pm$ , etc. In cases where we are looking for charged kaons,  $K^\pm$ , we assume all CTC tracks are kaons. In cases where we are looking for both charged kaons  $K^\pm$  and pions  $\pi^\pm$ , each CTC track must be tried as both a kaon and a pion, and so forth.

The offline reconstruction path for this analysis begins with the reconstruction of the  $z$  vertex, followed by reconstruction of all charged tracks in the CTC, followed by reconstruction of all charged tracks in the CMU, followed by linking CMU tracks with CTC tracks. Finally, a discussion of vertex and mass constraint algorithms follows.

## 6.1 Z Vertex Reconstruction

As mentioned previously, the VTPC is used in the offline analysis in reconstructing the position of the  $z$  vertex. Although the  $p\bar{p}$  beams nominally collide at  $z = 0$ , the length of the proton and anti-proton bunches leads to a distribution in  $z$  vertices which can be described by a Gaussian of width 30 cm centered on  $z = 0$ . The determination of the  $z$  vertex is important for reconstruction of CTC tracks and also in vertex constraints.

The algorithm for finding the  $z$  vertex [44] begins by identifying all hit patterns, or segments, consistent with the passage of a charged track. The segment search is performed within each octant of the VTPC. The requirements for the segments are:

- The number of hits in the segment must be  $\geq 6$
- The occupancy of the segment must be  $\geq 0.7$
- The  $\chi^2$  of the fit of the segment must be  $\leq 1000$

For all segments passing the above cuts, a  $z$  intercept is found. The resulting  $z$  intercepts are grouped into clusters, where a new cluster is defined if there is a separation of greater than 1.5 cm between intercepts. For each cluster, a 1.5 cm wide window is defined which maximizes the number of  $z$ -intercepts within the window. For each window so defined, the mean of the  $z$  intercepts is calculated. Finally, the process is iterated until the mean of all the intercepts is within  $\pm 1$  cm of the previous mean.

The efficiency for this algorithm has been checked by scanning a large number of events by eye. The efficiency for Minimum Bias events (i.e. those recorded with the least amount of trigger bias) was determined to be  $(98.7_{-1.3}^{+0.7})\%$ . In a sample of physics triggered events (i.e. those requiring a lepton in the trigger, or significant energy deposition in the calorimetry) the efficiency was determined to be  $(99.8_{-0.4}^{+0.1})\%$ , where the increase is due to the higher charged-track multiplicity of the events. The  $z$ -vertex position resolution is approximately 2 mm.



## 6.2 Track Reconstruction in the CTC

The path of a charged particle in the solenoidal field of the CTC is a helix. It can be shown that 5 parameters are needed to specify this helix, once a reference surface is chosen. At CDF, the reference surface is chosen as the *distance of closest approach* or impact parameter, of the track to the nominal beam or  $z$  axis. This reference surface is different for every track. For this choice, the 5 track parameters are then:

- $D_0$ , or the distance of closest approach in the  $xy$  plane
- $Z_0$ , or  $Z$  position at the distance of closest approach
- $\phi_0$ , or the direction in the  $x - y$  plane at the distance of closest approach
- $\cot \theta$ , where  $\theta$  is the dip angle of the helix
- $c$ , or the curvature of the track

In terms of the above 5 parameters, the path of a charged track can be expressed through the following equations:

$$x = r \sin \phi - (r + D_0) \sin \phi_0$$

$$y = -r \cos \phi + (r + D_0) \cos \phi_0$$

$$z = z_0 + s \cot \theta$$

$$r = \frac{1}{2c}$$

$$s = r(\phi - \phi_0)$$

In the above equations,  $s$  refers to the path length along the track, and  $r$  is the radius of the helix. Note that the helical model for the track path depends on the assumption of a uniform magnetic field, and the absence of matter (or minimal multiple scattering) within the tracking volume. In addition, the extrapolation of the track parameters to the distance of closest approach assumes the absence of matter between the CTC and the point of origin of the track.

What is actually measured in the CTC is the track path or the curvature  $c$  and the  $\cot \theta$ . In order to relate these quantities to the momentum of the track, one needs the following relations:

$$P_T = \frac{0.00149896B}{|c|} (\text{in GeV}/c)$$

$$B = 14116 \text{ Gauss}$$

$$P_x = P_T \cos \phi_0$$

$$P_y = P_T \sin \phi_0$$

$$P_z = P_T \cot \theta$$

where  $P_x$  and  $P_y$  have been evaluated (as is customary) at the distance of closest approach.

### 6.2.1 Algorithm

There were two algorithms [45] used to perform CTC track reconstruction for the 1988-89 data set.

- Algorithm A

- First identify line segments in the axial layers. A segment is defined as a subset of the 12 hits possible in a axial layer which are consistent with a track.
- Search in adjacent axial layers (moving from the outer to the inner layers) for segments which are consistent with the seed segment. The slope of the segments in the two layers should be consistent with a circle (i.e., the path of a charged particle in a magnetic field).
- Continue the search for segments in the remaining layers.
- Finally, perform a circle fit to all the hits for all axial segments linked together. This part of the fit yields the track parameters  $\phi_0, c, D_0$ .
- The remaining parameters  $z_0$  and  $\cot \theta$  are found by examining the stereo wires. Given the axial fit and the radius of the stereo layers, one can predict the  $\phi$  region in which to search for stereo hits. The stereo hits then supply  $z$  values (as a function of the radius and  $\phi$ ).

- Algorithm B

- First identify line segments in the outer axial layers.
- Given the slope of the hits in the outer layer, and the position of the beam (i.e. the expected origin of the track), extrapolate the track path through the inner layers.
- Given this path, look for segments in the inner layers.
- Using the closest found segment, repeat the process, but drop the beam constraint.
- Once the track has been extrapolated into the innermost layer, perform the full axial fit.
- Associate stereo hits as for Algorithm A above.

For both algorithms, a final fit must be performed. For all reconstructed tracks which point at the same  $z$  vertex (i.e. which come from the same interaction), the residuals (the differences between the measured and fitted hit positions) are summed and averaged. This resulting number (called the  $T0$ ) is then subtracted from all the hits, and the final fit is performed for all tracks.

Algorithm *B* was first run on the data. The sample of all events containing 2 reconstructed muons was then extracted. Algorithm *A* was then run on this sub-sample of events.

### 6.2.2 Wire Resolution and Efficiency

The measured CTC position resolution and wire efficiency [46] are shown in Figure 6.1. The resolution varied from about 350 microns in the inner CTC layers to about 200 microns in the outer layers. The probability that a CTC wire measurement would be used in the final fit varied from about 50% in the inner layers to about 93% in the outer layers. The lower efficiency and poorer resolution of the inner layers is believed to be due to the higher track density present in these layers.

### 6.2.3 Track Quality Cuts

The following cuts are imposed to improve track quality:

- $\eta \leq 1.5$
- At least 2 axial layers with at least 8 hits each
- At least 2 stereo layers with at least 4 hits each

Tracks which fail the above cuts are in general very poorly reconstructed.

### 6.2.4 Track Reconstruction Efficiency

We measured the CTC track reconstruction efficiency by embedding simulated tracks in real data  $J/\psi$  events. This method allows us to mimic effects such as those mentioned in section 6.2.2. We then measure the tracking efficiency as a function of the

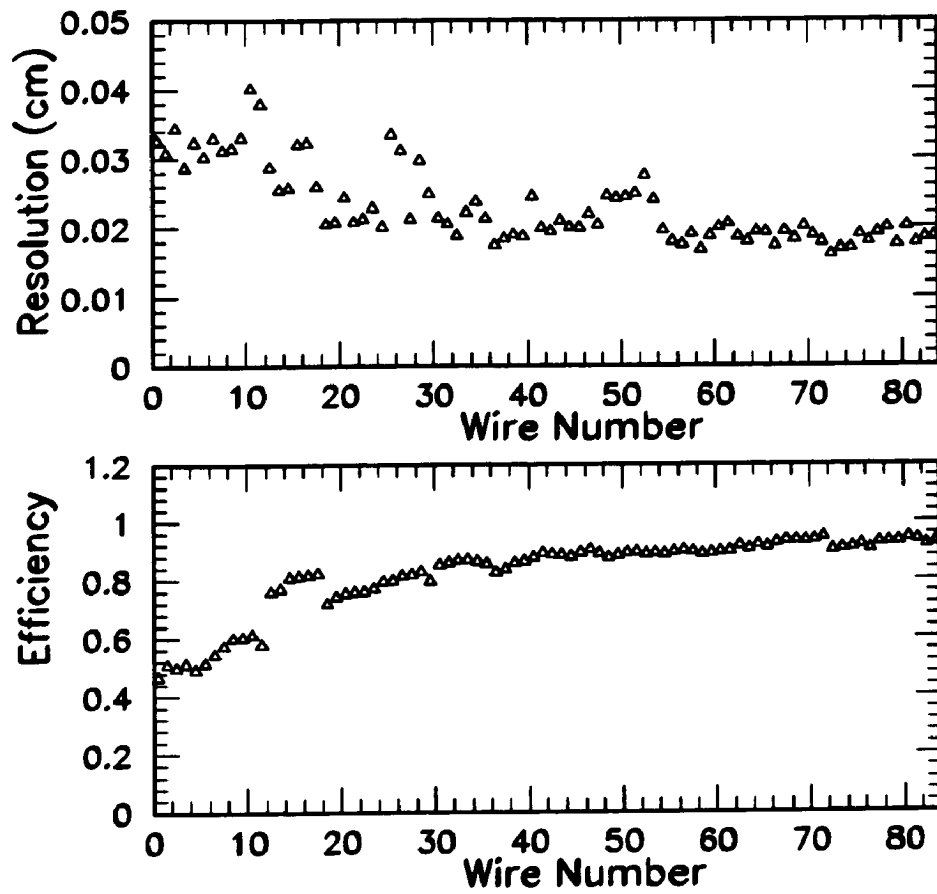


Figure 6.1: The measured CTC position resolution and wire efficiency.

$P_T$  of the track. This is shown in Figure 6.2, where it can be seen that for tracks with  $P_T \geq 2.0$ , the efficiency is flat as a function of  $P_T$ . The above track quality cuts imply that the efficiency will drop off as a function of track pseudorapidity, since tracks with larger pseudorapidity will exit the chamber having hit less wires. In addition, the true efficiency of the chamber itself also drops off at larger pseudorapidity. The combined effect is shown in Figure 6.3, where the efficiency is observed to drop for  $\eta \geq 1.0$ .

### 6.3 Determining the Beam Position

We refer here to the  $xy$  position of the  $p\bar{p}$  hard scatter; as noted previously, the  $z$  position of the  $p\bar{p}$  collision is determined by the VTPC. Knowledge of the beam position is needed at a later stage in the analysis and will be discussed in a subsequent section. For now, we describe the measurement of the  $x, y$  position of the interaction point.

The proton and anti-proton beams have a slight slope with respect to the  $z$  axis as they approach the nominal collision point at  $z = 0$ . This property introduces a dependence of the collision point on the  $z$  vertex of the event.

In addition, the collision point itself (at  $z = 0$ ) is offset from the point  $x = 0$ ,  $y = 0$ . Since each new store (i.e. new batch of protons and anti-protons injected into the Tevatron) has slightly different parameters, the above slope and offset are both

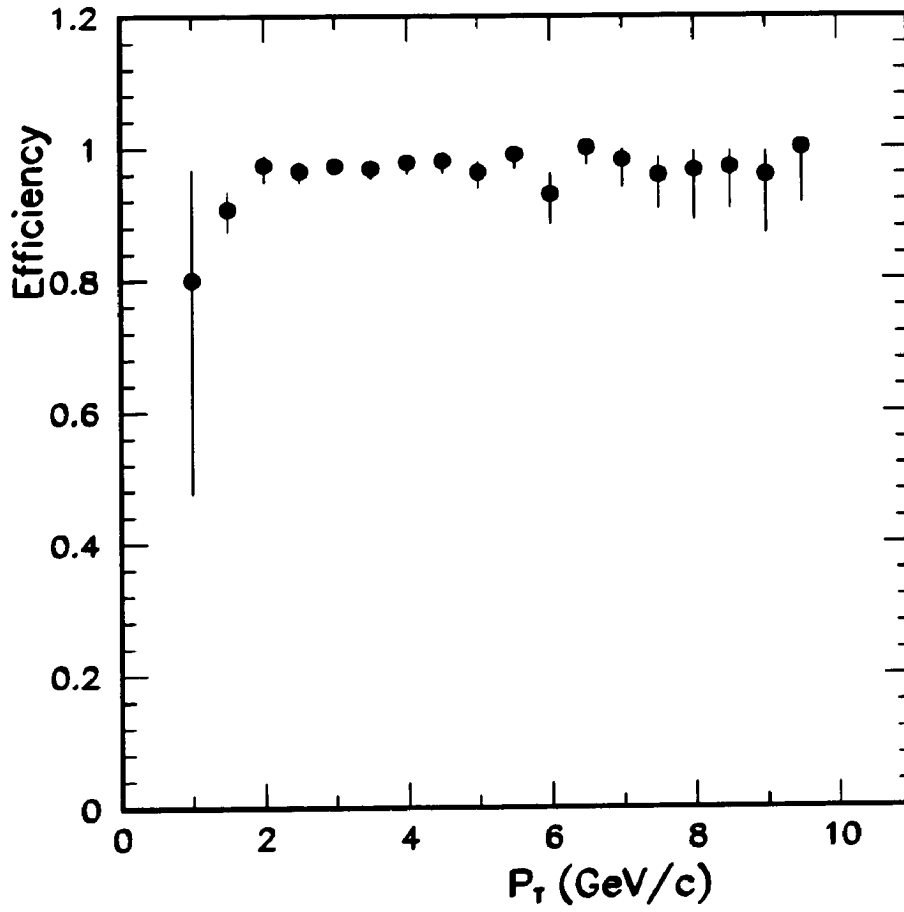


Figure 6.2: CTC track reconstruction efficiency as a function of track  $P_T$ . The error bars are binomial.



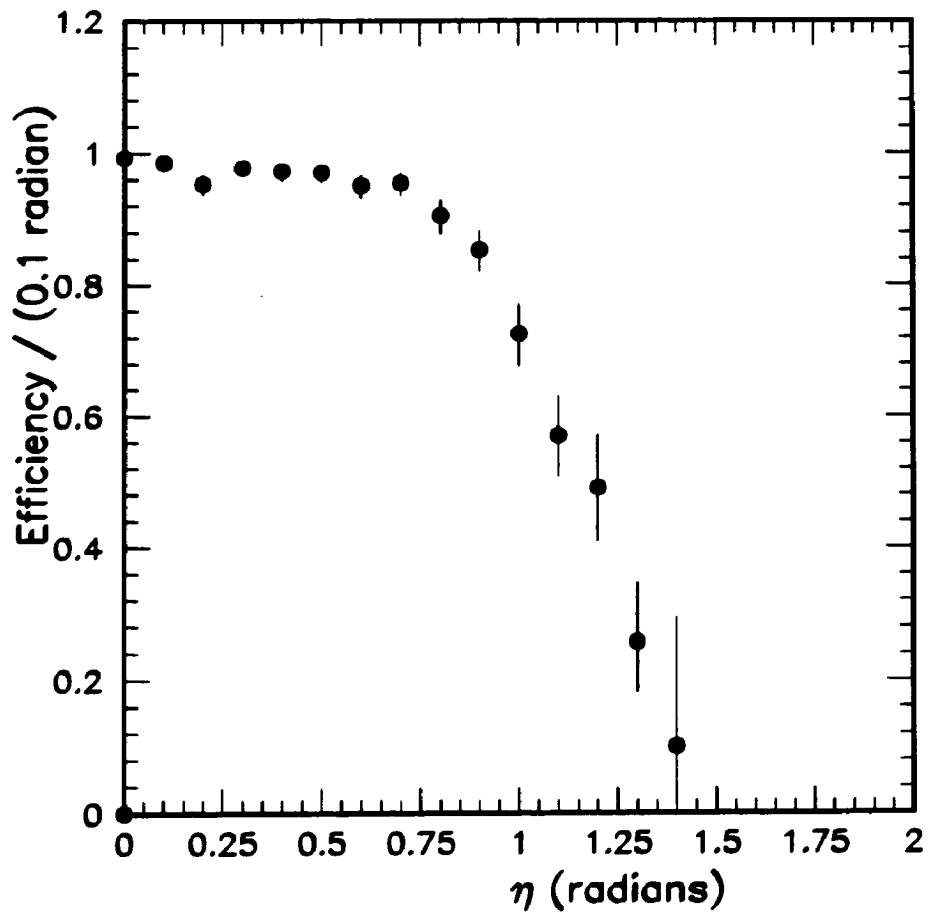


Figure 6.3: CTC track reconstruction efficiency as a function of track detector  $\eta$ . The error bars are binomial.

functions of the store, and so must be measured separately for each store.

The determination [47] of the beam positions was accomplished with a sample of high momentum (i.e. low curvature) tracks from each store. The true impact parameter  $D_0^{true}$  of each track can be related to the beam position  $(x_B, y_B)$  and the measured parameters  $D_0$  and  $\phi_0$  with the following equation:

$$D_0^{true} = D_0 + y_B \cos \phi_0 - x_B \sin \phi_0$$

assuming negligible difference between  $\phi_0^{true}$  and  $\phi_0$ .

The procedure for determining the beam position  $(x_B, y_B)$  for a large number of tracks is a simple  $\chi^2$  minimization technique. The coordinate  $(x_B, y_B)$  is that point in the  $xy$  plane that minimizes the width of the distribution of  $D_0^{true}$  for the large set of high momentum tracks. The average offsets for the beam position at  $z = 0$  were:

$$x_B = 70\mu\text{m}$$

$$y_B = -1200\mu\text{m}$$

with a statistical accuracy of typically  $\leq 1.0\mu\text{m}$ .

## 6.4 Track Reconstruction in the CMU

For track reconstruction [48] in the CMU, a local coordinate system is defined in the following manner. The 4 layers of the CMU are numbered from 0 to 3. The local  $z$  axis is the same as the global  $z$  axis. Then, within each wedge, the  $y$  axis lies

along a radial line from the global detector center through the center of the wedge. with  $y_{CMU} = 0$  defined to coincide with layer 0. The  $x_{CMU}$  axis lies perpendicular to the  $y_{CMU}$  axis, with  $x_{CMU} = 0$  at the center of the wedge, and  $x_{CMU}$  increasing as global  $\phi$  increases. The track reconstruction is done separately in the  $xy$  plane (corresponding to TDC information), and in the  $zy$  plane (corresponding to ADC information).

#### 6.4.1 Algorithm

The reconstruction algorithm proceeds along the following lines:

- The total number of TDC hits ( $\equiv$  NHITX) and ADC hits ( $\equiv$  NHITZ) are determined for each wedge.
- The tracking in the  $xy$  plane is performed first:
  - If NHITX = 2, and the hits are in different layers, and the hits are (at least) in adjacent cells, then the track is good. Note that two hit tracks will have a slope ambiguity, and will be counted as two separate tracks.
  - If NHITX  $\geq$  3, and the hits are in 3 different layers, then the track is good.
  - If NHITX  $\leq$  5, then assume that there is only one track in the wedge.
  - Once a track is found in the wedge, attach hits to the track that are within 0.25 cm ( $\sim 10\sigma$ ) of the fitted track. A few iterations on this step may be

necessary.

- Finally, calculate the slope and the intercept of the track.
- Then the tracking in the  $zy$  plane is performed:
  - If  $NHITZ = 2$ , and the hits are in different layers, and the hits are (at least) in adjacent cells, and  $NHITX = 2$ , then the track is good.
  - If  $NHITZ \geq 3$ , and the hits are in 3 different layers, then the track is good.
  - If  $NHITZ \leq 5$ , then assume that there is only one track in the wedge.
  - Once a track is found in the wedge, attach hits to the track that are within 5.0 cm ( $\sim 10\sigma$ ) of the fitted track. A few iterations on this step may be necessary.
  - Finally, calculate the slope and the intercept of the track.
- Tracks in the  $xy$  plane are matched with tracks in the  $zy$  plane. If there is no  $zy$  plane match for a  $xy$  track, then look for at least 2  $zy$  plane hits and form a  $zy$  plane track.

#### 6.4.2 Wire Resolution and Efficiency

In Figure 6.4 (a), we show the residual ( difference between the hit position returned by the CMU fit and the measured hit position) distribution for CMU tracks in the  $xy$  plane. This plot indicates that the position resolution in the  $xy$  plane is approximately

0.03cm. In Figure 6.4 (b), we show the number of hits attached to the reconstructed CMU track. If one assumes that the efficiency for a given hit to be attached to a reconstructed CMU track is independent of CMU layer, then the probability that 4 hits will be attached to a CMU track is:

$$P_4 = \epsilon^4$$

where  $\epsilon$  is the single hit efficiency. Similarly, the efficiency for 3 hits to be attached to a CMU track is:

$$P_3 = 4\epsilon^3(1 - \epsilon).$$

Therefore, by taking the ratio of the number of tracks with 3 hits to the number of tracks with 4 hits, we arrive at a relation for the single wire efficiency:

$$\frac{N_3}{N_4} = \frac{P_3}{P_4} = \frac{4(1 - \epsilon)}{\epsilon}$$

or

$$\epsilon = \frac{4}{\frac{N_3}{N_4} + 4}$$

The observed single hit efficiency is therefore  $(91.3 \pm 2.6)\%$ .

In Figure 6.5, we show the residual distribution and the hit number distribution for reconstructed CMU tracks in the  $zy$  plane. This plot indicates that the position resolution in the  $zy$  plane is approximately 0.6cm, with a single hit efficiency of  $(96.4 \pm 4.8)\%$ .

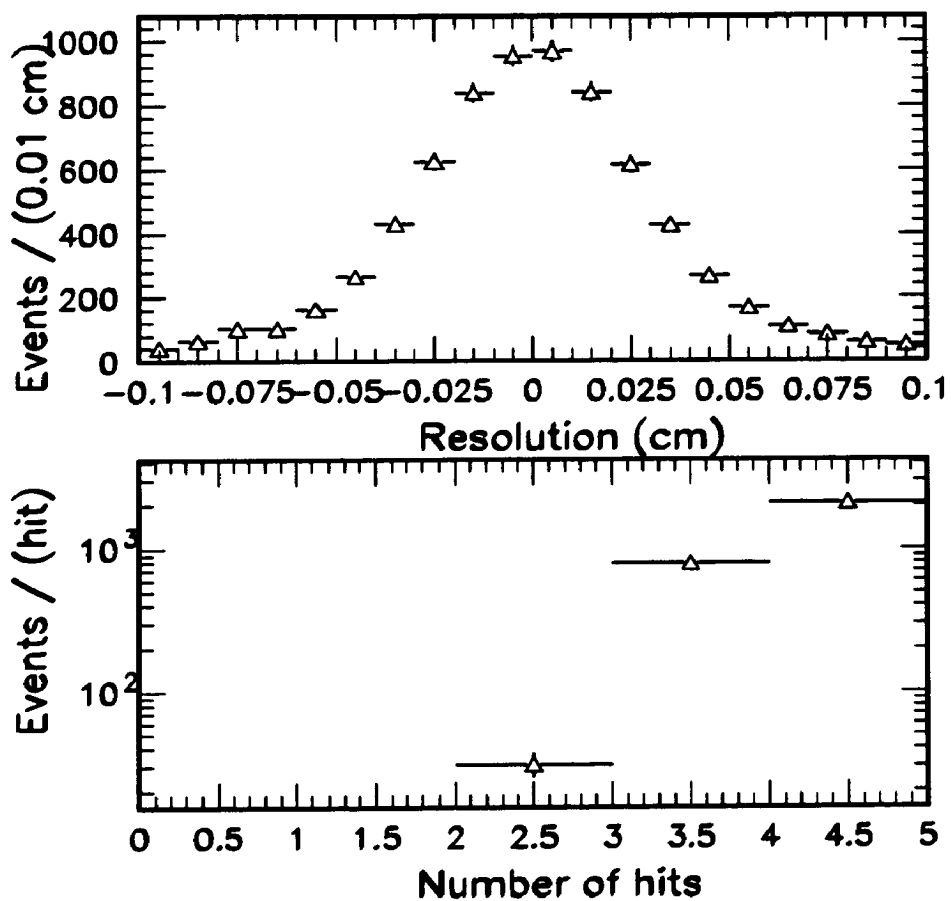


Figure 6.4: CMU track reconstruction results in the  $xy$  plane. In (a) we show the residual distribution and in (b) we show the distribution of the number of hits attached to the reconstructed track.

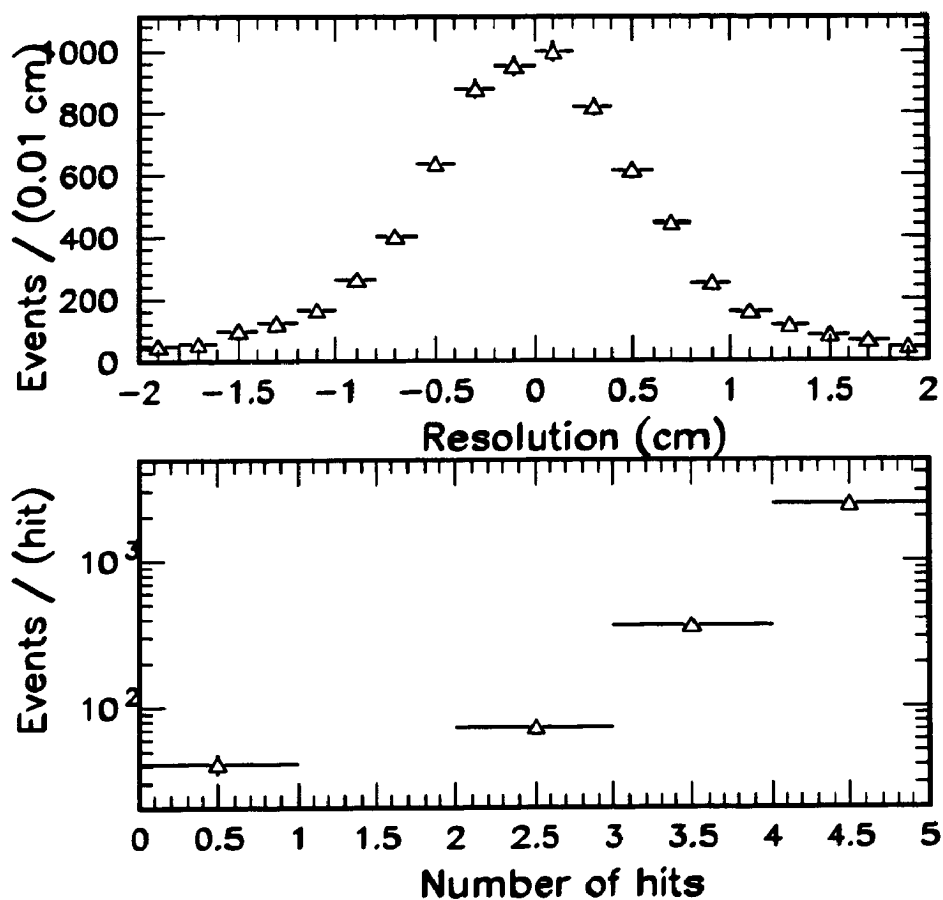


Figure 6.5: CMU track reconstruction results in the  $zy$  plane. In (a) we show the residual distribution and in (b) we show the distribution of the number of hits attached to the reconstructed track.

### 6.4.3 CMU Track Reconstruction Efficiency

The efficiency of the above algorithm has been tested using Monte Carlo models of the CMU chambers. This is reasonable since the occupancy in the CMU is so low. The Monte Carlo model was tuned to reproduce the efficiency and resolution distributions described in the above section. The CMU track reconstruction efficiency was found to be  $> 99\%$ .

## 6.5 Linking CMU tracks with CTC tracks

This part of the offline package attempts to associate tracks reconstructed in the CMU, with tracks reconstructed in the CTC.

### 6.5.1 Algorithm

The method used to link CMU-CTC tracks proceeds as follows:

- The CTC track sample is defined by these cuts:
  - Track  $P_T \geq 1.0$  GeV/c before the matching procedure. This cut is increased to 2.0 GeV/c after the matching procedure is finished.
  - The track  $D_0$  must be  $\leq 1.0$  cm. This cut is intended to remove  $\pi^\pm \rightarrow \mu^\pm \nu$  and  $K^\pm \rightarrow \mu^\pm \nu$  decays which occur before the track enters the CTC.
  - The mean residual of the axial hits attached to the track must be  $\leq 1.0$  cm. This cut is intended to remove  $\pi^\pm$  and  $K^\pm$  decays which occur inside



the active volume of the CTC.

- Loop over all CTC tracks passing the above cuts, extrapolate the CTC track to the radius of the muon chambers, and label the CTC track with the wedge number it is in. If at this radius, the CTC track is more than 35 cm from the center of the wedge, then also label the CTC track with the number of the nearest neighbor wedge. This second step is necessary due to multiple scattering in the calorimetry. (Note: The width of the wedge at the beginning of the muon chamber is 92 cm, while the width of the muon chambers at this point is only 76 cm.)
- For each track which is labeled with a wedge number that contains a CMU track, calculate a  $\chi^2$  based on the difference in slope and intercept (in the  $xy$  plane only) of the CMU track and the extrapolated CTC track. The errors used in the  $\chi^2$  calculation are assumed to be due to multiple scattering only (in practice this is a very good assumption). Furthermore, rather than weighting the errors by momentum (which is the proper form for the multiple scattering terms), equal weights independent of track momentum are assumed. This was done because of a possible bias against high momentum muons which might have a large  $\chi^2$  due to misalignment of the CMU relative to the CTC, and not because of a true mismatch.

- Finally, the CTC track with the best  $\chi^2$  is attached to the CMU track, and a candidate muon is formed.

### 6.5.2 CMU-CTC Link Quality Cuts

As mentioned previously, a CTC track is associated with a CMU track by extrapolating the CTC track from the outer radius of the CTC, through the return-field region of the calorimetry, to the first layer of the CMU system. The CTC track can then be characterized by a slope and intercept within the local coordinate system of the CMU, in the  $xy$  and  $zy$  planes separately. The CMU track is similarly characterized by its slope and intercept in the  $xy$  and  $zy$  planes. In the absence of intervening material in the region between the CTC and the CMU, one would expect quite good agreement in the two sets of variables. Of course, there is material, and the goodness of the match between the CTC and CMU tracks is determined by the following matching variables:

- $S_X$  = difference in  $xy$ -slope
- $I_X$  = difference in  $xy$ -intercept
- $S_Z$  = difference in  $zy$ -slope
- $I_Z$  = difference in  $zy$ -intercept

Multiple coulomb scattering in the region preceding the CMU degrades the match of the CTC and CMU track, increasing the magnitude of the above matching variables. This scattering is dependent on the momentum of the muon candidate. Since we know the total amount of material, we can calculate the expected scattering that muon candidates will experience in this region. The effect of the scattering on the above matching variables will be to smear them with Gaussian distributions centered on zero, with widths given by [49]:

$$\begin{aligned}\sigma_{S_x}^2 &= \left(\frac{0.131}{P_T}\right)^2 \frac{0.27 + 0.73/\sin\theta}{1 - 1.43/P_T} + (0.0062)^2 \\ \sigma_{I_x}^2 &= \left(\frac{13.8\text{cm}}{P_T}\right)^2 \frac{0.59 + 0.41/\sin\theta}{1 - 0.71/P_T} + (0.3\text{cm})^2 \\ \sigma_{S_z}^2 &= \left(\frac{0.131}{P_T}\right)^2 \frac{0.27 + 0.73/\sin\theta}{1 - 1.43/P_T} (\sin\theta)^2 + (0.0062)^2 \\ \sigma_{I_z}^2 &= \left(\frac{13.8\text{cm}}{P_T}\right)^2 \frac{0.59 + 0.41/\sin\theta}{1 - 0.71/P_T} \frac{1}{(\sin\theta)^2} + (1.5\text{cm})^2\end{aligned}$$

where the first term in the above equation is the true contribution of multiple scattering, and the second term is due to measurement errors. In these equations,  $P_T$  is the transverse momentum of the track (as measured in the CTC) and  $\sin\theta$  is given by:

$$\sin\theta = \frac{1}{\sqrt{1 + (P_Z/P_T)^2}}$$

with  $P_Z$  being the momentum of the track in the  $Z$  direction. Using the above relations, we define normalized matching variables:

$$M_{I_x} = \frac{I_x}{\sigma_{I_x}}$$

$$M_{S_X} = \frac{S_X}{\sigma_{S_X}}$$

$$M_{I_Z} = \frac{I_X}{\sigma_{I_Z}}$$

$$M_{S_Z} = \frac{S_Z}{\sigma_{S_Z}}$$

In practice, it is found that by using only  $M_{I_X}$  and  $M_{I_Z}$  and by requiring all muon candidates to satisfy the following cuts:

- $|M_{I_X}| \leq 3.0$
- $|M_{I_Z}| \leq 3.0$

we ensure good muon identification. In Figure 6.6, we show the distributions for  $M_{I_X}$  and  $M_{I_Z}$  obtained using the cosmic ray muon sample. This figure indicates that the efficiency for the two cuts combined is  $(96.9 \pm 0.7)\%$ .

### 6.5.3 Link Efficiency

In addition to the above efficiency for passing the matching cuts, which we will call  $\epsilon_{mcut}$ , we also need to know the efficiency for linking a given CMU track with the correct CTC track, which we will call  $\epsilon_{clink}$ . Thus the total efficiency for linking CMU tracks with CTC tracks is:

$$\epsilon_{link} = \epsilon_{clink} \times \epsilon_{mcut}.$$

We can get an upper limit on  $\epsilon_{clink}$  by examining the data. We measure the number of times there is more than one CTC track which extrapolates to the same

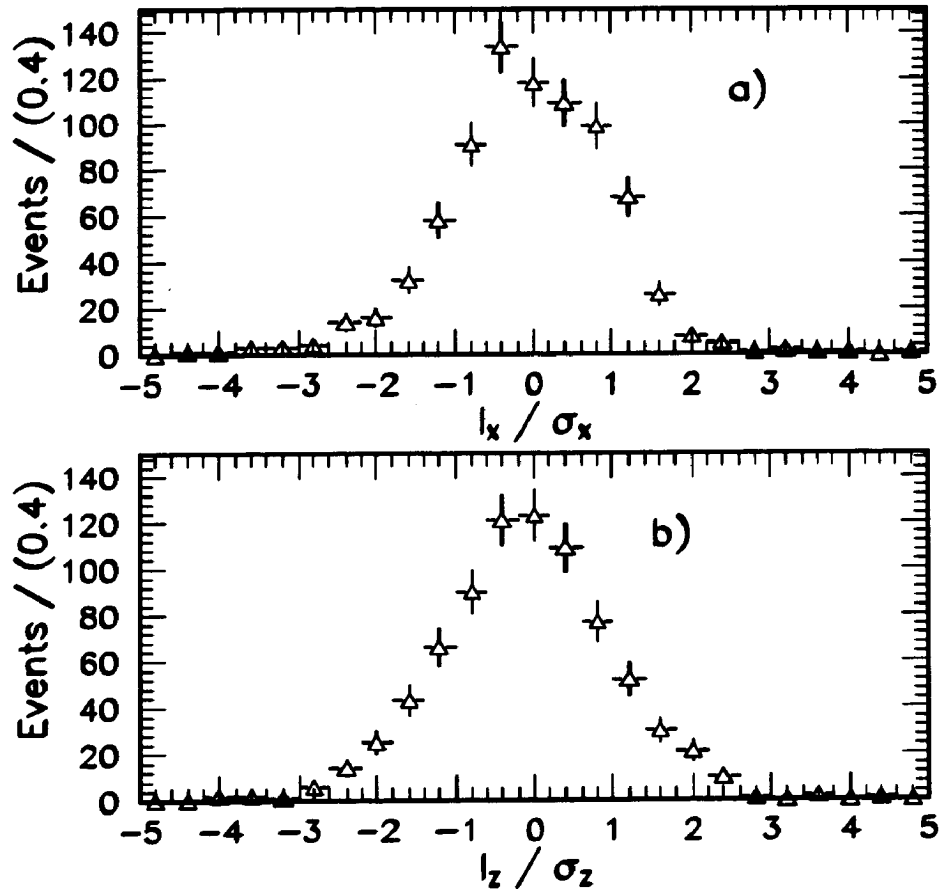


Figure 6.6: The distributions for  $M_{I_x}$  (top) and  $M_{I_z}$  (bottom) obtained using the cosmic ray muon sample. The error bars are statistical.

wedge of a CMU track. We find that in 8% of the cases there is a link between a CMU track and a CTC track, there is another CTC track which can be extrapolated to the same wedge. So  $\epsilon_{clink} \geq 0.92$  since it is possible to make a mistake in only 8% of the cases.

To further extend this method, we use a Monte Carlo model to generate muon candidates. We then imbed the Monte Carlo CMU track in real data events. We ask how often there is another real data CTC track with a better  $\chi^2$  match with the Monte Carlo CMU track than the Monte Carlo CTC track. We only look at the subsample of real data tracks that extrapolate to the wedge of the Monte Carlo CMU track, and we find that  $2.3^{+0.9}_{-0.6}\%$  of the real data CTC tracks match the Monte Carlo CMU track better than the Monte Carlo CTC track. Combining this number with the 8% we observe in the data yields:

$$\epsilon_{clink} = 99.82^{+0.07}_{-0.05}\%.$$

Using the above number of  $\epsilon_{rcut} = (96.9 \pm 0.7)\%$ , we find:

$$\epsilon_{link} = (96.7 \pm 0.7)\%.$$

## 6.6 Vertexing and Mass Constraint Algorithms

The final stage in the offline reconstruction process concerns vertex and mass constraint algorithms. These algorithms are used typically when one is interested in calculating the invariant mass of a set of tracks. As an example, consider the decay

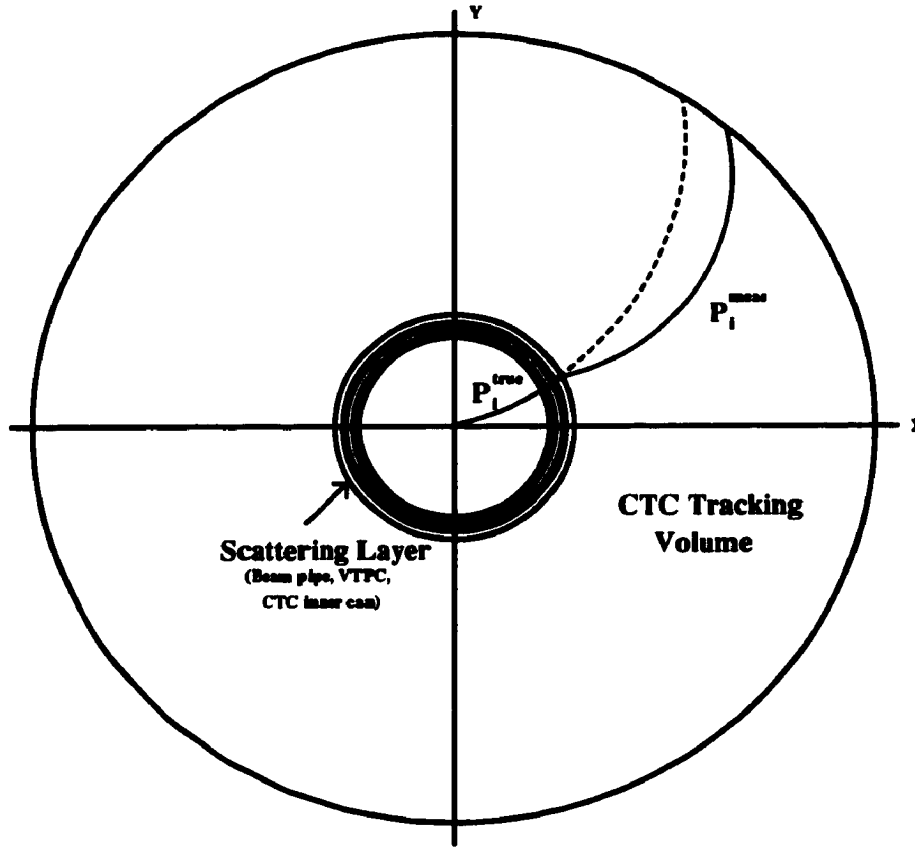


Figure 6.7: Illustration of the effects of multiple scattering on the path of a charged track from the inner beam pipe out through the CTC.

$B_u^- \rightarrow J/\psi + K^-$ , in which the  $J/\psi$  then decays as  $J/\psi \rightarrow \mu^+ \mu^-$ . In Figure 6.7, we illustrate the possible path in the CTC of one of the three charged tracks in this decay. In this picture, the inner cylinder represents the combined effects of multiple scattering and  $dE/dX$  energy losses due to material between the origin of the track inside the beam pipe and its measurement inside the CTC.

The true vectors of track momenta will be called  $P_i^{true}$ ; the vectors that are actually measured will be called  $P_i^{meas}$ . The true value of the mass of the decaying  $B$  meson

is given by:

$$M_B = \sqrt{E_{tot}^2 - P_{tot}^2}$$

with

$$E_{tot} = \sum_{i=1}^3 E_i^{true}$$

$$E_i = \sqrt{(P_i^{true})^2 + M_i^2}$$

$$P_i = \sqrt{(P_{xi}^{true})^2 + (P_{yi}^{true})^2 + (P_{zi}^{true})^2}$$

and  $M_i$  is the mass of the  $i^{th}$  particle, either muon or kaon. This equation is only truly valid if it is evaluated at the decay point of the  $B$  meson (the  $J/\psi$  lifetime is approximately zero and so the  $J/\psi$  decays at the same point). However, we must use the momenta  $P_i^{meas}$ , which is only an approximation. If we were to use the true momenta, a distribution of masses calculated in the above manner would have a full width of  $\sim 0$  for the  $B$  meson, and  $\sim 0.1 MeV/c^2$  for the  $J/\psi$ . Using the measured values results in widths of approximately  $30 MeV/c^2$ . This is the effect of detector resolution.

The use of constraints can help improve this. Since we know that the three tracks in this decay must come from the same point, we can vary the track parameters describing the helices of the three tracks until the three tracks intersect at a common point. This is called a vertex constraint. In addition, we know which of the two tracks are muons, and we know the two muons should form the  $J/\psi$  mass, which is measured as  $3.09693 \pm 0.00001$  [2], an accuracy much higher than our resolution. Once again,



we can vary the track parameters of the muon tracks until the mass of the track pair forms exactly  $3.09693 \text{ GeV}/c^2$ . This is called a mass constraint. Finally, we measure the  $B$  direction using CTC information fairly well. Since we know where the beam position is, we demand that the found vertex in the  $xy$  plane should lie along a line running along the  $B$ -meson direction through the beam position. In fact, since the  $B$ -meson lifetime is  $(c\tau_B) = 0.036 \text{ cm}$ , and the  $B$  mesons we consider have energies of  $\sim 12 \text{ GeV}/c^2$ , they travel on average a distance of  $\sim (c\tau_B) \times (12/5.3)$  or  $0.9 \text{ cm}$ . Therefore, we also constrain the vertex to be on the side of the beam position the  $B$ -meson momentum vector points. This is our pointing constraint.

Each of these constraints adds information, and results in values of  $P_i^{meas}$  which are closer in value to  $P_i^{true}$ . This leads to an effective improvement of our detector resolution, which leads to better signal-to-noise ratio. These constraints have been implemented using a least-squares-minimization technique [50].

### 6.6.1 Performance

We tested the algorithm on a Monte Carlo sample of  $B_u^- \rightarrow J/\psi + K^-$  decays. These decays were passed through a simulation of the CDF detector and analyzed with the same offline package. In Figure 6.8 (a) we show the  $\mu^+\mu^-K^-$  mass using only the track parameters measured in the CTC. In Figure 6.8 (b) we show the  $\mu^+\mu^-K^-$  mass after vertex constraining the 3 tracks. In Figure 6.8 (c) we show the  $\mu^+\mu^-K^-$  mass

**Table 6.1: Results of a test of constrained fits on a Monte Carlo sample of  $B_u^- \rightarrow J/\psi + K^-$  (with  $J/\psi \rightarrow \mu^+\mu^-$ ).**

Constraint Used	Width MeV/c <sup>2</sup>
No Constraint	$30.0 \pm 1.0$
Vertex Constraint Only	$20.0 \pm 1.0$
Vertex and Pointing Constraint	$18.0 \pm 1.0$
Vertex, Pointing, Mass Constraint	$12.0 \pm 1.0$

after a combined vertex and pointing constrained fit. Finally, in Figure 6.8 (d) we show the  $\mu^+\mu^-K^-$  mass after a combined vertex, pointing and mass constrained fit. One can see a steady improvement in the resolution, as more constraints are added, for a overall improvement of  $\sim 60\%$ . The details are summarized in Table 6.1.

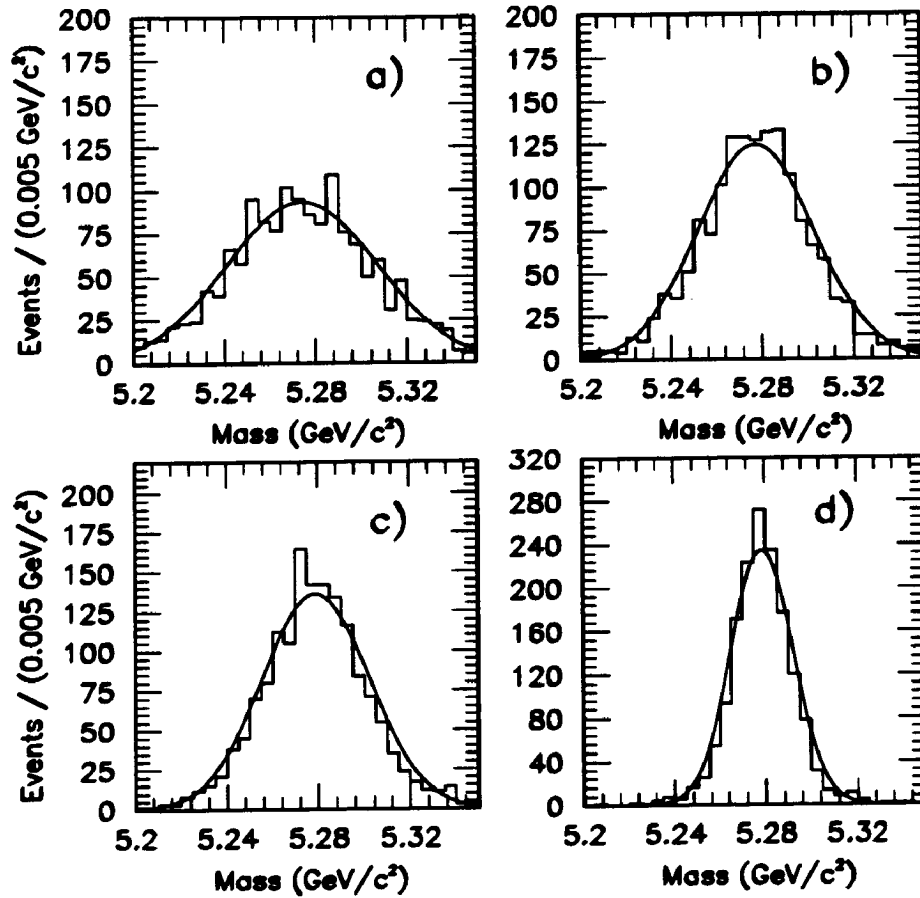


Figure 6.8:  $\mu^+\mu^-K^-$  mass distributions showing the effects of adding constraints. Figure (a) shows the  $\mu^+\mu^-K^-$  mass distribution with no constraints added, (b) has a vertex constraint, (c) has a vertex and pointing, and (d) has a combined vertex, pointing, and mass constraint.

## Chapter 7

### Reconstruction of Particle Decays

In this chapter we will outline the methods used to reconstruct particle decays using the  $J/\psi \rightarrow \mu^+\mu^-$  data sample. We begin by describing the various resonances observed in the  $\mu^+\mu^-$  data itself, before focusing in on the  $J/\psi$  signal.

#### 7.1 Data Sample

The events used in this analysis were selected from the Dimuon\_Central\_3 trigger sample with the requirement that each event contain two muon candidates of opposite charge, with each muon satisfying the cuts:

- $P_T \geq 3.0 \text{ GeV}/c$
- $|M_X| \leq 3.0$
- $|M_Z| \leq 3.0$

In addition, at least one muon candidate must have  $|I_X| \leq 10.0 \text{ cm}$ . These simply ensure good identification of the two candidate muons. The  $P_T$  cut is designed so

Table 7.1: Results of fitting the  $\mu^+\mu^-$  sample, showing for each resonance the fitted mass, width, and number of events ( $N^{rec}$  observed. The last column shows the deviation in % of the mass we observe from the world average.

Resonance	Mass (GeV/c <sup>2</sup> )	Width (MeV/c <sup>2</sup> )	$N^{rec}$	$\frac{(M_{fit}-M_{true})}{M_{true}}(\%)$
$J/\psi$	$3.099 \pm 0.001$	$21 \pm 1$	$1028 \pm 37$	$0.07 \pm 0.03$
$\psi(2S)$	$3.690 \pm 0.005$	$21 \pm 5$	$45 \pm 10$	$0.11 \pm 0.14$
$\Upsilon(1S)$	$9.452 \pm 0.010$	$78 \pm 10$	$189 \pm 22$	$-0.09 \pm 0.11$
$\Upsilon(2S)$	$10.063 \pm 0.047$	$125 \pm 43$	$64 \pm 21$	$0.40 \pm 0.47$

that the trigger efficiency of the data sample is well understood.

In Figure 7.1 we show the invariant mass of the  $\mu^+\mu^-$  sample satisfying the above cuts. In this plot one can clearly see resonances corresponding to the  $J/\psi$ ,  $\psi(2S)$ ,  $\Upsilon(1S)$  and  $\Upsilon(2S)$  mesons. In fact, the positions of the peaks can be used to test the overall mass scale. Each resonance is fit with a Gaussian distribution representing the signal and a linear function representing the non-resonant  $\mu^+\mu^-$  pairs and background. The fits are shown in Figure 7.2, and in Table 7.1 the fit results are listed. In the last column of this table, we compare the fit results for the means of the resonances with the world average values [2]. The table indicates an error in the mass scale consistent with 0.1%.

For the remainder of this analysis, we will concentrate on the  $J/\psi$  signal. When we refer to  $J/\psi$  events, we will always imply events containing two muons that satisfy

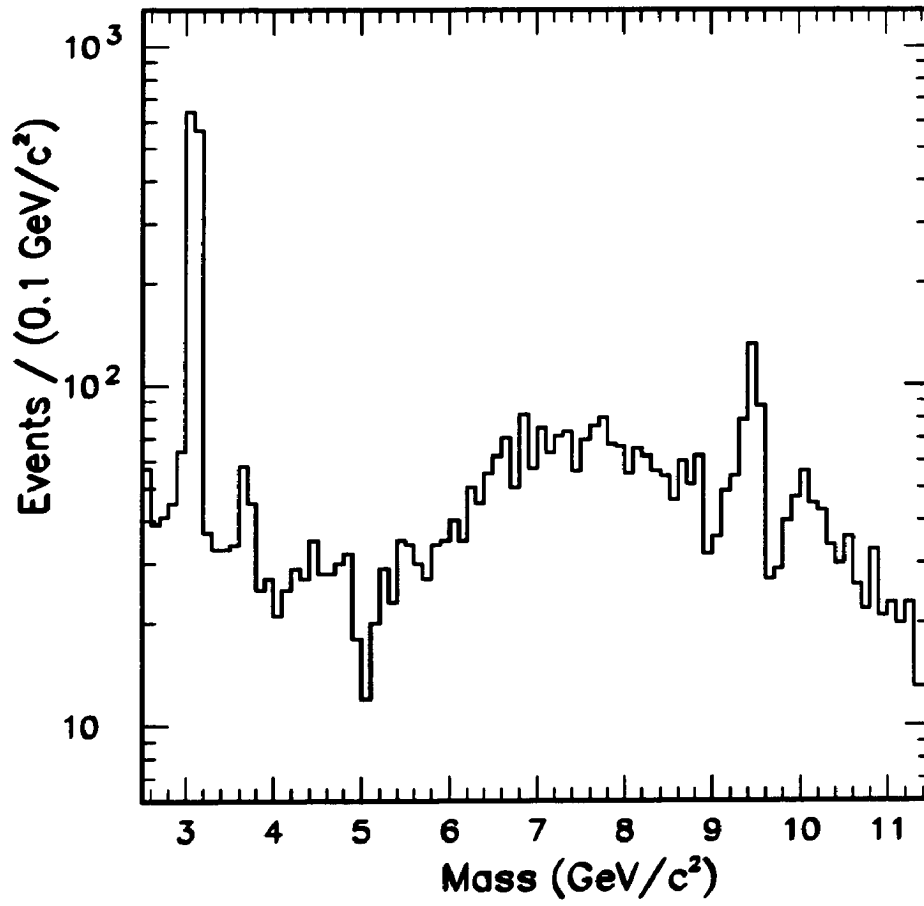


Figure 7.1: Invariant mass of the  $\mu^+\mu^-$  data sample for the cuts described in the text.

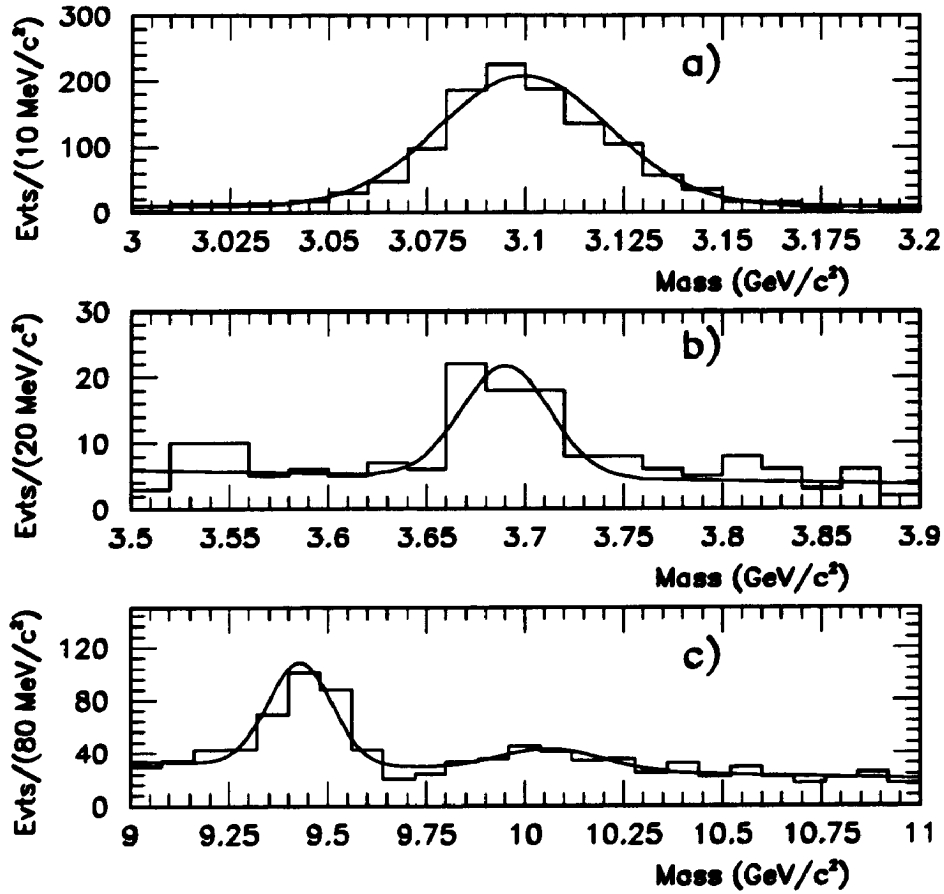


Figure 7.2: Fit results in the  $\mu^+\mu^-$  data sample. (a)  $\mu^+\mu^-$  mass distribution in the region of the  $J/\psi$  meson. (b)  $\mu^+\mu^-$  mass distribution in the region of the  $\psi(2S)$  meson. (c)  $\mu^+\mu^-$  mass distribution in the region of the  $\Upsilon(1S)$  and  $\Upsilon(2S)$  mesons.

the above cuts, and whose  $\mu^+\mu^-$  mass is within  $3\sigma$  of the world average  $J/\psi$  mass of  $3.0969 \text{ GeV}/c^2$ . Here  $\sigma$  refers to the Gaussian parameter listed in Table 7.1, which for the  $J/\psi$  is  $21 \text{ MeV}/c^2$ .

## 7.2 Isolation of $\psi(2S) \rightarrow J/\psi\pi^+\pi^-$

We now turn to reconstruction of the decay:

$$\psi(2S) \rightarrow J/\psi\pi^+\pi^-$$

in which the  $J/\psi$  has already been identified in the  $\mu^+\mu^-$  sample above. Identifying this decay is an important test of one's ability to reconstruct a multi-body decay involving the  $J/\psi$ . In addition, the  $\psi(2S)$  is thought to originate almost entirely from  $B$  meson decay, and therefore identifying this decay is a good precursor to reconstructing full  $B$  meson decays.

The  $\pi^+\pi^-$  pair is identified as a pair of oppositely-charged tracks in the CTC. The reconstruction procedure begins with a  $J/\psi$  candidate passing the loose  $P_T$  cuts. One then loops over all oppositely charged tracks in the CTC (except the muons from the  $J/\psi$  decay), simultaneously vertex constraining the 4 tracks, and mass constraining the 2 muons to the world average  $J/\psi$  mass. In addition, we require that the 2 pions be close to the  $J/\psi$  momentum direction by applying the following cut:

$$\cos \theta_{J/\psi-\pi} \geq 0.5.$$



In Figure 7.3, we show the resulting invariant mass of the 4 tracks.

By fitting the observed resonance with to a Gaussian distribution, with a linear function describing the background, we obtain a mean of  $3.685 \pm 0.001 \text{ GeV}/c^2$ , in good agreement with the result obtained in the  $\psi(2S) \rightarrow \mu^+\mu^-$  channel. We see  $32 \pm 9$  events in the signal, with  $\sigma = 5.0 \pm 0.3$  for the width of the Gaussian.

### 7.3 Isolation of $B_u^- \rightarrow J/\psi + K^-$

We now turn to reconstruction of the decay:

$$B_u^- \rightarrow J/\psi + K^-.$$

There are a number of reasons that make a search for this decay mode favorable:

- The branching ratio for this mode has been measured and found to be large.

$$Br(B_u^- \rightarrow J/\psi + K^-) = (0.08 \pm 0.02 \pm 0.02)\%$$

This is approximately 10% of the total decay rate of  $B^- \rightarrow J/\psi + X$ .

- The combinatoric background to this decay, relative to other possible decay modes, is small. If the charged track multiplicity in a given event containing a  $J/\psi$  is  $n$ , then the combinatoric background (i.e., the number of possible  $J/\psi$  -track combinations) for this decay mode will also be  $n$ . In a decay such as  $B_d^0 \rightarrow J/\psi + K^{*0}$ , where the  $K^{*0}$  must be identified through its decay  $K^{*0} \rightarrow K^+\pi^-$ , the combinatoric background will go as  $n(n-1)$ .

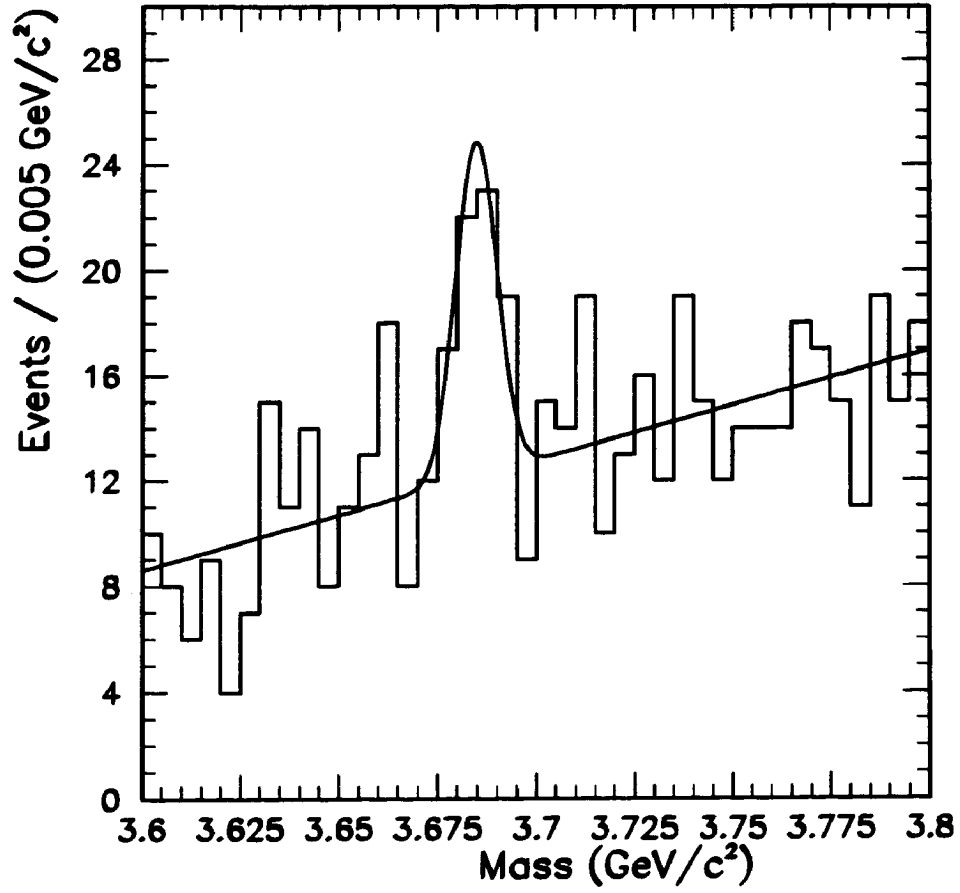


Figure 7.3:  $J/\psi \pi^+ \pi^-$  mass distribution in the region of the  $\psi(2S)$  meson.

In addition to the cuts on the  $J/\psi$ , there are cuts needed to reduce the random combinatoric background. These cuts are designed so that the efficiency for real  $B^-$  meson decays is high, while that for the background is low. In Figure 7.4 we show the  $P_T$  of kaon candidates in the data, where the data sample here is defined by events containing identified  $J/\psi$  mesons. In this Figure we also show a Monte Carlo prediction of the  $P_T$  distribution for kaons in the decay  $B_u^- \rightarrow J/\psi + K^-$ . One can see that the data sample tends to populate the very low  $P_T$  region. In Figure 7.5 we show the  $P_T$  of all  $B^-$  meson candidates in the same data sample. In this Figure we also show a Monte Carlo prediction of the  $P_T$  distribution for  $B^-$  mesons. Once again, the data tend to populate a lower- $P_T$  region. These distributions motivate the following cuts:

- $K^- \ P_T \geq 2.0 \text{ GeV}/c$  .
- $B^- \ P_T \geq 9.0 \text{ GeV}/c$  .

In Figure 7.6 we show the  $J/\psi + K^-$  mass distribution for events satisfying all of the above cuts. There is a clear peak in the region  $5.26 - 5.32 \text{ GeV}/c^2$ , where one would expect the  $B^-$  meson to appear. To verify that the signal is robust under the variation of the chosen cuts, we show in Figure 7.7 the  $J/\psi + K^-$  mass distribution after lowering the  $P_T$  cut on the muons from  $3.0 \text{ GeV}/c$  to  $2.0 \text{ GeV}/c$ . The signal increases by approximately 30%, while there is a noticeable increase in the background. In Figure 7.8, we show the  $J/\psi + K^-$  mass distribution after lowering the  $P_T$  cut on

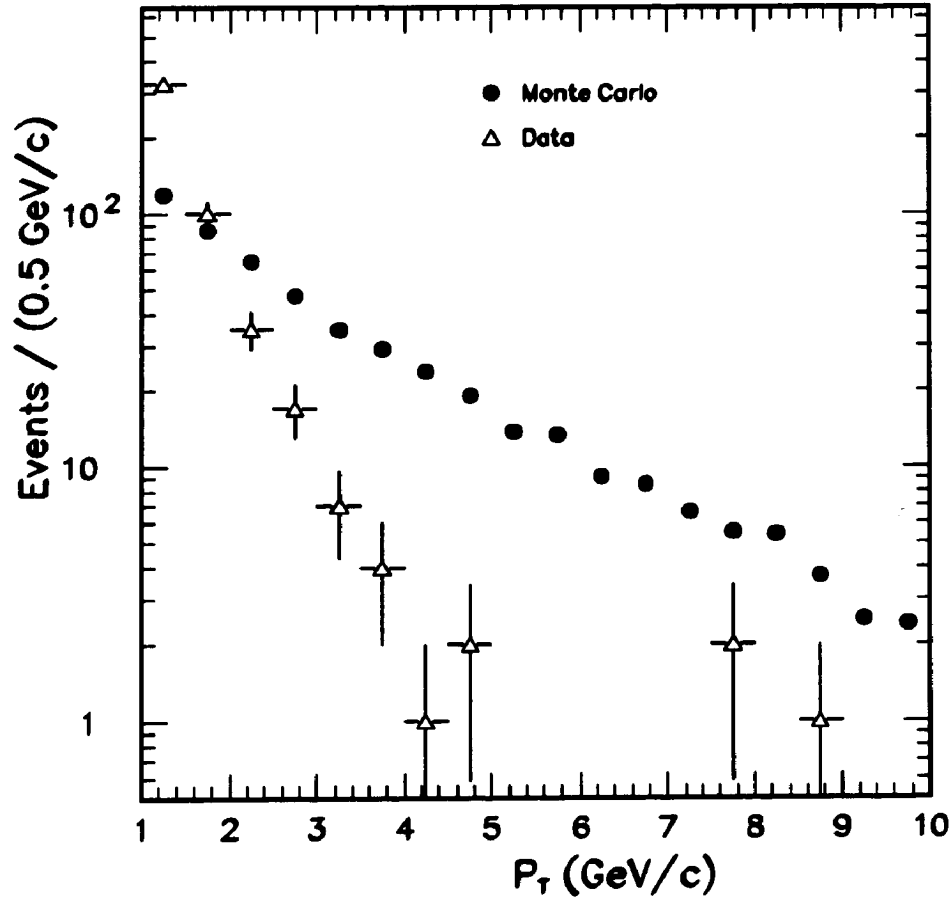


Figure 7.4: The  $P_T$  spectrum for candidate  $K^-$  observed in the data compared with the Monte Carlo spectrum for  $K^-$  in the decay  $B_u^- \rightarrow J/\psi + K^-$ . The error bars are statistical.

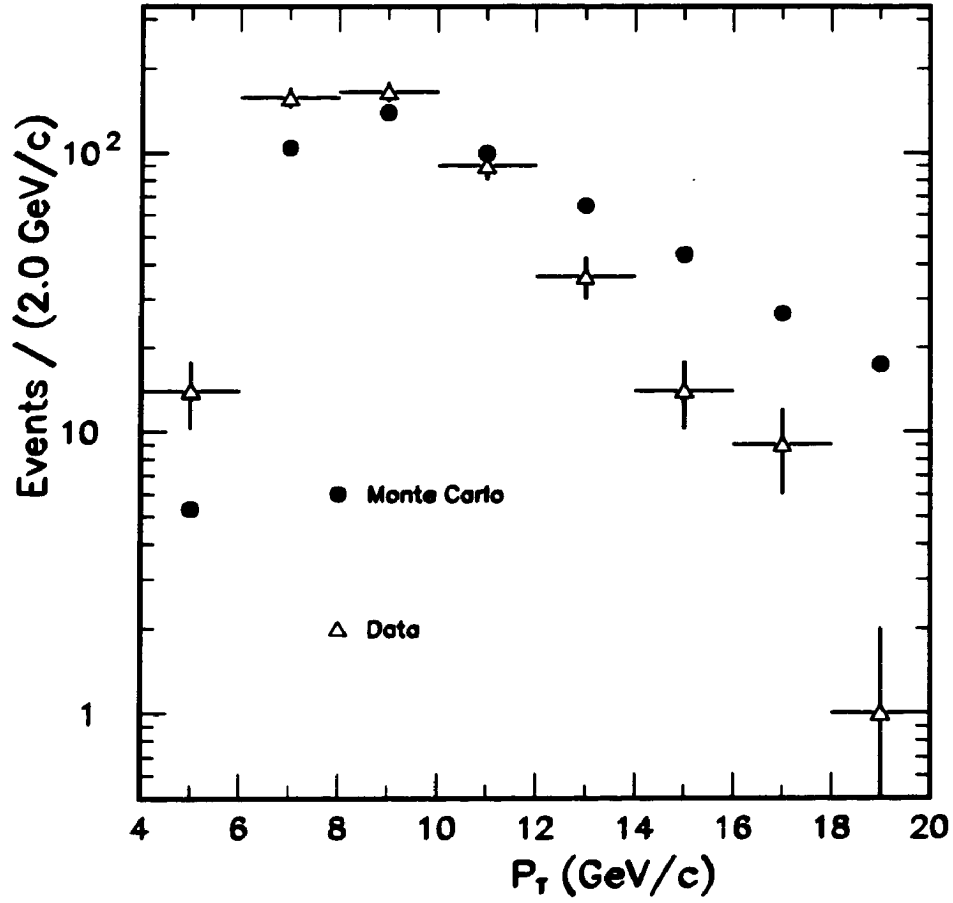


Figure 7.5: The  $P_T$  spectrum for candidate  $B^-$  mesons observed in the data compared with the Monte Carlo spectrum for true  $B^-$  mesons. The error bars are statistical.

the kaon from 2.0 GeV/c to 1.0 GeV/c . Once again, we see a significant increase in the signal.

#### 7.4 Determining the Origin of the Background for $B_u^- \rightarrow J/\psi + K^-$

We would like to verify that the shape of the background in the  $B_u^- \rightarrow J/\psi + K^-$  mass plot is approximately flat, or at least that it does not peak in the region where we see our signal. There are two major sources of background to this decay. One possibility is background due to *fake*  $J/\psi$ s. In Figure 7.9, we show the  $J/\psi$  signal we use. The shaded central region forms that part of the  $\mu^+\mu^-$  mass distribution we call our signal. This plot shows that the  $\sim 1000$  signal  $J/\psi$  's sit above  $\sim 130$  *fake*  $J/\psi$  's. To determine the probability that these "fake"  $J/\psi$  's are significantly contributing to our observed  $B_u^- \rightarrow J/\psi + K^-$  signal, we use the shaded  $\mu^+\mu^-$  regions on either side of the central  $\mu^+\mu^-$  resonance. These regions are  $2.90 - 3.00$  GeV/c<sup>2</sup> and  $3.20 - 3.30$  GeV/c<sup>2</sup> , respectively. The resulting *fake*  $J/\psi + K^-$  distribution is shown in Figure 7.10. We observe only 6 events total. However, the *fake*  $\mu^+\mu^-$  region we consider is almost twice as large as in our true sample, so the *fake*  $J/\psi$  sample contributes less than 4 events to our observed background of almost 50 events. It is clear that the *fake*  $J/\psi + K^-$  sample is uncorrelated with the observed peak.

The other major background possibility is due to random combinatorics. In an event containing a real  $B$  meson, there are a large number of charged tracks present,

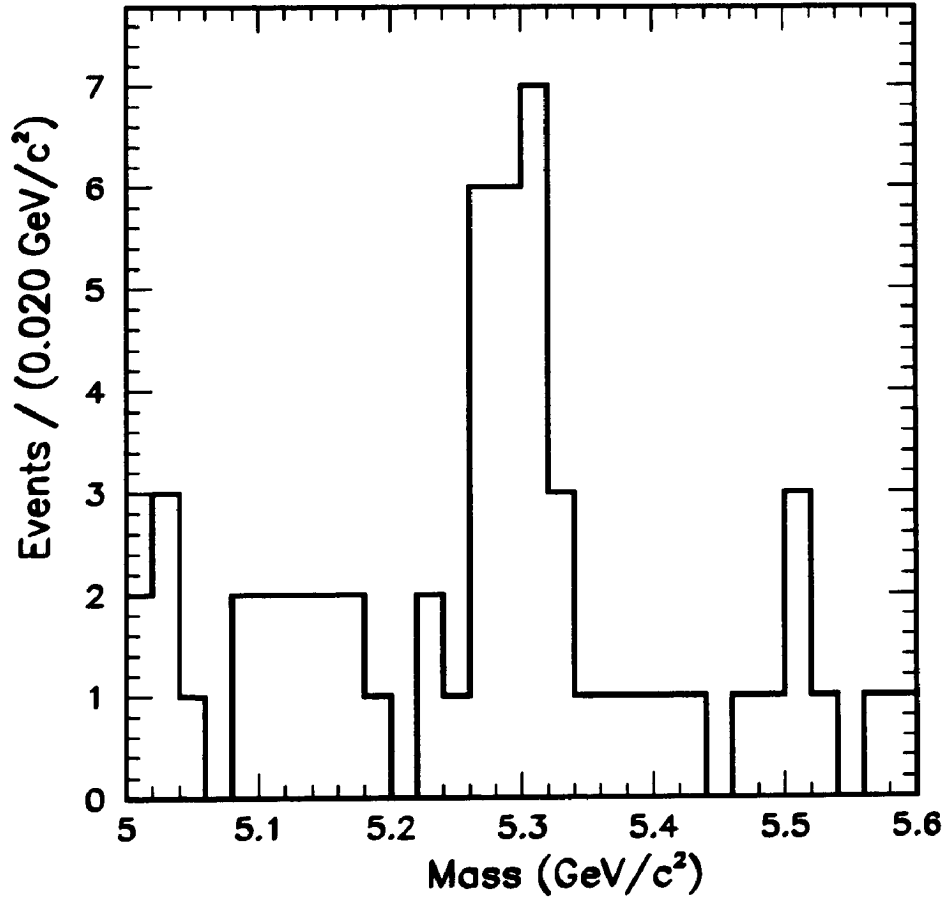


Figure 7.6:  $J/\psi + K^-$  mass distribution in the region of the  $B^-$  meson, for the cuts described in the text.

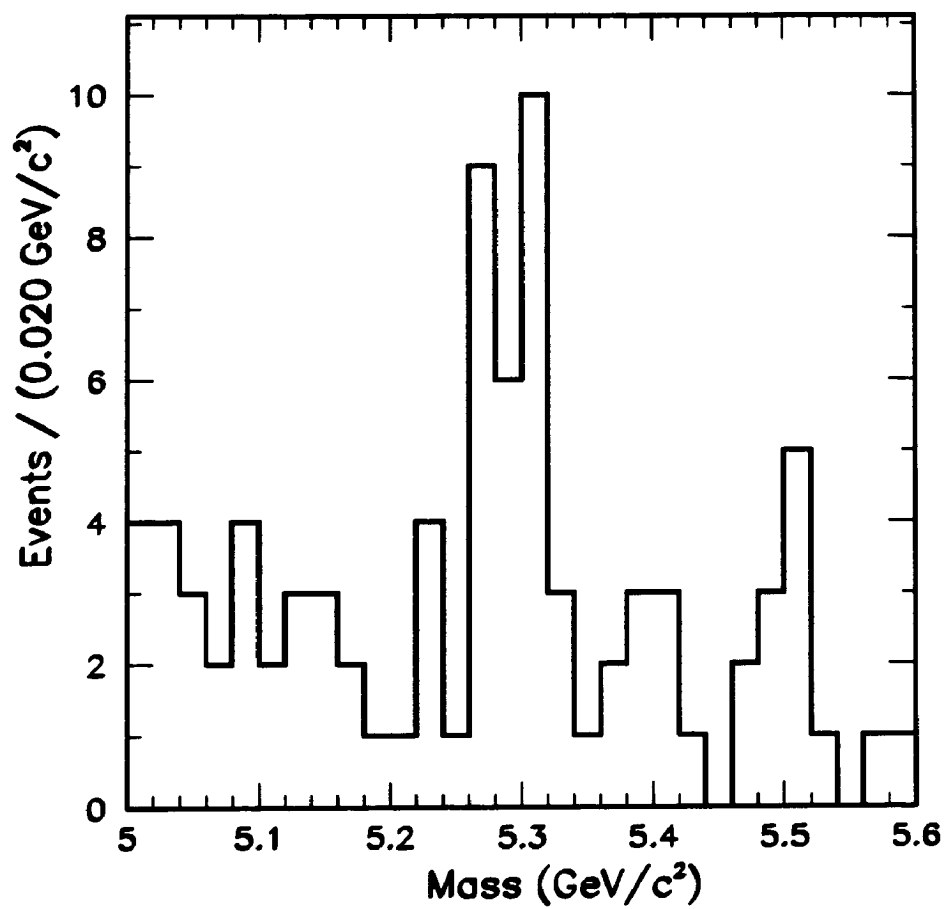


Figure 7.7:  $J/\psi + K^-$  mass distribution after lowering the muon  $P_T$  cut from 3.0 to 2.0 GeV/c .



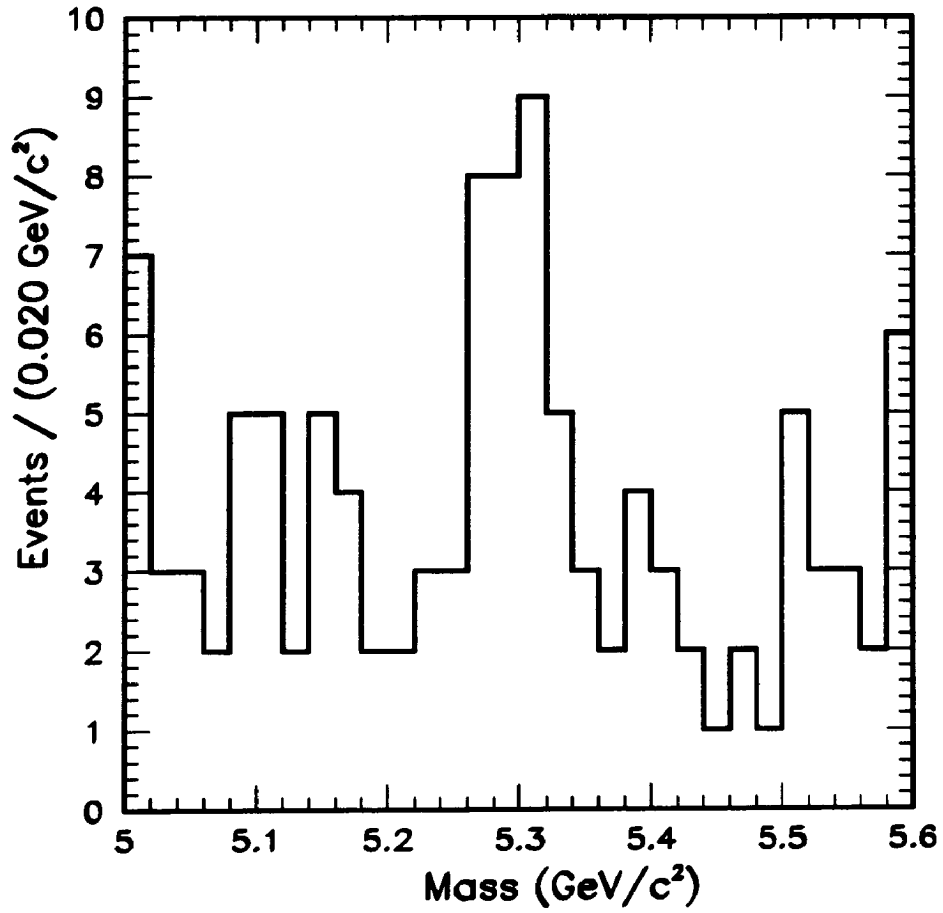


Figure 7.8:  $J/\psi + K^-$  mass distribution after lowering the kaon  $P_T$  cut from 2.0 to 1.0  $\text{GeV}/c$ .

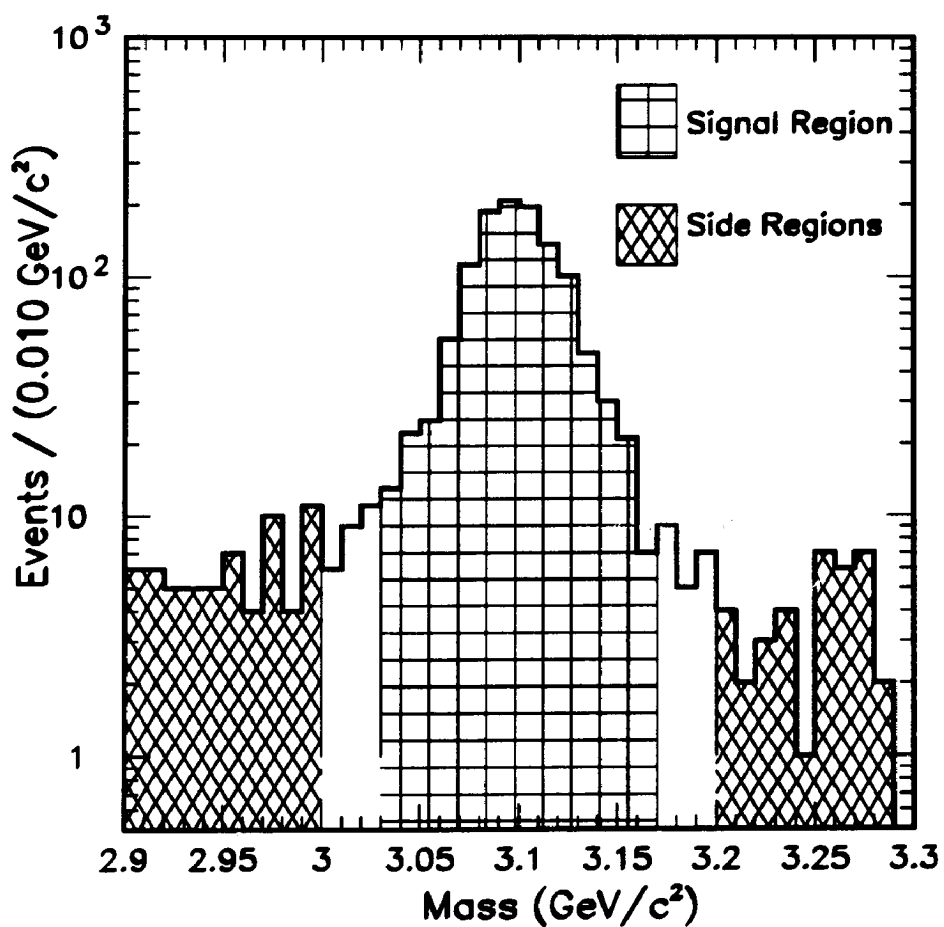


Figure 7.9:  $\mu^+\mu^-$  mass distribution observed in the data. The central shaded region is used in the search for  $B_u^- \rightarrow J/\psi + K^-$ . The shaded regions on the sides are used to estimate the effect of *fake*  $J/\psi$ 's.

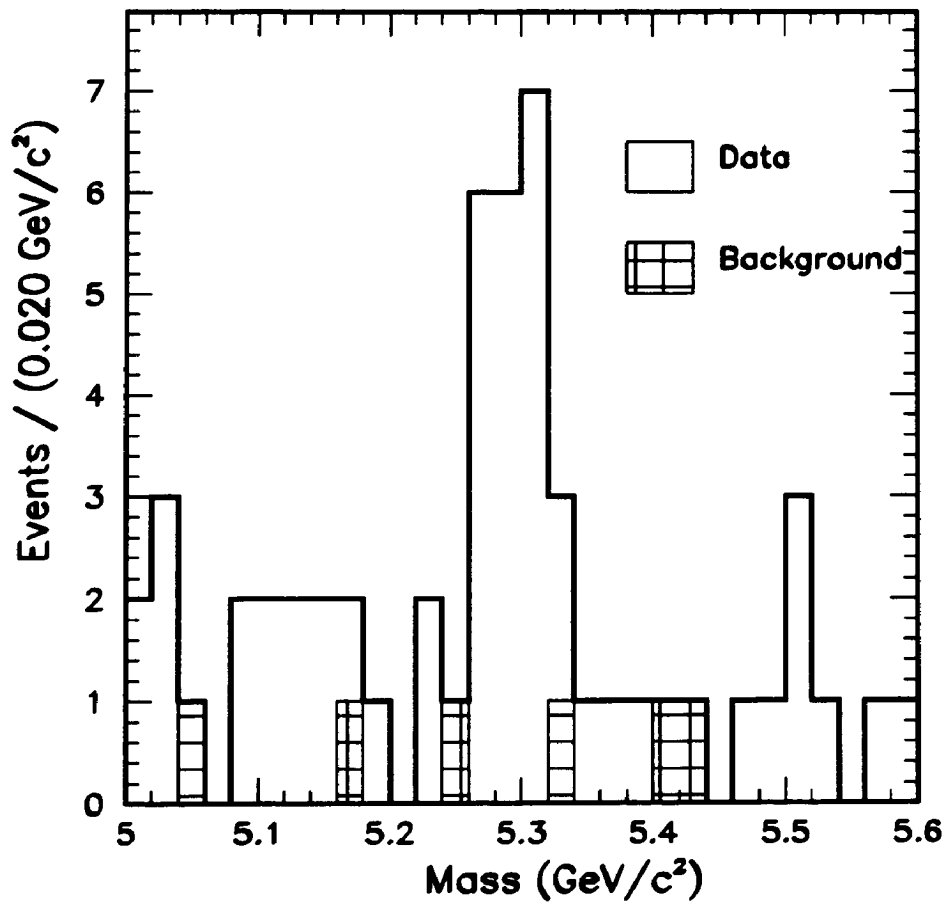


Figure 7.10: Background to the observed  $J/\psi K^-$  mass distribution from *fake*  $J/\psi$ 's.

which can be on the order of 20. These tracks could have originated in the fragmentation of the  $b$  quark into the  $B$  meson. Other possible sources are the decay products of the  $B$  meson which produced the  $J/\psi$ , or the decay products of the partner  $\bar{B}$  meson. If the tracks in question and the  $J/\psi$  come from the same parent  $B$  meson, then the mass of one of these tracks and the  $J/\psi$  will always be less than or equal to the  $B$  meson mass (taking into account the effects of momentum resolution). If the tracks in question come from fragmentation or from the partner  $\bar{B}$  meson, then the mass of one of these tracks and the  $J/\psi$  should have no correlation to the  $B$  mass. To determine the shape of this background, we used the following method. We took the momentum vector of a  $J/\psi$  passing all of our standard cuts from one event, and the momentum vectors of candidate kaons passing all of our standard cuts from another event, and formed the  $J/\psi + K^-$  mass. We show the results of this exercise in Figure 7.11, where we superimpose the true  $J/\psi + K^-$  signal. We see that this estimate seems to account for both the shape and the overall normalization of the background in the data fairly well.

## 7.5 Determining the Number of Observed $B_u^- \rightarrow J/\psi + K^-$ Events

### 7.5.1 Fit Procedure

The number of observed  $B^-$  mesons is determined by fitting the data in Figure 7.6. Since the number of events per bin is small, the fitting procedure we use is a Binned-

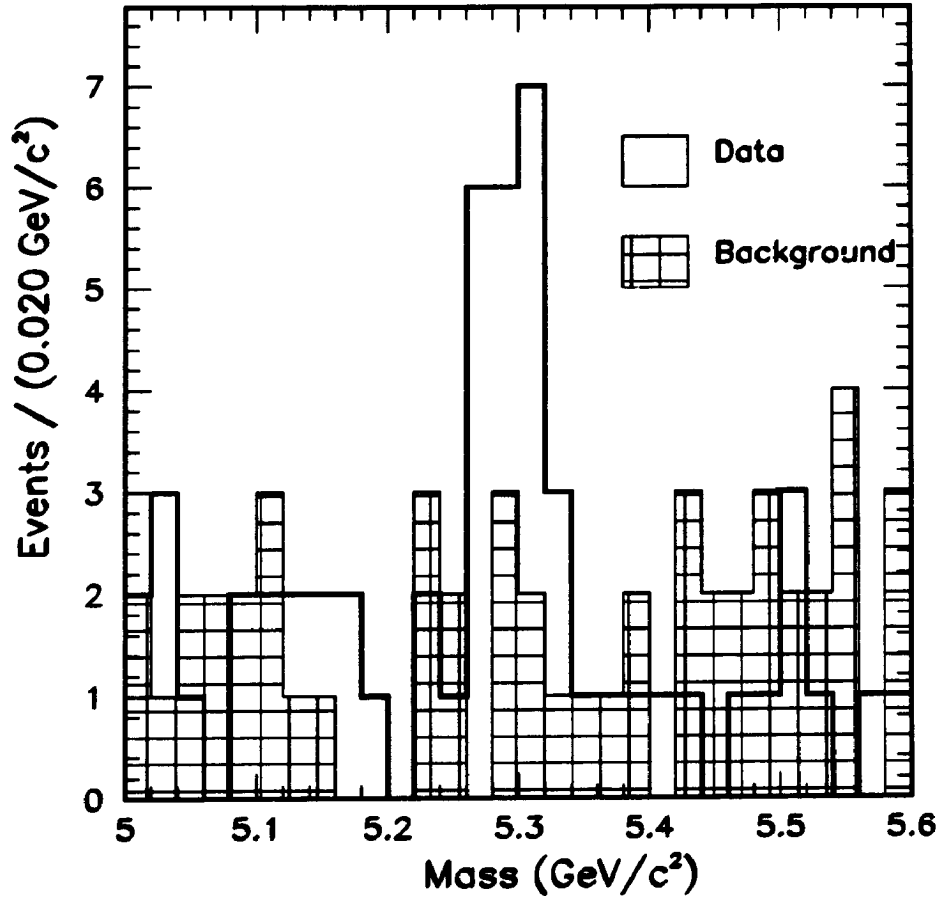


Figure 7.11: Background to the observed  $J/\psi K^-$  mass distribution from random tracks in the events.

**Maximum-likelihood method.** We use a Gaussian distribution to model the signal, and a linear function to describe the background (i.e. the data in the regions far from the peak). To briefly describe this method, note that the probability of observing  $n_i$  events in a given bin  $i$ , when one expects  $m_i$  events, is:

$$P_i = \frac{m_i^{n_i} e^{-m_i}}{n_i!}.$$

Given  $N$  bins in a histogram, the overall probability is then:

$$P_{total} = P_1 \times P_2 \times \dots \times P_N$$

Equivalently, one can consider the logarithm of the probability:

$$\log P = \sum_{i=1}^N \log P_i$$

$$\log P_i = n_i \log m_i - m_i - \log n_i!$$

and in fact this is the procedure adopted here. The expected number of events  $m_i$  in a given bin depend on the 5 parameters in the fit: the peak position, the width  $\sigma$ , and the the normalization of the Gaussian describing the signal, and the slope and intercept of the line describing the background. The values of these parameters are varied until the total probability of the fit is maximized. The variation is performed via the software package MINUIT.

### 7.5.2 Fit Results

To determine the number of events described by the Gaussian distribution, we must first decide whether the 2 parameters corresponding to the mean and width of the Gaussian should float (i.e. be free parameters) or not. If we allow both parameters to float, the fit returns the following values:

$$\text{Mean} = 5.295 \pm 0.007 \text{ GeV}/c^2$$

$$\sigma = 20 \pm 6 \text{ MeV}/c^2$$

where the errors shown are those which correspond to a change in the *log*-likelihood of 0.5 (this is approximately the same as a  $1\sigma$  change in a  $\chi^2$  fit). When comparing the mean to the world average  $B^-$  mass of  $5.2791 \pm 0.0019 \text{ GeV}/c^2$  [5, 4], one should also include the error in the mass scale of 0.1% (or  $0.005 \text{ GeV}/c^2$ ). Including this error, the observed mass is within 1.5 standard deviations of the world average. As will be discussed in the next chapter, the width we observe for the Gaussian is also approximately 1.5 standard deviations above that predicted by our Monte Carlo model. Since the number of fitted events is strongly correlated to the width of the Gaussian, we choose to fix the width to the Monte Carlo prediction of  $12 \text{ MeV}/c^2$ . This will lower the number of fitted events, but also lowers the effect of statistical fluctuations in bins near the peak.

The fit results in a mean of  $5.294 \pm 0.006(\text{fit}) \pm 0.005(\text{scale}) \text{ GeV}/c^2$  with  $14.1 \pm 4.3$  signal events. To determine the sensitivity of the number of events to the fit procedure,

Table 7.2: Results of fitting the observed  $B_u^- \rightarrow J/\psi + K^-$  sample.

Fit Method	Mass (GeV/c <sup>2</sup> )	Width (mv2)	Number
Floating Mass, Floating Width	$5.295 \pm 0.007$	$20 \pm 6$	$17.2 \pm 5.1$
Fixing Mass, Fixing Width	5.279	12	$11.2 \pm 4.1$
Floating Mass, Fixing Width	$5.295 \pm 0.006$	$20 \pm 6$	$14.1 \pm 4.3$
Fixing Mass, Floating Width	5.279	$26 \pm 7$	$16.9 \pm 5.3$

we list in Table 7.2 the results of varying the fit procedure by alternately fixing and floating the width and mean of the Gaussian we use to describe the signal. One can see that the variation in the number of events about the value returned by the chosen fit procedure is approximately 20%. In Figure 7.12 we show the four fit results.



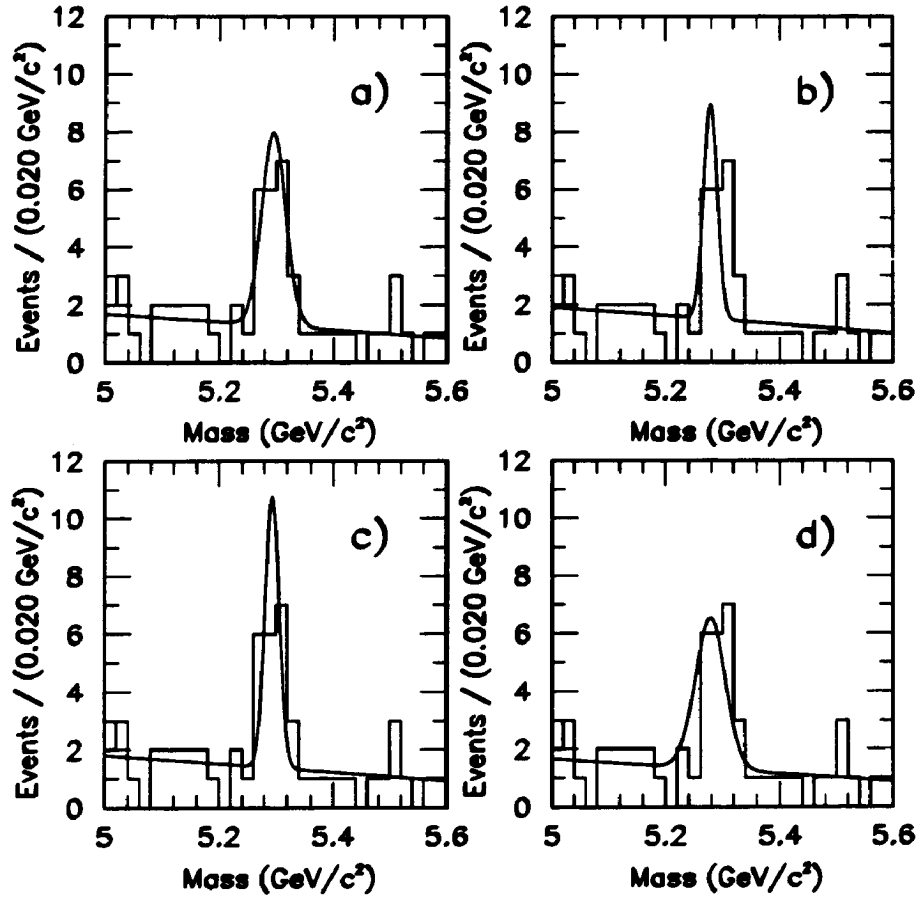


Figure 7.12: Fitting the observed  $B_u^- \rightarrow J/\psi + K^-$  sample. For all figures the histogram is the data, the curve is the fit. In Figure (a) the mass and width are floated, in (b) the mass and width are fixed, in (c) the mass is floated, the width is fixed, and in (d) the mass is fixed, the width is floated.

## Chapter 8

### Measuring the Cross Sections

#### 8.1 Method

Our measurement of the  $b$  quark and  $B_u^-$  meson cross sections is based on the  $B_u^- \rightarrow J/\psi + K^-$  sample described in the previous chapter. In order to determine the cross section, we need to know the efficiency for reconstructing the process  $b \rightarrow B_u^- \rightarrow J/\psi + K^-$ , followed by  $J/\psi \rightarrow \mu^+ \mu^-$ . To do this we use a Monte Carlo model which incorporates the  $b$  quark generation and fragmentation, a simulation of the CDF geometry and trigger, and a model of the offline reconstruction process.

##### 8.1.1 Monte Carlo Generation

The origin of our observed signal in the channel  $B_u^- \rightarrow J/\psi + K^-$  is assumed to be the production of  $b$  quarks and their subsequent fragmentation into  $B^-$  mesons. As mentioned previously, we use the Nason, Dawson, and Ellis (NDE) forms for the  $P_T$  and rapidity distributions for  $b$ -quark production. The justifications for using this

calculation are twofold. First of all, it is the latest QCD perturbative calculation, and the  $b$  quark is thought to be heavy enough that a perturbative expansion in  $\alpha_s$  is proper. Secondly, the  $b$  quark  $P_T$  spectrum has been measured at UA1[51], and both the shape and overall normalization agree with NDE at  $\sqrt{s} = 630 \text{ GeV}/c^2$ . The UA1 measurement is shown in Figure 8.1.

The calculated  $b$ -quark  $P_T$  distribution at  $\sqrt{s} = 1.8 \text{ TeV}/c^2$  was shown in Figure 2.4. The central (solid dotted) curve is incorporated into our Monte Carlo model. Since we use the Monte Carlo model to determine our efficiency only, we are not sensitive to the overall normalization associated with the NDE calculation. The rapidity distribution is shown in Figure 8.2. Here we also show the dependence of the rapidity spectrum on the  $P_T$  of the  $b$  quark. This effect is incorporated into the Monte Carlo model also.

One might ask what effect the theoretical errors on the  $P_T$  shape have on our analysis. We can get an idea of this effect by parameterizing the  $P_T$  spectrum with the form:

$$\frac{d\sigma}{dP_t} = \frac{A}{(P_t^2 + m_b^2)^n}$$

where  $m_b = 5.0 \text{ GeV}/c^2$ ,  $A$  is used to set the overall normalization, and  $n$  is a free parameter. Fitting the theoretical curve over the region  $7.0 \leq P_t \leq 40.0$  results in the value  $n = 3.01$ . The fit result is shown in Figure 8.3. To determine the effect of changing the slope of the  $P_T$  spectrum we chose two other values for  $n$ ;  $n = 2.63$

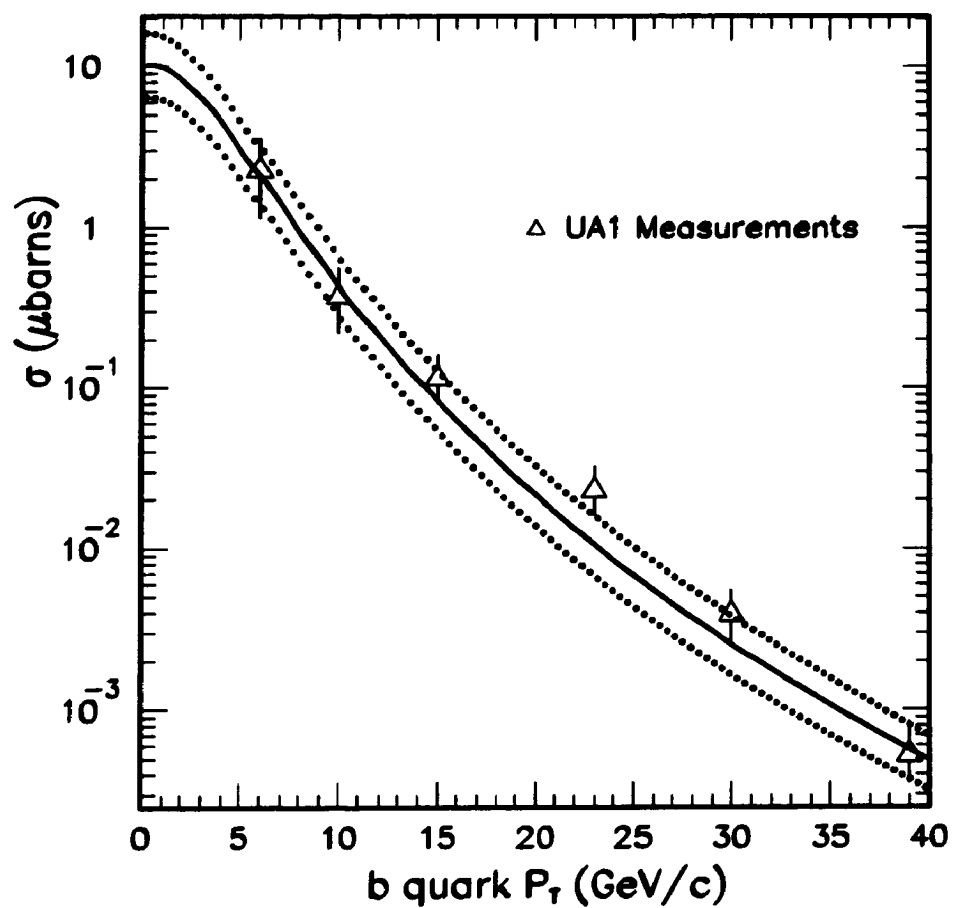


Figure 8.1: UA1 measurement of the  $b$  quark cross section.

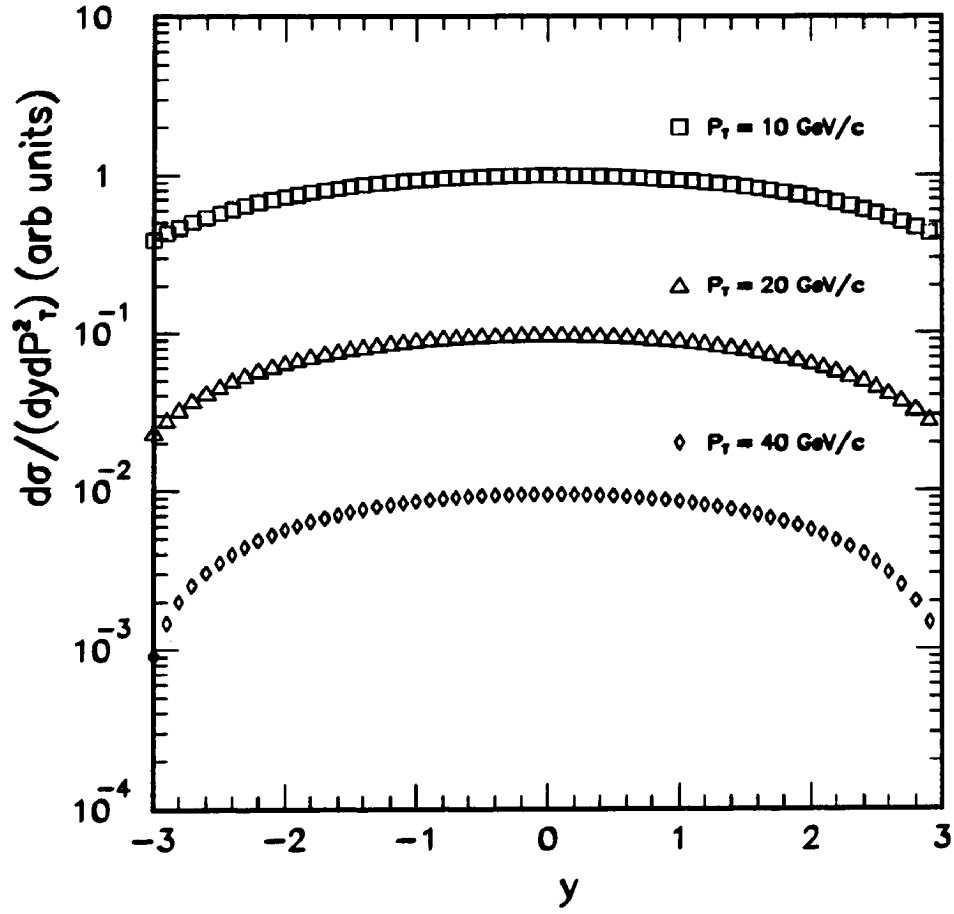


Figure 8.2: The calculated  $b$ -quark rapidity spectrum.

and  $n = 3.42$ . These two choices are shown superimposed on the theoretical curve in Figure 8.4. (In fact, these last two values for  $n$  were chosen because they cover the region between the upper and lower error curves in Figure 8.4, in the  $P_T$  range of interest.) In Figure 8.5 we show the relative efficiency for reconstructing  $b$  mesons as a function of  $n$ , where 1.0 on the efficiency axis corresponds to  $n = 3.01$  (i.e. the default NDE  $P_T$  shape). We conclude that the assumed shape of NDE contributes an  $\sim 10\%$  systematic error.

As mentioned in section 2.3, we model energy sharing between the quark and meson with the Peterson parameterization. The experimentally observed value [19] for the fragmentation parameter is:

$$\epsilon_b = 0.006 \pm 0.002.$$

By varying this parameter in our model within the experimental uncertainty, we observe a 7% variation in the acceptance.

In the decay  $B_u^- \rightarrow J/\psi + K^-$ , the  $J/\psi$  and  $K^-$  are produced in a  $\ell = 1$  state and the  $J/\psi$  is polarized such that its spin is perpendicular to its momentum vector, as measured in the rest frame of the decaying  $B^-$  meson. This results in a  $\sin^2 \theta$  angular distribution for the decay muons with respect to the  $J/\psi$  direction in the rest frame of the  $B$  meson. This effect is incorporated into our Monte Carlo model.

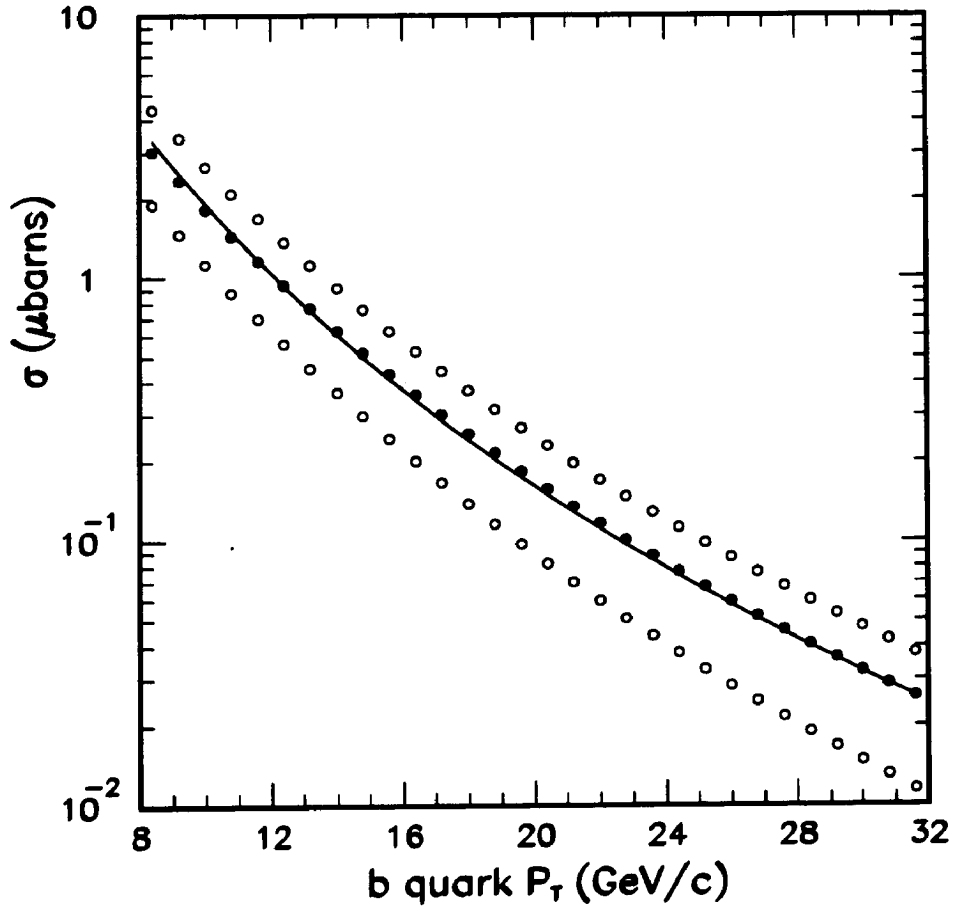


Figure 8.3: The calculated cross section overlayed with the fit curve described in the text. For the fit curve,  $n = 3.01$ .

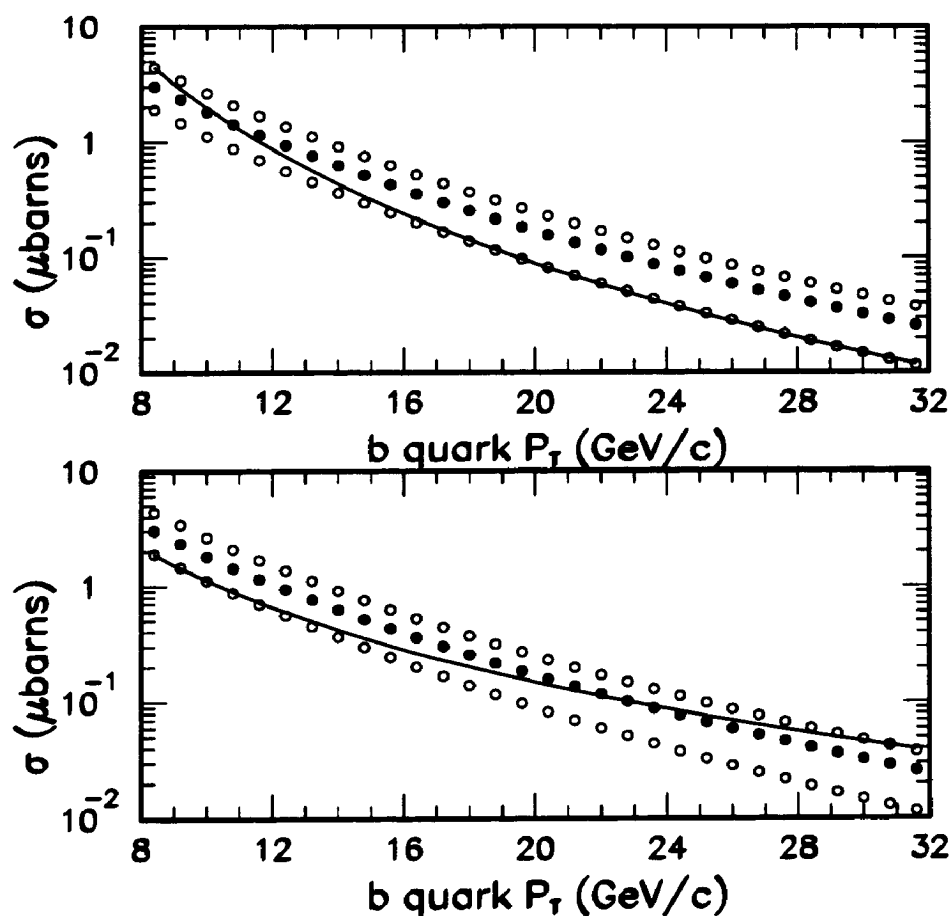


Figure 8.4: The calculated cross section overlaid with the fit curves described in the text. The fit curve in (a) is described by the parameter  $n = 3.42$ . The fit curve in (b) is described by the parameter  $n = 2.63$ .



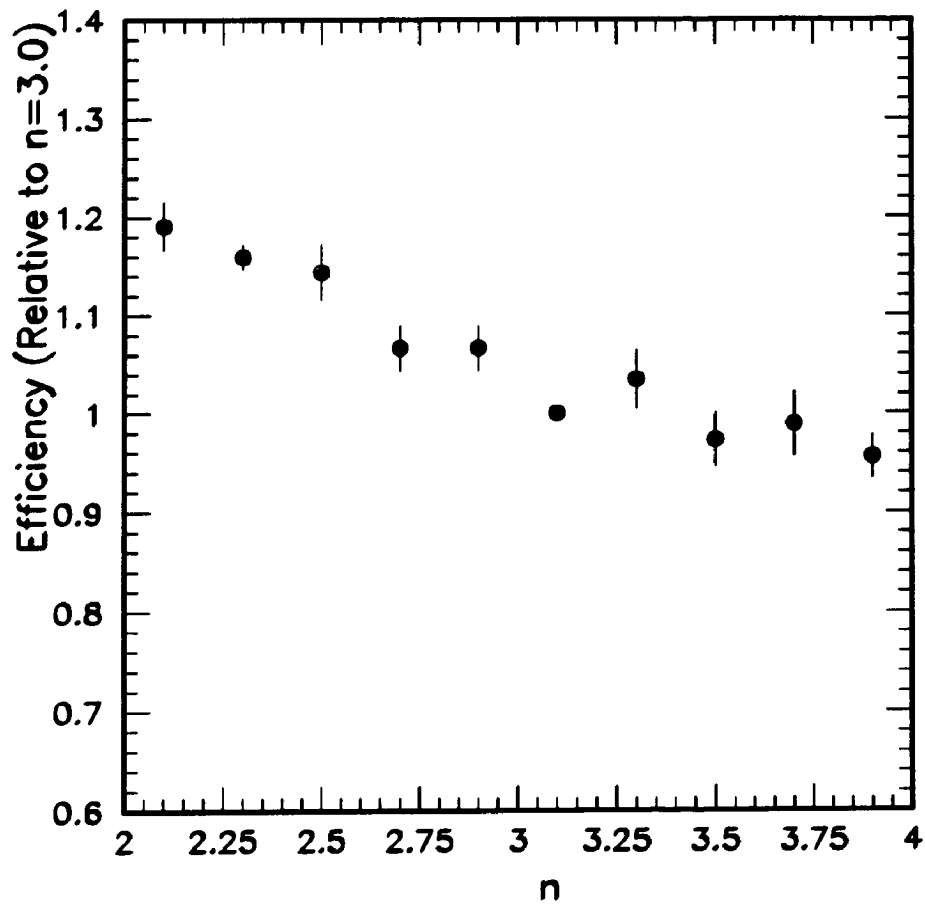


Figure 8.5: Reconstruction efficiency as a function of the fit parameter  $n$  described in the text. The error bars are binomial.

### 8.1.2 Trigger Model

Parameterizations of both the Level-1 and Level-2 trigger efficiencies as functions of muon  $P_T$  were used in the simulation. These were discussed in detail in Chapter 5. The uncertainty associated with the Level-2 trigger for muons with  $P_T \leq 2.0$  GeV/c, and the rapid rise in efficiency in the region from 2.0 GeV/c to 3.0 GeV/c require that both muons have  $P_T \geq 3.0$  GeV/c. The variations in the trigger parameterizations lead to a systematic variation in the acceptance of 12% for events with both muons having  $P_T > 3.0$  GeV/c.

### 8.1.3 Detector Model

The detector model we use incorporates the geometry and material construction of the CDF detector. In most cases, detailed aspects of detector performance have been tuned to reproduce measurements made using the data.

The CTC position resolution and wire efficiency used in our Monte Carlo model were tuned to that observed in Figure 6.1 for the data. To then compare how well the simulation models the performance of the tracking algorithm in the data, we compare the *calculated* error on the track parameters, shown in Figures 8.6 and 8.7. The good agreement between data and Monte Carlo model evident in these plots indicates that the CTC is modeled very well. These effects will become important when we wish to predict the expected resolution on both the  $J/\psi$  and the reconstructed  $B$

meson sample.

As noted in Figure 6.2, the dependence of the efficiency of the tracking algorithm on the  $P_T$  of the track is very small. However, as noted in Figure 6.3, the efficiency has a significant dependence on  $\eta$ . In Figure 8.8 we show the muon and kaon  $\eta$  distributions after all cuts. Convoluting these distributions with the above efficiency distribution results in a tracking efficiency of  $(97 \pm 2)\%$  for each muon. The broader  $\eta$  spectrum of the kaons results in a slightly lower efficiency of  $(94 \pm 2)\%$ . The overall tracking efficiency is then  $(89 \pm 4)\%$ . Based on this study, we assign a systematic error of 5% due to the track reconstruction algorithm.

An additional effect entering into the tracking efficiency concerns  $K^-$  decays.  $c\tau = 371$  cm for the charged kaon, and the simulation predicts 7% of the kaons with  $P_T \geq 2.0$  GeV/c decay before exiting the CTC. In Figure 8.9 we show the decay radius of kaons with  $P_T \geq 2.0$  GeV/c. Since the mass of the kaon is comparable to the  $P_T$  of the kaon sample we are considering, a decay inside the active volume of the CTC may show up as a kink (change in direction) along the path of the charged track, resulting in poorer track reconstruction efficiency. Approximately half of these events (with the  $K^-$  decaying inside the CTC) are successfully reconstructed as  $B^-$  decays. It is difficult to determine how well the Monte Carlo models the tracking efficiency for these decays. Since the number of decays forms a relatively small fraction of our sample, we will assume the track reconstruction efficiency predicted by the Monte

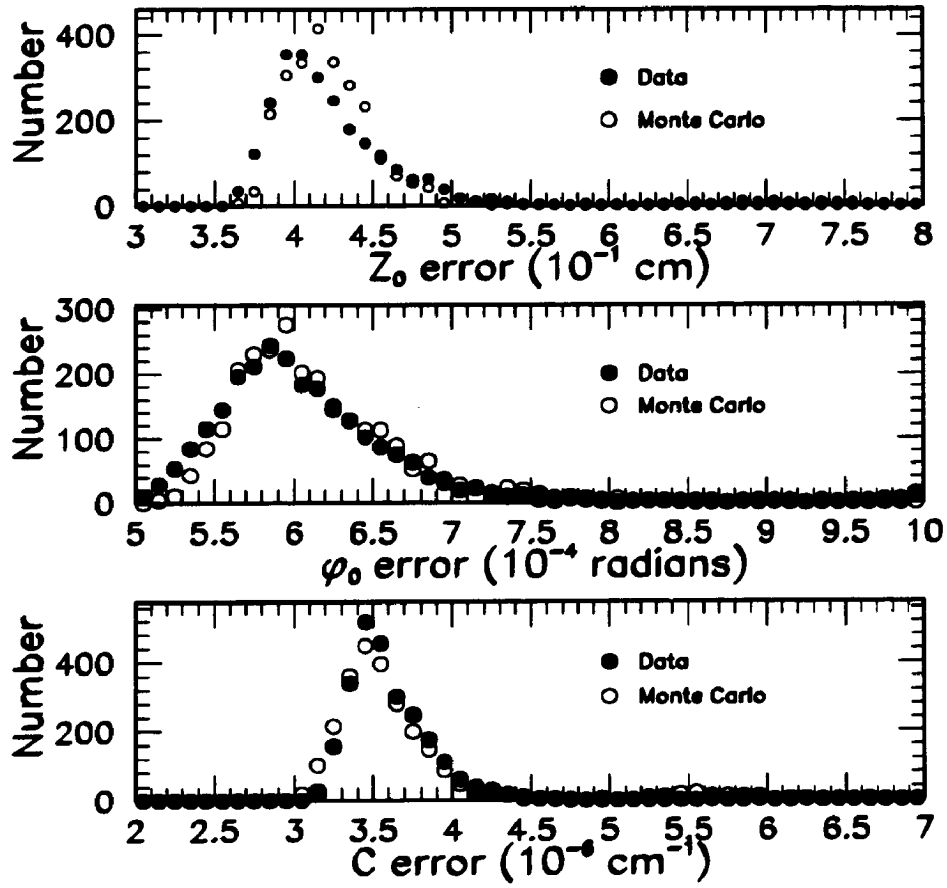


Figure 8.6: The calculated error on the track parameters  $Z_0$ ,  $\phi_0$ , and  $c$ ; Monte Carlo vs data.

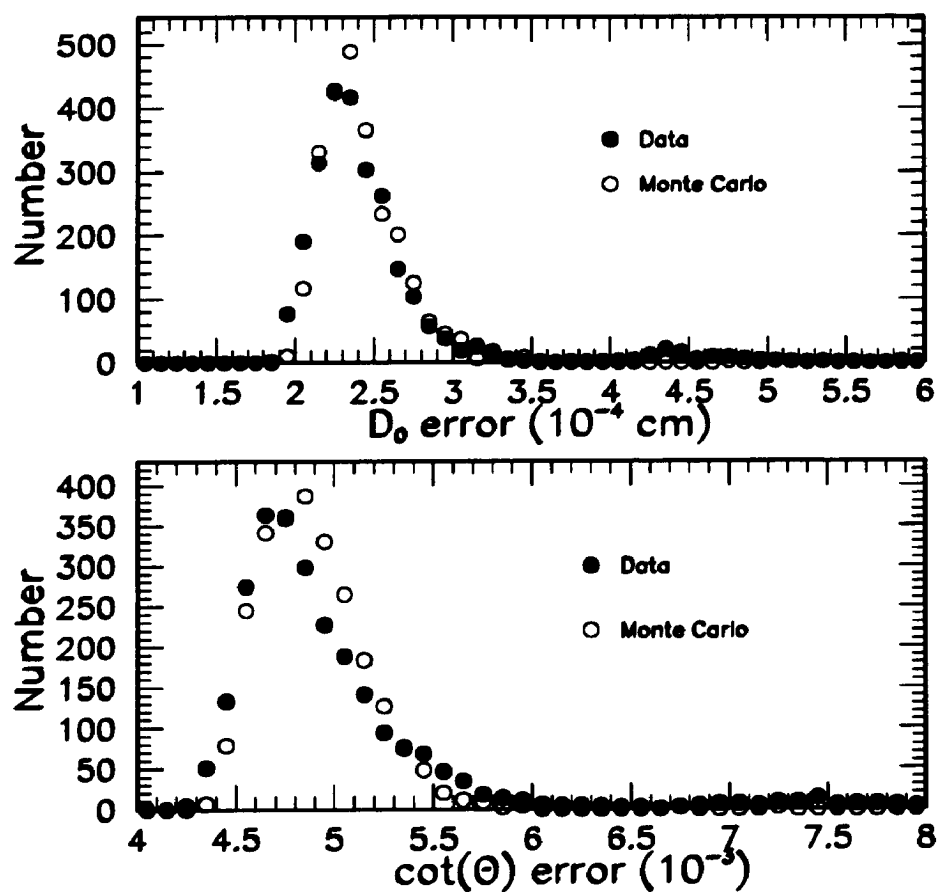


Figure 8.7: The calculated error on the track parameters  $D_0$  and  $\cot \theta$ ; Monte Carlo vs data.

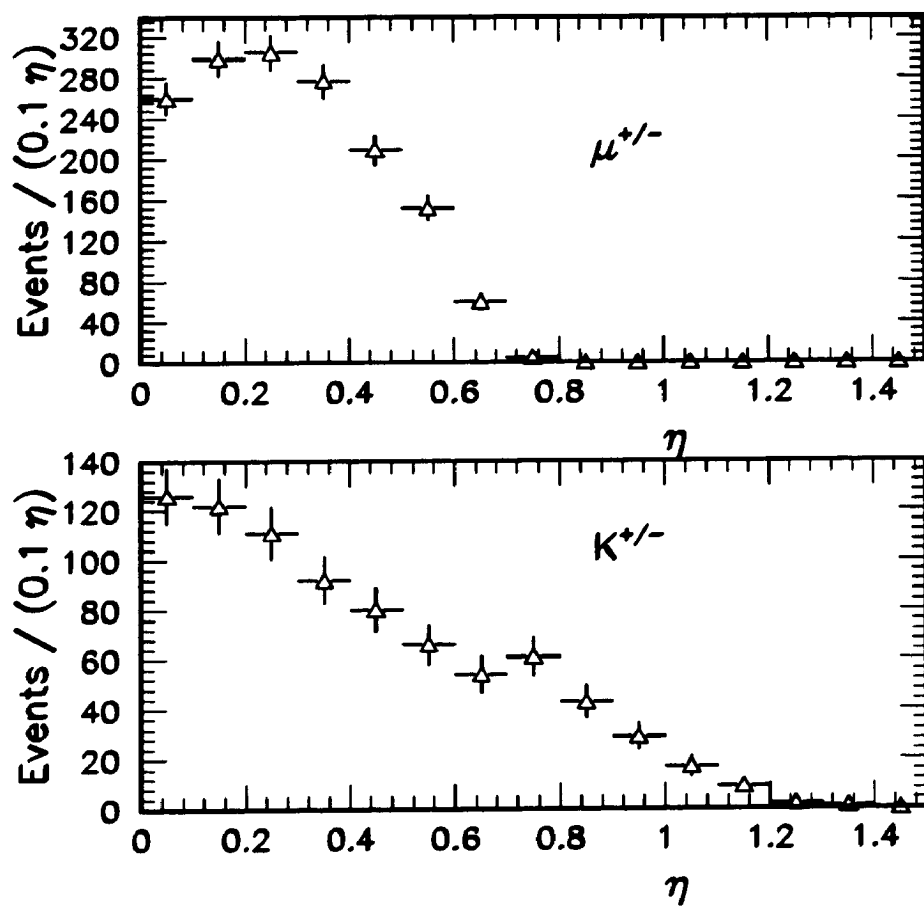


Figure 8.8: Detector rapidity spectra for muons and kaons as predicted by the Monte Carlo model. The error bars are statistical.

Carlo. We assign a 4% systematic due to kaon decays inside the CTC.

The CMU position resolution and wire efficiency used in our Monte Carlo model were tuned to that observed in the data, shown in Figures 6.4 and 6.5. To then compare how well the simulation models the performance of the CMU tracking algorithm in the data, we compare the fit quality in both the  $xy$  and  $zy$  directions, shown in Figure 8.10. One can see that the fit quality observed in the data is well reproduced in the Monte Carlo model. In addition, in Figure 8.11, we compare the distributions obtained in the Monte Carlo model for the CMU-CTC matching variables with that observed in our Cosmic Ray muon sample. Once again, there is good agreement between Monte Carlo model and data.

As discussed in Sections 5.4 and 5.5, the single muon efficiency of the CMU reconstruction algorithm is  $(96.7 \pm 0.7)\%$ , which includes the CMU reconstruction efficiency, the CMU-CTC link efficiency, and the CMU-CTC link quality cut efficiency. Assuming the reconstruction efficiencies for both muons are independent, the overall CMU efficiency is  $(93.6 \pm 1.0)\%$ .

Finally, the simulation models the muon chamber geometry, (including cracks between the  $\phi$  wedges and the crack between the two sides in  $\eta$ ). The presence of the cracks in the chamber can be demonstrated by extrapolating the muon CTC track to the radius of the muon chambers. The cracks will appear as dips in plots of the  $\phi$  and  $\eta$  of the extrapolated track. This is shown in Figure 8.12, for both the data and

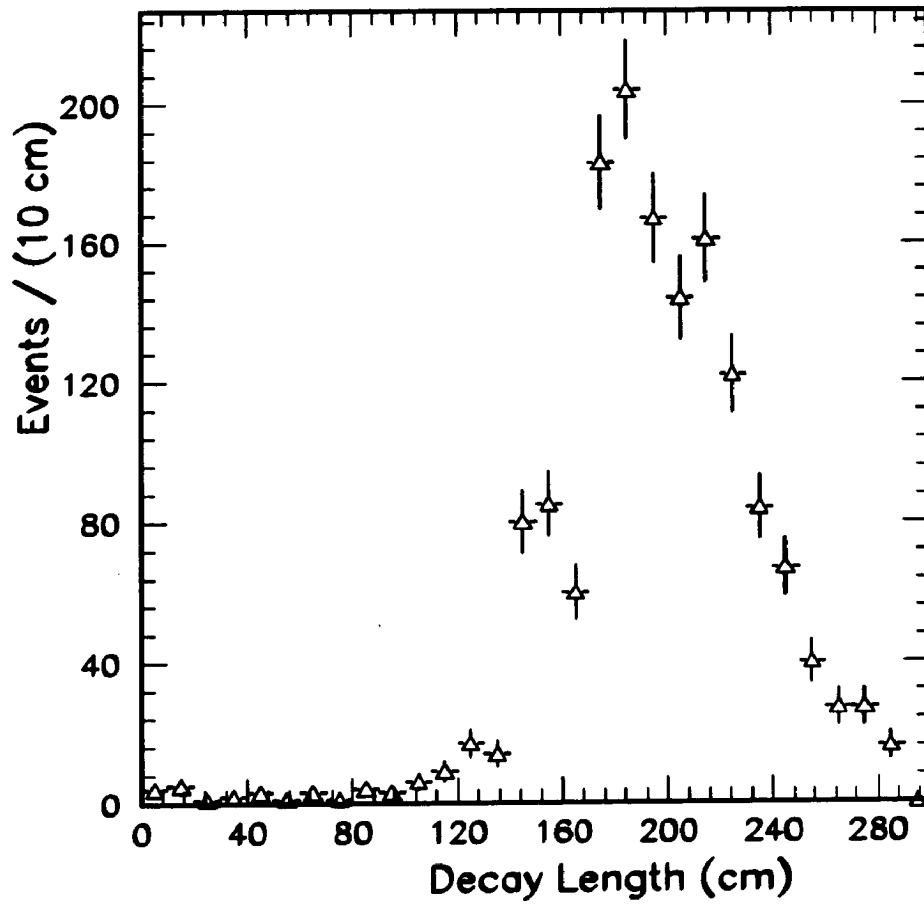


Figure 8.9: Decay radius of kaons with  $P_T \geq 2.0$  GeV/c , as predicted by the Monte Carlo model. The error bars are statistical.



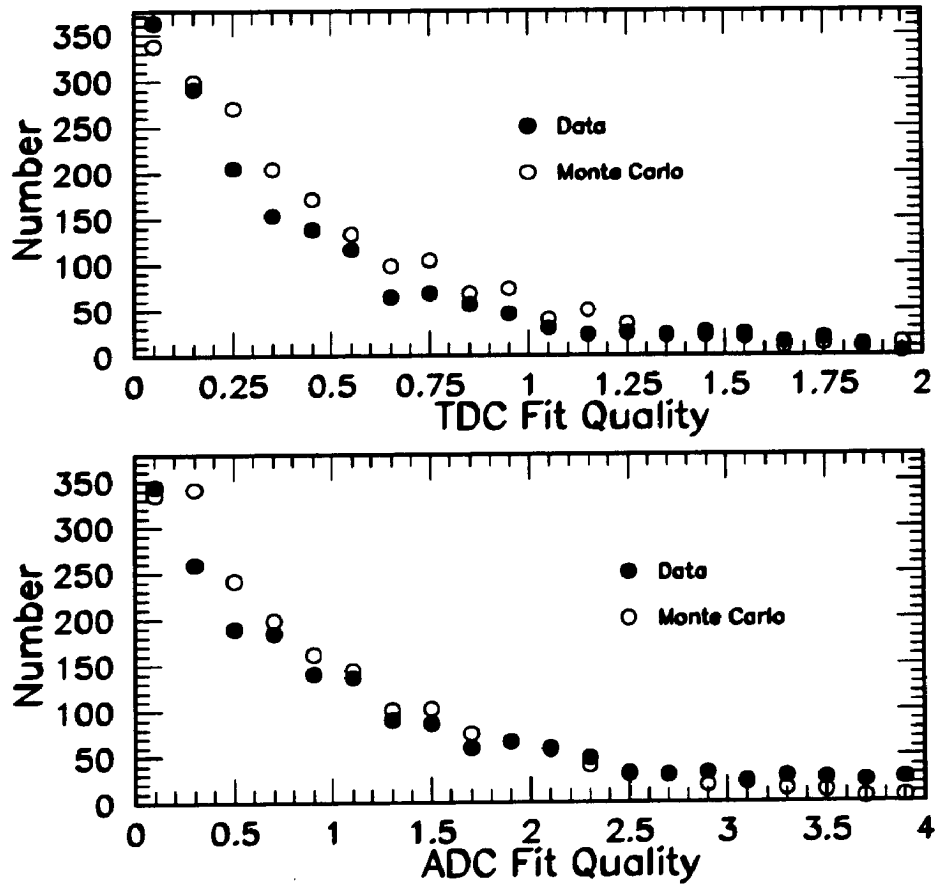


Figure 8.10: Comparison of the fit quality of the CMU track reconstruction observed in the data with that seen in the Monte Carlo model. The top curve is the fit quality in the  $xy$  plane and the bottom is the fit quality in the  $zy$  plane.

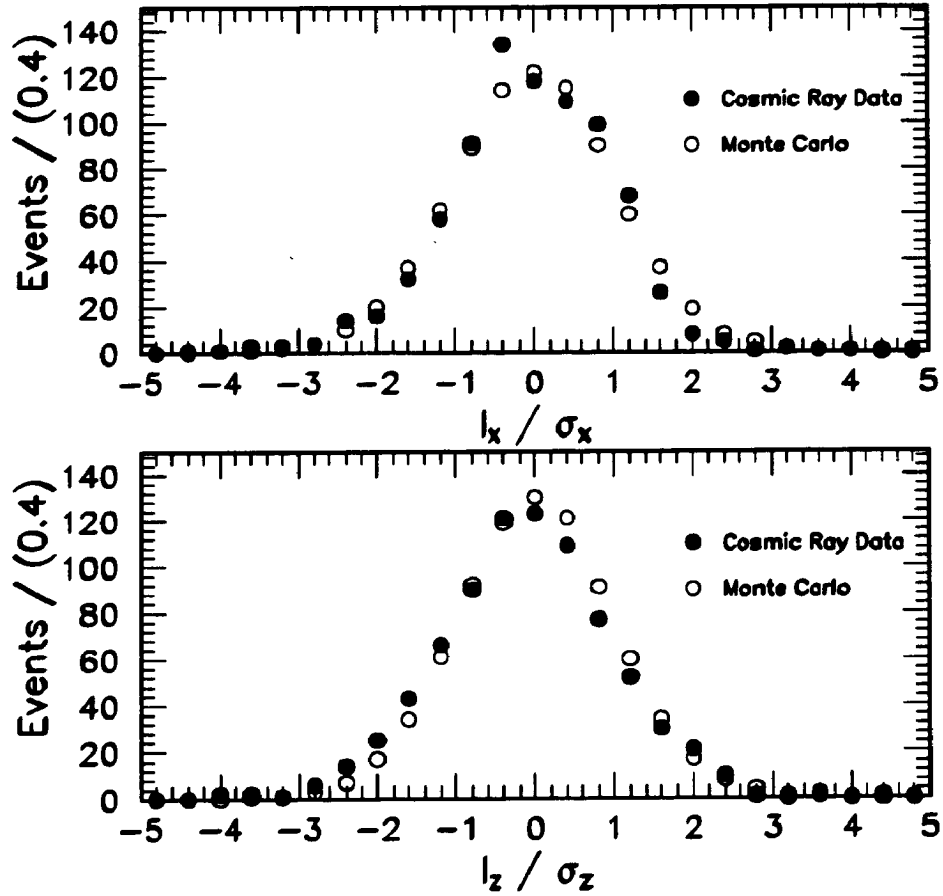


Figure 8.11: Comparison of the normalized matching variables observed in the data with that seen in the Monte Carlo model. The top curve is the normalized  $x$ -intercept match,  $(I_x/\sigma_x)$ , and the bottom curve is the normalized  $z$ -intercept match,  $(I_z/\sigma_z)$ .

Table 8.1: Reconstruction Efficiencies and systematic errors.

Effect	Efficiency (%)	Systematic (%)
CTC Tracking	89	5
Kaon Decays	96	4
CMU Tracking	94	1
Overall	80	7

the Monte Carlo model. The muon fiducial volume covers 85% of the solid angle in the region  $|\eta| < 0.65$ .

In Table 8.1 we show the overall efficiency and systematic error associated with offline reconstruction effects. Our final reconstruction efficiency is  $(80 \pm 6)\%$ , assuming both muons are within the fiducial acceptance of the CMU and have  $P_T \geq 3.0 \text{ GeV}/c$ , and that the  $K^-$  has  $P_T \geq 2.0 \text{ GeV}/c$ .

#### 8.1.4 Comparison of Data with the Monte Carlo Model

In this section we determine how adequately our Monte Carlo model describes our observed data sample. The first test examines the observed width of both the  $J/\psi$  and the  $B$ -meson sample. The values predicted by Monte Carlo model and those observed in data are detailed in Table 8.2. One can see that in both cases the data values are approximately one standard deviation high.

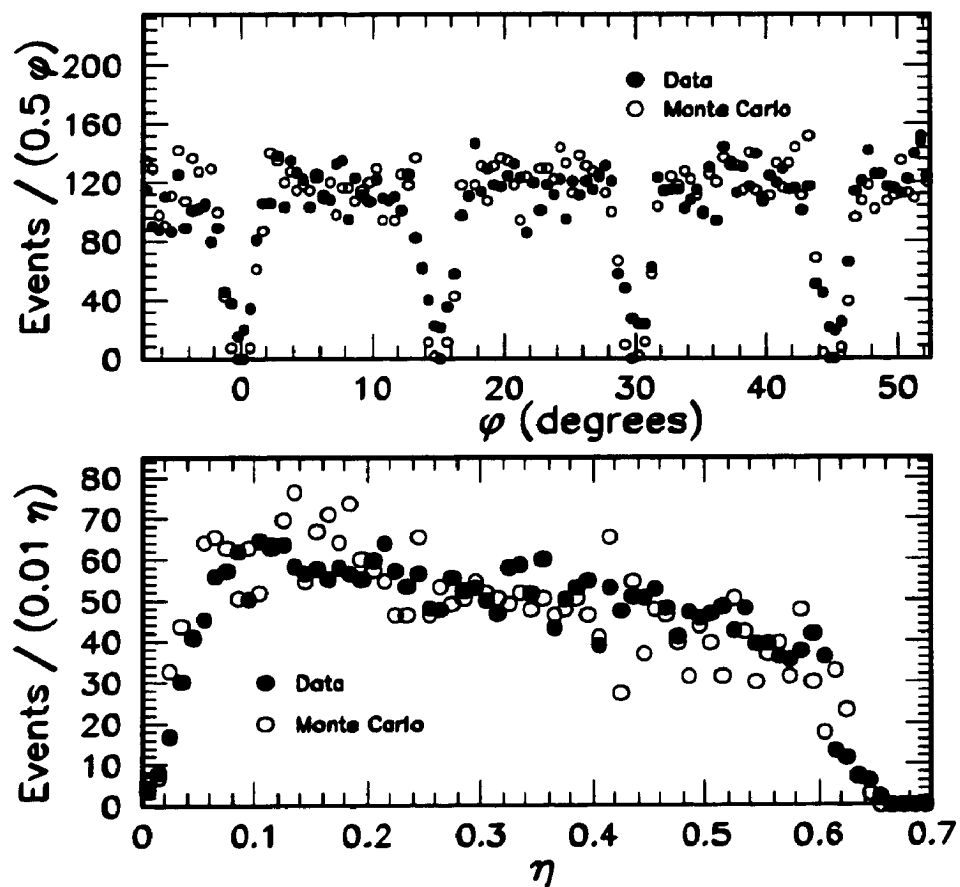


Figure 8.12: Mapping the cracks in the muon chambers, comparison of the Monte Carlo model *vs* data.

Table 8.2: Widths observed in the data compared with Monte Carlo.

Sample	Data (MeV/c)	Monte Carlo (MeV/c)
$J/\psi \rightarrow \mu^+ \mu^-$	$21 \pm 1$	$19 \pm 1$
$B_u^- \rightarrow J/\psi + K^-$	$20 \pm 6$	$12 \pm 1$

Another test of the Monte Carlo model can be accomplished by examining the  $B^-$  and  $K^-$   $P_T$  distributions. However, the signal we observe is approximately 15 events above a background of approximately 5 events, so in order to compare the data with the Monte Carlo model (which contains no background), we must subtract out the background. The background subtraction procedure we use is described by the following:

- We define our signal region as the mass range  $5.26 - 5.34 \text{ GeV}/c^2$ .
- We define two background regions as the mass ranges  $5.16 - 5.24 \text{ GeV}/c^2$  and  $5.36 - 5.44 \text{ GeV}/c^2$ .
- We plot the  $K^-$   $P_T$  for the events found in the signal region in  $1.0 \text{ GeV}/c$  bins in a histogram.
- We plot the  $K^-$   $P_T$  for the events found in the background region in  $1.0 \text{ GeV}/c$  bins in a separate histogram. Since the background shape is not rapidly changing, we assume the non-resonant (i.e. non  $B^-$  meson) contribution to the

signal region can be approximated by the two background regions. We then divide the background histogram bin contents by 2, and subtract the resultant histogram bin-by-bin from the signal histogram.

The result of this procedure applied to the  $K^- P_T$  spectrum is shown in Figure 8.13, where we overlay the Monte Carlo prediction for the  $P_T$  spectrum. The Monte Carlo prediction has been normalized to the number of signal events present after background subtraction. In Figure 8.14 we show the corresponding distributions for the  $B^-$  meson  $P_T$  distributions where a similar background subtraction has been done for the data. Finally, in Figure 8.15, we show the  $B^-$  meson rapidity distributions. Although there is qualitative agreement between data and Monte Carlo, the lack of statistics in the data does not allow a quantitative comparison.

## 8.2 The $b$ quark Cross Section

A  $b$  quark can fragment into  $B^-$ ,  $\bar{B}^0$ ,  $\bar{B}_s^0$  mesons, or a variety of  $b$  flavored baryons. To extract the  $b$ -quark cross section, we make the assumption described in Section 2.3, that  $B^-$ ,  $\bar{B}^0$ ,  $\bar{B}_s^0$ , and  $b$  baryons are produced in the ratio 0.375 : 0.375 : 0.15 : 0.10. This assumption that  $F_{b \rightarrow B^-} = 0.375$  then enters directly into our cross section calculation.

Since the  $b$  quark is not observed directly, we quote the cross section for  $b$  quarks with  $P_T > P_T^{min}$  where  $P_T^{min}$  is defined as that  $b$  quark  $P_T$  such that 90% of our final

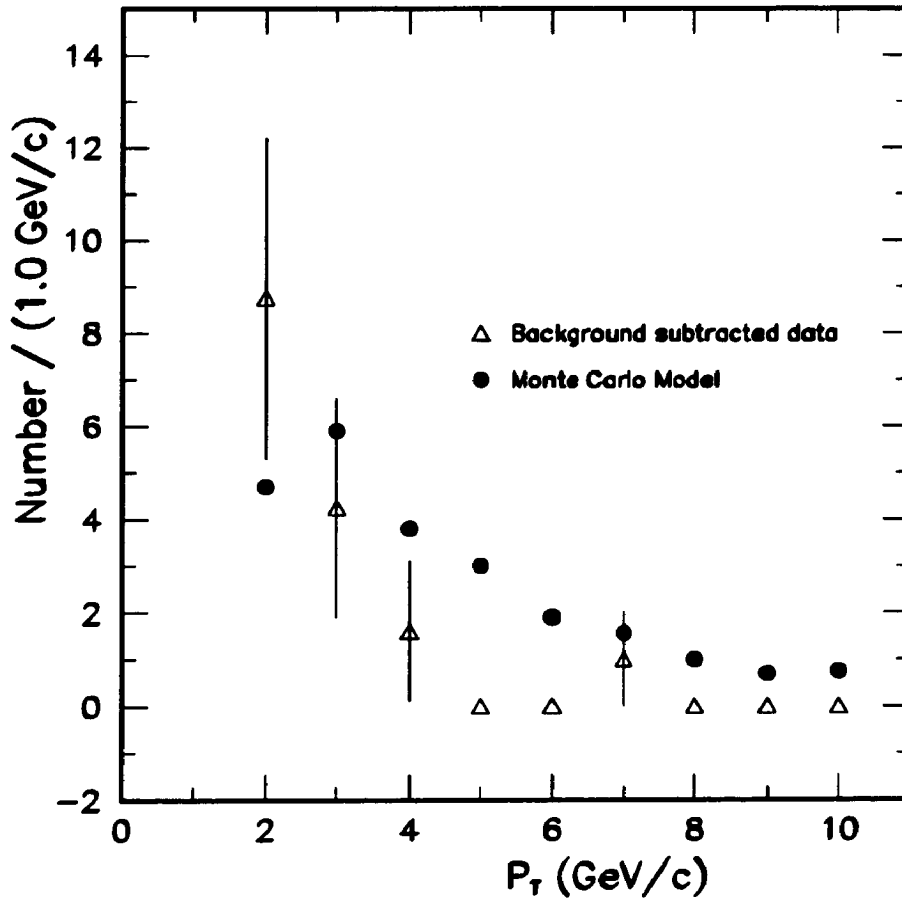


Figure 8.13: Comparison of the  $K^-$   $p_T$  spectrum observed in the data with the Monte Carlo prediction. The error bars are the statistical errors of both the data and the background added in quadrature.

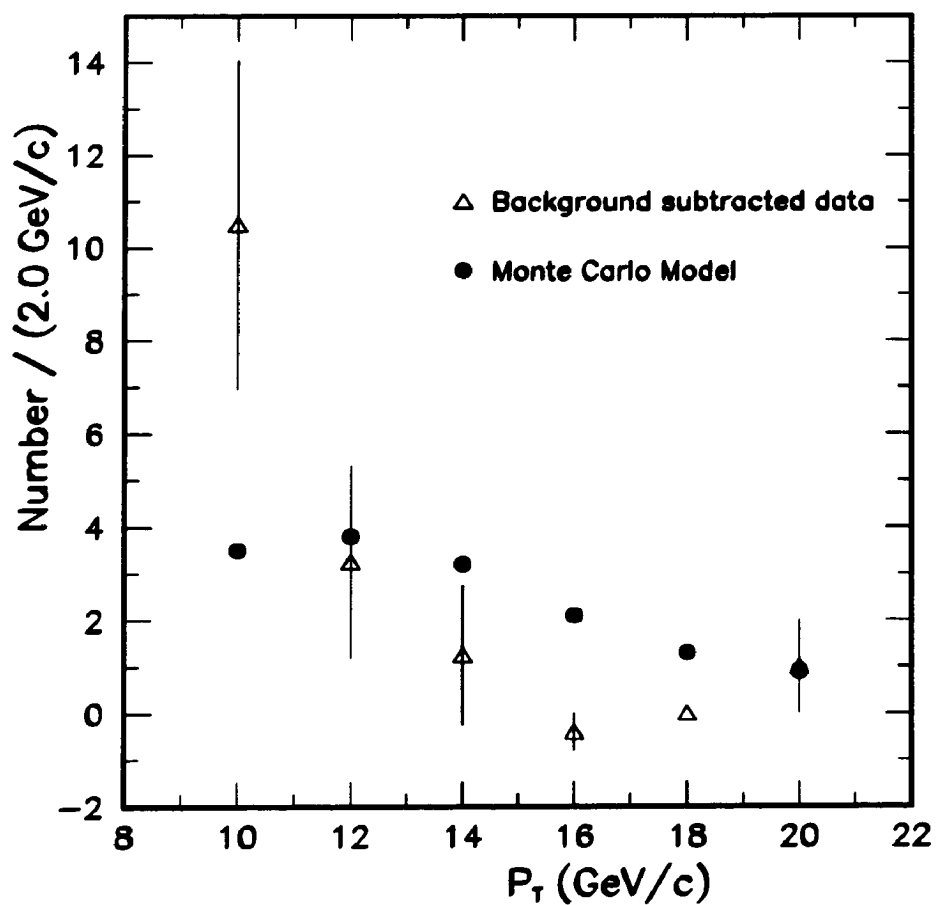


Figure 8.14: Comparison of the  $B^-$  meson  $P_T$  spectrum observed in the data with the Monte Carlo prediction. The error bars are the statistical errors of both the data and the background added in quadrature.



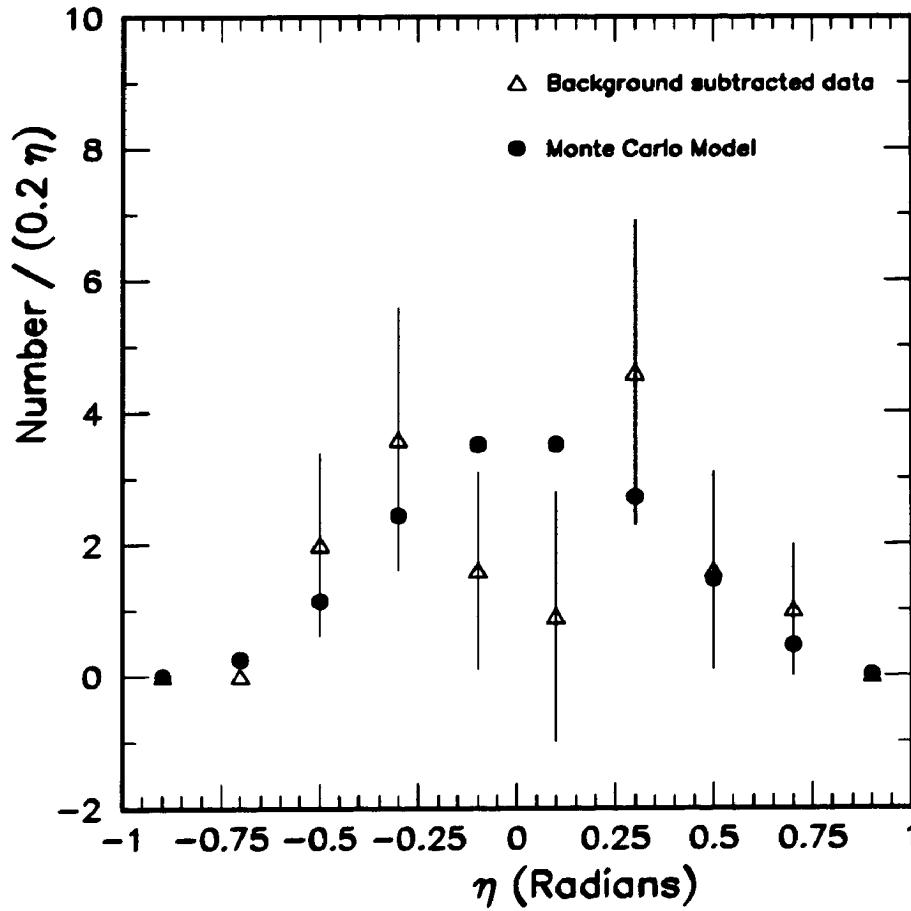


Figure 8.15: Comparison of the  $B^-$  meson rapidity spectrum observed in the data with the Monte Carlo prediction. The error bars are the statistical errors of both the data and the background added in quadrature.

sample of reconstructed  $B^-$  mesons come from  $b$  quarks with  $P_T > P_T^{min}$ . This definition of  $P_T^{min}$  is illustrated in Figure 8.16. Using the Monte Carlo model described above, we find that  $P_T^{min} = 11.5 \text{ GeV}/c$ .

As figure 8.15 shows, the rapidity of our observed  $B_u^- \rightarrow J/\psi + K^-$  sample is  $\leq 0.7$ . The reason for this is that we trigger on the two muons from the  $J/\psi$  decay, and the CMU system is confined to *pseudorapidity* (which is a close approximation to rapidity in the case of the muons)  $\leq 0.65$ . This will effect the rapidity distribution of the  $b$  quarks which contribute to our observed sample. This is shown in Figure 8.17, where it is apparent that our acceptance for  $b$  quarks is limited to  $|y| \leq 0.7$ . Since the theoretical calculation is for  $b$  quarks with rapidity  $\leq 1.0$ , we use our Monte Carlo model to correct our rapidity acceptance out to  $|y| = 1$ .

We then define our efficiency as:

$$\epsilon_b = \frac{N_B^{rec}}{N_b^{gen} \text{ with } P_{Tb} \geq P_T^{min} \text{ and } |y_b| \leq 1.0}$$

where  $N_B^{rec}$  refers to the number of  $B$  mesons passing all of the same analysis cuts as in the data, and  $N_b^{gen}$  refers to the number of  $b$  quarks generated. The generation of the Monte Carlo  $b$  quark sample was for  $b$  quarks with  $P_T \geq 7.0 \text{ GeV}/c$  (i.e well below  $P_T^{min}$ ), and  $|y_b| \leq 1.0$ . Our Monte Carlo model predicts that the efficiency  $\epsilon_b$  for the decay chain  $b \rightarrow B^- \rightarrow J/\psi + K^-$ ,  $J/\psi \rightarrow \mu^+ \mu^-$  is  $(2.27 \pm 0.45)\%$ . where the error represents the sum in quadrature of the systematic effects due to offline reconstruction and the trigger parameterization.

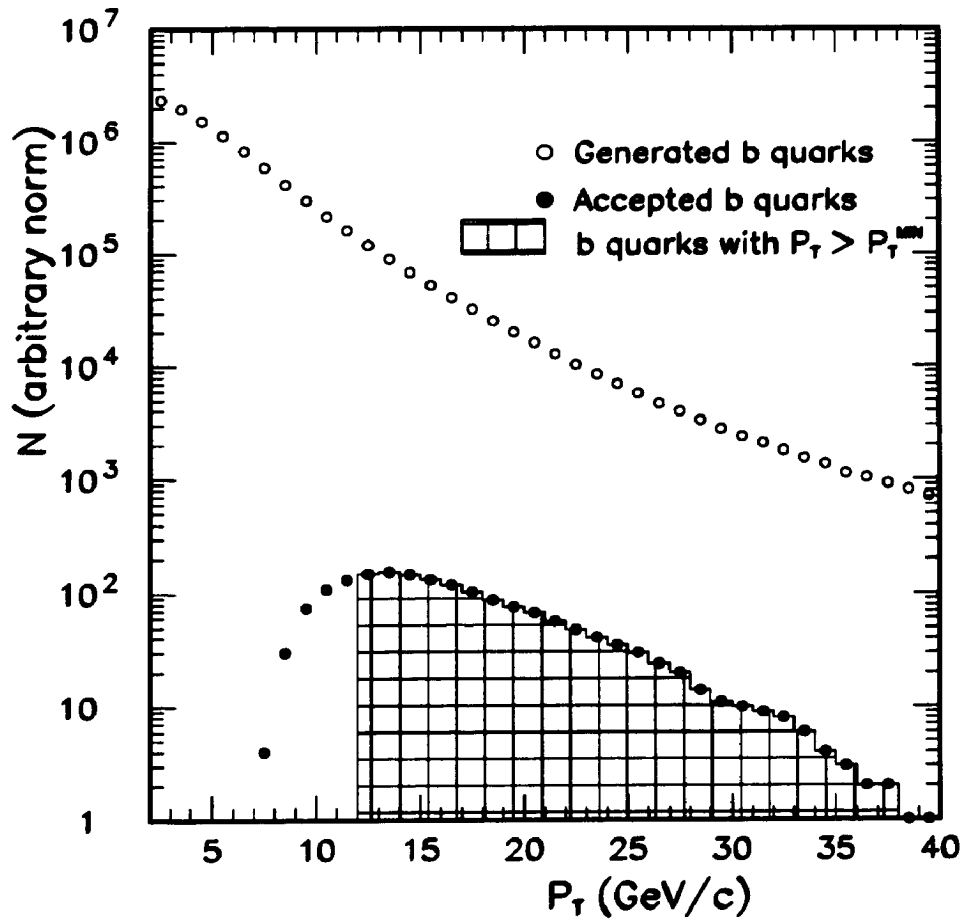


Figure 8.16: Illustration of  $P_T^{\min}$ .

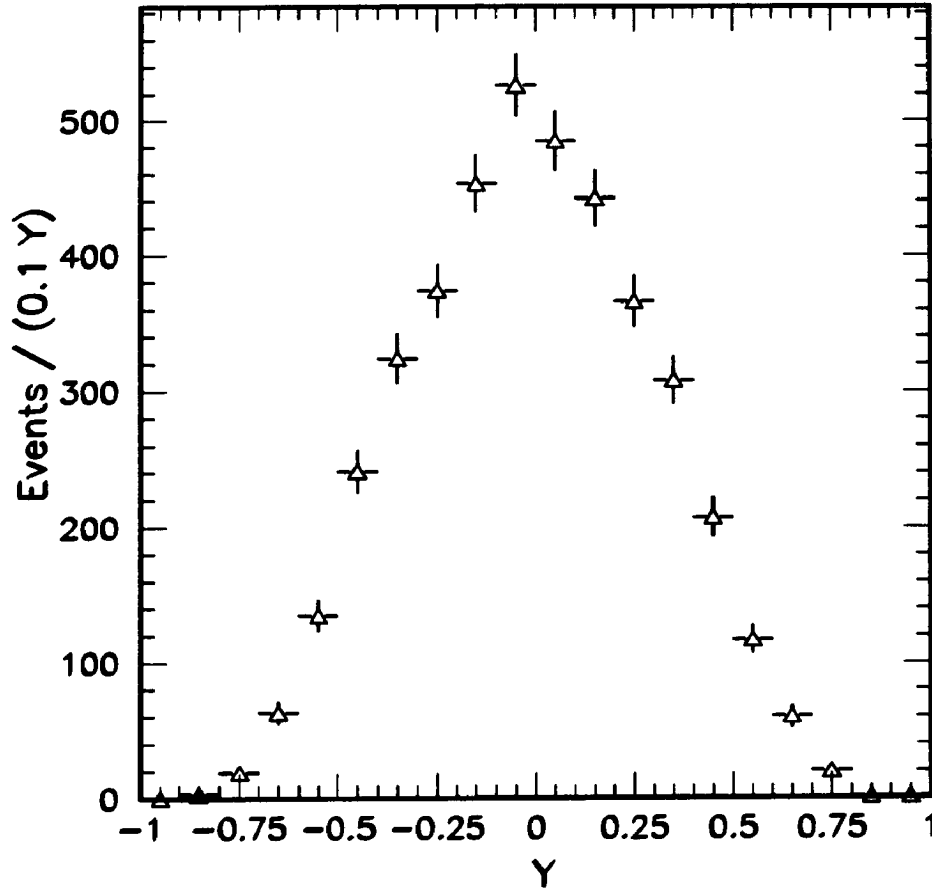


Figure 8.17: The rapidity distribution of  $b$  quarks which contribute to our final sample of observed  $B_u^- \rightarrow J/\psi + K^-$  events. The error bars are statistical.

The determination of the  $b$  quark cross section is done via the following equation:

$$\begin{aligned} & \sigma(\bar{p}p \rightarrow bX; P_{Tb} \geq 11.5 \text{ GeV}/c, |y_b| \leq 1.0) \\ &= \frac{(N/2)}{\epsilon_b \cdot \mathcal{L} \cdot F_{b \rightarrow B^-} \cdot Br(B^- \rightarrow J/\psi + K^-) \cdot Br(J/\psi \rightarrow \mu^+ \mu^-)} \end{aligned}$$

where  $N$  is the number of events we observe in the data,  $\mathcal{L}$  is the integrated luminosity, and  $\epsilon_b$  is the reconstruction efficiency defined above. The combined branching ratio  $Br(B^- \rightarrow J/\psi + K^-) \cdot Br(J/\psi \rightarrow \mu^+ \mu^-)$  is  $(5.2 \pm 1.4) \times 10^{-5}$  [5, 4]. Since our observed sample actually includes contributions from both  $B^+$  and  $B^-$  mesons, we divide  $N$  by 2. In Table 8.3, we summarize the parameters used in the calculation.

Our result for the cross section is:

$$\sigma(\bar{p}p \rightarrow bX; P_{Tb} \geq 11.5 \text{ GeV}, |y_b| \leq 1.0) = 6.1 \pm 1.9 \pm 2.4 \text{ } \mu\text{b}$$

where first error is statistical and the second combines in quadrature the systematic effects listed in Table 8.4.

### 8.3 The $B$ Meson Cross Section

The  $B$  meson cross section calculation follows along very similar path. In this case we use the following relation to determine the cross section:

$$\begin{aligned} & \sigma(\bar{p}p \rightarrow B^- X; P_{TB} \geq 9.0 \text{ GeV}/c, |y_B| \leq 1.0) \\ &= \frac{(N/2)}{\epsilon_B \cdot \mathcal{L} \cdot Br(B^- \rightarrow J/\psi + K^-) \cdot Br(J/\psi \rightarrow \mu^+ \mu^-)} \end{aligned}$$

Table 8.3: Parameters used in the  $b$  quark production cross section calculation.

Parameter	Value
Number of events, $N$	$14.1 \pm 4.3$
Efficiency, $\epsilon_b$	$(2.27 \pm 0.45)\%$
Luminosity, $\mathcal{L}$	$(2.6 \pm 0.2)\text{pb}^{-1}$
$Br(B^- \rightarrow J/\psi + K^-) \cdot Br(J/\psi \rightarrow \mu^+ \mu^-)$	$(5.2 \pm 1.4) \times 10^{-5}$
$F_{b \rightarrow B^-}$	0.375

Table 8.4: Systematic uncertainties in the cross section calculation.

Source	Uncertainty
Mass fitting	20%
Offline reconstruction	7%
Trigger efficiency	12%
$b$ -quark fragmentation	10%
$b$ -quark $P_T$ shape	10%
Combined branching ratios	27%
Luminosity	7%
Total	40%

where  $\epsilon_B$  is the reconstruction efficiency for the process  $B_u^- \rightarrow J/\psi + K^-$ ,  $J/\psi \rightarrow \mu^+\mu^-$ . To determine this efficiency we use the Monte Carlo procedure above. We assume the generation of  $B_u^-$  mesons is via underlying  $b$ -quark production, with the energy sharing model of Peterson *et al* [18]. With these assumptions, the systematic uncertainties in the measurement are the same as above. Clearly, there is no assumption about how often a  $b$  quark fragments into  $B_u^-$ . The Monte Carlo model predicts  $\epsilon_B = (1.87 \pm 0.37)\%$ , where the error represents the sum in quadrature of the systematic effects due to offline reconstruction and the trigger parameterization.

The result for the cross section is:

$$\sigma(\bar{p}p \rightarrow B^- X; P_{TB} \geq 9.0 \text{ GeV}/c, |y_B| \leq 1.0) = 2.8 \pm 0.9(stat) \pm 1.1(syst) \mu\text{b}$$

where the errors are broken down as for the quark calculation.

## Chapter 9

### Conclusions

#### 9.1 Comparison of the measurement with theoretical prediction

Using a data set corresponding to an integrated luminosity of  $2.6 \text{ pb}^{-1}$ , we have successfully reconstructed the exclusive decay  $B_u^- \rightarrow J/\psi + K^-$ . This represents the first full reconstruction of  $B$  mesons in a hadron collider. We have used this sample of  $B$  mesons to perform the first measurement of the  $B^-$ -meson and  $b$ -quark production cross sections at  $\sqrt{s} = 1.8 \text{ TeV}/c^2$  in  $p\bar{p}$  collisions.

As mentioned previously, the  $b$ -quark production cross section has been calculated complete through order  $\alpha_s^3$  [6]. Our result for the  $b$ -quark cross section integrated above  $P_{Tb} = 11.5 \text{ GeV}/c$  is shown in Figure 9.1, along with curves representing the theoretical calculation. In this plot we also show CDF measurements using an independent analysis [52]. In Table 9.1, we list the results from all the CDF measurements. In the last column of this table we note the ratio of the CDF measurement to the central theoretical prediction (i.e. no errors in the theoretical calculation have



Table 9.1: Measurements of the  $b$  quark cross section at CDF, compared to the theoretical calculation.

Sample	$P_T^{min}$ GeV/c	Cross Section ( $\mu\text{b}$ )	Factor $\times$ NDE
$B_u^- \rightarrow J/\psi + K^-$	11.5	$6.1 \pm 3.1$	$5.3 \pm 2.7$
$B \rightarrow e^- \bar{\nu} D^0 X$	19.0	$0.45 \pm .16$	$2.1 \pm 0.8$
$B \rightarrow e^- \bar{\nu} X$	15.0	$1.15 \pm 0.45$	$2.2 \pm 0.9$
$B \rightarrow e^- \bar{\nu} X$	23.0	$0.21 \pm 0.08$	$2.1 \pm 0.8$
$B \rightarrow e^- \bar{\nu} X$	32.0	$0.05 \pm 0.02$	$2.3 \pm 0.9$

been included). It is clear that the general trend of all the CDF measurements is towards a cross section that is of order 2 times larger than that predicted by theory. However, it must also be noted that the measurements all possess large uncertainties.

## 9.2 Future Prospects

As far as measuring the  $b$  quark production cross section, clearly the first priority is to verify that the physical cross section is indeed 2 to 3 times larger than that predicted by theory. The only way this can be done is by reducing the measurement error, both statistical (which stands at 28%) and systematic (which stands at 40%). We list here the likely improvements which will be made in the next collider run, which at the time of this writing is scheduled for May, 1992.

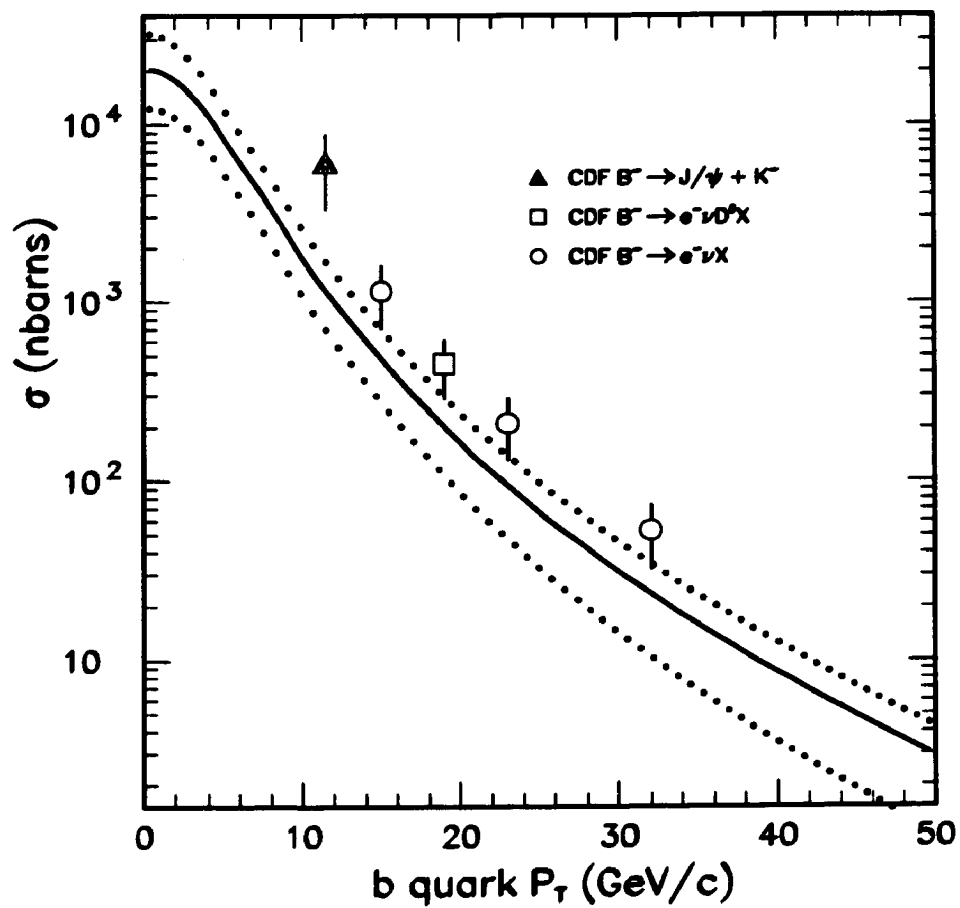


Figure 9.1: The  $b$  quark production cross section using all current CDF measurements. Also shown is the theoretical calculation of Nason *et al.*

- The aim of the next CDF run is to collect approximately  $25\text{pb}^{-1}$  of data, which is almost a factor of 10 increase over the data sample used in this analysis. Detector upgrades could optimistically increase the acceptance by another factor of 10, leading to an overall reduction in the statistical error from 28% to less than 5%.
- The systematic error associated with the mass fitting procedure is highly correlated to the data sample size. In fact, a case could be made that we have actually double counted our statistical error by assigning this error. In any event, with a data sample size that is expected to be  $\geq 1000$  identified  $B_u^- \rightarrow J/\psi + K^-$  candidates, this error should go from its present 20% to  $\leq 2\%$ .
- The systematic associated with the trigger efficiency will likely be reduced from 12% to  $\leq 5\%$ . This will be accomplished through cosmic ray muon studies dedicated to an analysis of the low  $P_T$  behavior of the muon trigger.
- Finally, the largest single systematic in this analysis is the branching ratio measurement of  $B_u^- \rightarrow J/\psi + K^-$ . We depended on measurements made at ARGUS and CLEO, which had uncertainties of the order of 30%. This was because the identified  $B_u^- \rightarrow J/\psi + K^-$  data samples at these two experiments were both of order 8 events. The upgraded detector CLEO II has been steadily collecting data through 1991, and by the end of 1992 should have a data sample

approximately 10 times larger than that used to extract the current  $B_u^- \rightarrow J/\psi + K^-$  branching ratio. From this we estimate that the total error in their branching ratio estimate should be  $\leq 10\%$ .

To recap, we can expect the statistical error in the next measurement of the cross section to drop from 28% to 5%. We can expect the total systematic error to drop from 40% to about 20%. The errors added in quadrature should go from 50% to about 21%. At this stage, a discrepancy between experiment and theory of a factor of 2 or larger would be very significant.

## Bibliography

- [1] F. Abe *et al.*, *A Measurement of the B-Meson and b-Quark Cross Sections at  $\sqrt{s} = 1.8$  TeV Using the Exclusive Decay  $B^\pm \rightarrow J/\psi K^\pm$* ,  
Submitted to Phys. Rev. Letters.
- [2] Particle Data Group, J. J. Hernández *et al.*, Phys. Lett. B **239** (1990).
- [3] L3 Collaboration, B. Adeva, *et al.*, Phys. Lett. B **252**, 703 (1990);  
ALEPH Collaboration, D. Decamp, *et al.*, Phys. Lett. B **258**, 236 (1991);  
UA1 Collaboration, C. Albajar *et al.*, Phys. Lett. B **262** 171 (1991);  
F. Abe, *et al.*, Phys. Rev. Lett. **67** 3351 (1991).
- [4] CLEO Collaboration, D. Bortoletto *et al.*, Phys. Rev. D **45** 21 (1992).
- [5] ARGUS Collaboration, H. Albrecht *et al.*, Z. Phys. C **48** 543 (1990).
- [6] P. Nason, S. Dawson, and R. K. Ellis, Nucl. Phys. B **303** 607 (1988); Nucl. Phys. B **327** 49 (1989); Nucl. Phys. B **335** 260 (1990).

- [7] G. Altarelli, M. Diemoz, G. Martinelli, and P. Nason, Nucl. Phys. B **308** 724 (1988).
- [8] W. Beenakker, H. Kuifj, W. L. van Neeven, and J. Smith, Phys. Rev. D **40** 54 (1989).
- [9] Good reviews can be found in:
- C. Quigg, *Gauge Theories of the Strong, Weak, and Electromagnetic Interactions*, (Benjamin/Cummings, Reading, Mass. 1983);
- V. Barger and R. Phillips, *Collider Physics*, (Addison-Wesley, Redwood City, Calif., 1987);
- G. Kane, *Modern Elementary Particle Physics*, (Addison-Wesley, Redwood City, Calif., 1987).
- [10] R. P. Feynman, *Quantum Electrodynamics*, (Benjamin/Cummings, Reading, Mass. 1961).
- [11] S. Glashow, Nucl. Phys. **22**, 579 (1961); S. Weinberg, Phys. Rev. Lett., **19**, 1264 (1967); A. Salam, Proc. 8<sup>th</sup> Nobel Symp., W. Svartholm, *ed.*, (Almqvist and Wiksell, Stockholm 1968).
- [12] R. N. Cahn and G. Goldhaber, *The Experimental Foundations of Particle Physics*, (Cambridge University Press, Cambridge, Mass., 1989).

- [13] A good review can be found in F. J. Yndurain, *Quantum Chromodynamics: An Introduction to the Theory of Quarks and Gluons*, (Springer, New York, 1983).
- [14] J. C. Collins, D. E. Soper, and G. Sterman, Nucl. Phys. B **261** 104 (1985).
- [15] This form of the Lagrangian appears in the Barger and Phillips text cited in reference [9].
- [16] G. Altarelli and G. Parisi, Nucl. Phys. B **126** 298 (1977).
- [17] J. C. Collins, Nucl. Phys. B (Proc. Suppl.) **12** 219 (1990).
- [18] C. Peterson *et al.*, Phys. Rev. D **27** 105 (1983).
- [19] J. Chrin, Z. Phys. C **36** 163 (1987).
- [20] A good summary of fragmentation models can be found in:  
*Electron-Positron Annihilation Physics*, B. Foster, *ed.*, (Adam Hilger, Bristol 1990).
- [21] TASSO Collab, M. Althoff, *et al.*, Z. Phys. C **27** 27 (1985);  
HRS Collab., M. Derrick, *et al.* Phys. Lett. B **158**, 519 (1985).
- [22] CDF Collab, F. Abe, *et al.*, Phys. Rev. D **40** 3791 (1989).
- [23] M. Bauer, B. Stech, M. Wirbel, Z. Phys. C **34** 103 (1987).

- [24] N. Cabibbo, Phys. Rev. Lett. **10**, 531 (1963);  
M. Kobayashi, T. Maskawa, Prog. Theor. Phys. **49**, 652 (1973).
- [25] P. Avery, *Review of B Decays*, UFTP Preprint -EXP-87-1.
- [26] E. W. N. Glover, A. D. Martin, W. J. Stirling, Z. Phys. C **38** 473 (1988);  
R. Baier and R. Ruckl, Nucl. Phys. B **208** 281 (1981).
- [27] S. D. Holmes, *A Practical Guide to Modern High Energy Accelerators*, Sante Fe TASI-87.
- [28] S. D. Holmes, *Achieving High Luminosity in the Fermilab Tevatron*, Fermilab-CONF-91-141.
- [29] M. J. Schochet, *The Physics of Proton Antiproton Collisions*, Fermilab-CONF-91-341-E.
- [30] F. Abe *et al.*, Nucl. Instrum. Methods Phys. Res., Sect. A **271**, 387 (1988).
- [31] F. Snider *et al.*, Nucl. Instrum. Methods Phys. Res., Sect. A **268**, 75 (1988).
- [32] F. Bedeschi *et al.*, Nucl. Instrum. Methods Phys. Res., Sect. A **268**, 50 (1988).
- [33] C. Newman-Holmes, E. Schmidt, R. Yamada, *Measurement of the Magnetic Field of the CDF Magnet*, CDF Internal Note 346;  
D. A. Crane, H. B. Jensen, C. Newman-Holmes, *Solenoid Magnetic Field in the 1988-89 Run*, CDF Internal Note 969.



- [34] L. Balka, *et al.*, Nucl. Instrum. Methods Phys. Res., Sect. A **267**, 272 (1988).
- [35] S. Bertolucci, *et al.*, Nucl. Instrum. Methods Phys. Res., Sect. A **267**, 301 (1988).
- [36] G. Ascoli, *et al.*, Nucl. Instrum. Methods Phys. Res., Sect. A **268**, 33 (1988).
- [37] D. Amidei *et al.*, Nucl. Instrum. Methods Phys. Res., Sect. A **269**, 51 (1988).
- [38] J. T. Carroll *et al.*, Nucl. Instrum. Methods Phys. Res., Sect. A **300**, 552 (1991).
- [39] G. Ascoli *et al.*, Nucl. Instrum. Methods Phys. Res., Sect. A **269**, 63 (1988).
- [40] A. Gauthier, *Efficiency of the Level 1 Central Muon Trigger*, CDF Internal Note 1002.
- [41] R. C. Fernow, *Introduction to Experimental Particle Physics*, (Cambridge University Press, Cambridge, Mass. 1986).
- [42] B. Schorr, *Programs for the Landau and the Vavilov Distributions and the Corresponding Random Numbers*, Comp. Phys. Comm. **7**, 215 (1974).
- [43] G. W. Foster *et al.*, Nucl. Instrum. Methods Phys. Res., Sect. A **269**, 93 (1988).
- [44] M. Binkley and J. C. Yun, *A Study of Multiple Interactions From VTPC Analysis*, CDF Internal Note 884;  
M. Binkley and J. Hinkelman, *Road Searching Routines for the VTPC*, CDF Internal Note 841.

- [45] T. Rodrigo, Private communication.
- [46] M. Spahn, R. W. Kadel, A. Barbaro-Galtieri, P. Berge, *A Study Of Tracking Systematics in the CTC*, CDF Internal Note 1539.
- [47] A. Mukherjee, *CTC Calibration and Alignment*, CDF Internal Note 1002.
- [48] T. Westhusing, *The Central Muon Analysis Code*, CDF Internal Note 737.
- [49] D. Frei, *Multiple Scattering of Central Muons*, CDF Internal Note 1430.
- [50] J. Marriner, Private communication.
- [51] UA1 Collab., C. Albajar *et al.*, Phys. Lett. B **256** 121 (1991).
- [52] F. Abe *et al.*, *A Measurement of the Bottom Quark Production in 1.8 TeV Proton-Antiproton Collisions Using Semileptonic Decay Electrons*,  
To be submitted to Phys. Rev. Letters.



## 2017 ProQuest Distribution Agreement

This Agreement is between the author (Author) and ProQuest LLC, through its ProQuest Dissertation Distribution business (formerly ProQuest/UMI). Under this Agreement, Author grants ProQuest certain rights to preserve, archive and distribute the dissertation or thesis (the Work), abstract, and index terms provided by Author to ProQuest.

### Section I. License for Inclusion of the Work in ProQuest Publishing Program

**Grant of Rights.** Author hereby grants to ProQuest the non-exclusive, worldwide right to reproduce, distribute, display and transmit the Work (in whole or in part) in such tangible and electronic formats as may be in existence now or developed in the future. Author further grants to ProQuest the right to include the abstract, bibliography and other metadata in the ProQuest Dissertations & Theses database (PQDT) and in ProQuest Dissertation Abstracts International and any successor or related index and/or finding products or services.

**ProQuest Publishing Program - Election and Elements.** The rights granted above shall be exercised according to the publishing option selected by Author in Section III, Author Options, and subject to the following additional Publishing Program requirements:

- **Distribution of the Work.** Except as restricted by Author in the publishing option selected, the rights granted by Author automatically include (1) the right to allow sale and distribution of the Work, in whole or in part, by ProQuest and its sales agents and distributors and (2) the right to make the Abstract, bibliographic data and any meta data associated with the Work available to search engines and harvesters.
- **Restrictions.** ProQuest will use commercially reasonable efforts to restrict the distribution of the Work as provided under the publishing option selected by Author or as later elected by Author through direct contact with ProQuest. Such election is subject to Author's Degree Granting Institution Directives. With respect to restrictions requested after submission of the Work, Author acknowledges that ProQuest cannot recall or amend previously distributed versions of the Work.
- **Removal of Work from the Program.** ProQuest may elect not to distribute the Work if it believes that all necessary rights of third parties have not been secured. Refer to the website [http://www.proquest.com/products\\_umi/dissertations/](http://www.proquest.com/products_umi/dissertations/) for information about copyright and your dissertation or thesis. If Author's degree is rescinded, and/or the degree-granting institution so directs, ProQuest will expunge the Work from its publishing program in accordance with its then current publishing policies.
- **Degree Granting Institution Directives.** Author is solely responsible for any conflict between policies and directions of Author's degree-granting institution, Author's choice of publishing model, and/or any restriction Author places on the use of the Work. For the avoidance of doubt, ProQuest is not responsible for access to the Work that is provided by Author's degree-granting institution through its library or institutional repository. Author must work directly with Author's degree granting institution to ensure application of any restrictions to access relating to the Work by Author's degree granting institution.

**Delivery of the Work.** Author shall provide to ProQuest the Work and all necessary supporting documents during the online submission process, according to the Instructions accompanying this agreement.

**Rights Verification.** Author represents and warrants that Author is the copyright holder of the Work and has obtained all necessary rights to permit ProQuest to reproduce and distribute third party materials contained in any part of the Work, including all necessary licenses for any non-public, third party software necessary to access, display, and run or print the Work. Author is solely responsible and will indemnify ProQuest for any third party claims related to the Work as submitted for publication.

#### Open Access Publishing Plus

- ☒ I want the broadest possible dissemination of my work, and I want to provide free global access to the electronic copy of my work via the internet.
- ☒ I understand that I will not be eligible to receive royalties.

I want major search engines (e.g. Google, Yahoo) to discover my work. Learn more: <http://www.proquest.com/en-US/products/dissertations/google.shtml>

- ☒ Yes
- ☒ No

Acknowledgment: I have read, understand and agree to this ProQuest Publishing Agreement, including all rights and restrictions included within the publishing option chosen by me as indicated above.

REQUIRED Author's signature \_\_\_\_\_ Date 8/18/17  
(Print Name) Richard E. Hughes  
Institution conferring degree Univ of Penn

Formatted: Indent: Left: 0.69", First line: 0.07", Bulleted + Level: 1 + Aligned at: 0.69" + Indent at: 0.78"

Formatted: Indent: Left: 0.75", Bulleted + Level: 2 + Aligned at: 0.81" + Indent at: 1.06"